NOAA Technical Memorandum ERL ETL-292

SENSITIVITY OF MILLIMETER AND SUB-MILLIMETER WAVE CHANNELS TO CLEAR AIR TEMPERATURE AND WATER VAPOR VARIATIONS

M. Klein
A.J. Gasiewski

Environmental Technology Laboratory
Boulder, Colorado
August 1998

noaa NATIONAL OCEANIC AND ATMOSPHERIC ADMINISTRATION / Environmental Research Laboratories

NOAA Technical Memorandum ERL ETL-292

SENSITIVITY OF MILLIMETER AND SUB-MILLIMETER WAVE CHANNELS TO CLEAR AIR TEMPERATURE AND WATER VAPOR VARIATIONS

Marian Klein
Albin J. Gasiewski

Environmental Technology Laboratory
Boulder, Colorado
August 1998

NOTICE

Mention of a commercial company or product does not constitute an endorsement by the NOAA Environmental Research Laboratories. Use of information from this publication concerning proprietary products or the test of such products for publicity or advertising purposes is not authorized.

For sale by the National Technical Information Service, 5285 Port Royal Road
Springfield, VA 22061

Table of Contents.

Abstract. The brightness temperature observed from above the Earth's atmosphere is sensitive to parameters such as pressure, temperature, water vapor, and hydrometeor content. This sensitivity around oxygen and water vapor absorption lines has been used successfully for passive vertical sounding of temperature and water vapor profiles. In order to determine optimal sounding strategies for future high-resolution, passive, microwave instruments, a study of the potential clear-air sounding capabilities of all significant microwave oxygen and water vapor absorption lines in the frequency range from approximately 10 to 1000 GHz has been undertaken. The study uses a second-order statistical climatological model covering four seasons and three latitudinal zones: low (30°S to 30°N), middle (30° to 60°), and high (60° to 90°) latitudes, and a wide range of altitudes (up to ~70 km). The climatological model was developed using data from three sources: the Upper Atmosphere Research Satellite (UARS) HALogen Occultation Experiment (HALOE) instrument, the TIROS Operational Vertical Sounder (TOVS) Initial Guess Retrieval (TIGR) radiosonde set, and the NOAA Advanced Microwave Sounder Unit (AMSU) radiosonde set. Variations in the vertical sensitivities of brightness temperature due to statistical variations of water vapor and temperature with latitude and season around each line are considered, and useful channel sets for geostationary microwave vertical sounding are suggested.

1. Introduction

The synoptic measurement of atmospheric temperature and humidity profiles, clouds, and land and ocean surface parameters using satellite is nearly three decades old. The microwave frequencies currently used for these purposes are primarily below 200 GHz near oxygen and water vapor resonances and in the window regions between such resonances. Recent technological progress in the development of millimeter-wave and submillimeter-wave receivers, however, now allows the possibility of using increasingly higher frequencies for atmospheric observation. For example, the Microwave Limb Sounder on the NASA Upper Atmospheric Research Satellite (UARS) incorporates limb-sounding radiometers operating at 205 GHz for the measurement of trace species such as ClO, ozone, sulfur dioxide, nitric acid, etc. Future versions of this instrument will incorporate even higher frequency radiometers - 240 and 640 GHz.

The advent of higher frequency radiometers stands not only to benefit limb sounding of the upper atmosphere, but also vertical sounding of the troposphere, and lower stratosphere. The potential advantages of using submillimeter-wave (SMMW) channels (>300 GHz) for vertical sounding of water vapor and clouds were first discussed by *Gasiewski*, [1992]. In particular, it was pointed out that water vapor sounding could potentially be performed using the 325.1529 GHz water vapor (H2Ov) resonance nearly equally well as using the 183.3101 GHz resonance, but with significant improvements in spatial resolution for diffraction-limited imaging systems. The advantage of increased spatial resolution is important for temporally-resolved imaging of rapidly evolving severe weather from geosynchronous orbit wherein the maximum size of the aperture of the imaging system is cost constrained to no more than perhaps a few meters.

It was also shown by both *Gasiewski*, [1992] and *Evans and Stephens*, [1991] that microwave sounding channels above 300 GHz could potentially be used to measure cirrus ice cloud mass. The detection and measurement of cirrus clouds by conventional microwave channels[1] is difficult due to the

[1] Herein defined to be those frequencies below 300 GHz.

high degree of transparency of clouds at these frequencies. The relatively low spatial resolution that can be obtained using conventional channels further compounds this problem. In contrast, at infrared frequencies, even relatively thin cirrus clouds are virtually opaque, thus, their bulk properties cannot easily be measured. However, observation within the range of frequencies from ~300 to ~1000 GHz provide a useful trade-off in sensitivity between high cloud transparency at conventional microwave frequencies and high cloud opacity at infrared frequencies. A factor of ~3-10 increase in sensitivity to cloud parameters relative to the conventional microwave frequencies can be expected in this range, thus facilitating the measurement of cirrus integrated ice content without serious degradation of temperature and water vapor sounding capabilities. Moreover, the use of similar weighting function sets for water vapor or oxygen at frequency intervals spaced approximately one or two octaves apart can provide additional degrees of observational freedom which can be used to discriminate between the effects of cirrus clouds and water vapor or temperature variations. Examples of such sets include weighting functions at frequencies spaced appropriately around the 183.3101 and 325.1529 GHz water vapor lines, the 183.3101 and 380.1974 GHz water vapor lines, and the 118.7503 and 424.7631 GHz oxygen lines.

The high spatial resolution capabilities of submillimeter-wave vertical sounding channels are also expected to be useful for mapping precipitation systems, for example, hurricane eye regions and convection near front lines. Unlike infrared channels, these channels do not typically saturate in the presence of hydrometeors in precipitating cloud tops, but rather provide a monotonic response related to the amount of ice loft in the cell top, and hence, to the severity of the convection [*Gasiewski et al.*, 1994]. Again, the primary application would be from geosynchronous orbit, although the high-resolution capabilities of SMMW channels could be fully utilized from low-earth orbiting altitudes or from medium to high-altitude aircraft. The application of SMMW channels from any of these perspectives could be used to drive numerical weather prediction models through direct assimilation of submillimeter-wave radiance data.

In order to develop optimal vertical sounding and imaging strategies using submillimeter wave channels we consider in this study several issues related to the sensitivity of the upwelling brightness spectrum to atmospheric water vapor and temperature in clear air.[2] We emphasize observations over an ocean background due the relative utility of synoptic satellite measurements over the ocean compared to their use over land. The sounding capabilities of SMMW channels at frequencies above ~200 GHz are to a great extend determined by the water vapor continuum absorption spectrum. The continuum spectrum in turn, is the result of far-wing effects of opacity resulting from the strong rotational water lines located in the far-infrared portion of the spectrum, and provides a upper altitude limit to the probing height of all submillimeter-wave sounding channels. The limiting effect of the continuum is particularly significant for moist atmospheric conditions (e.g., tropical or midlatitude conditions during summer).

Several strongly absorbing water vapor lines exist below 1000 GHz, which are sensitive to temperature and water vapor vertical structure in the upper troposphere to lower mesosphere. While the existence of these lines suggest the possibility of sounding water vapor within the 10-80 km range, limitations resulting from the small natural degree of variation of water vapor at high altitudes also exist. The degree to which high-altitude water vapor sounding is limited by the natural degree of variation is considered within this study. The degree of variation is determined using three climatological databases of water vapor profiles from the surface to the mesosphere. The three bases are derived from both rocketsonde and solar occultation measurements, and agree typically within one order of magnitude on

[2] We are considering the sensitivity of SMMW channels to clouds in a follow-on study.

the concentration of water vapor within their regions of overlap. Conclusions are made with regard to the applicability of the databases, and full second-order climatology for temperature and water vapor from the surface to the lower mesosphere and parametrized by season and latitude is presented.

The response of the brightness spectrum to water vapor content is highly nonlinear and best analyzed using incremental response function (or, incremental weighting functions, IWF). These are indeed the functions that are required in any incremental retrieval or data assimilation operation. Since the mean amount of water vapor can significantly change this response in height, magnitude, and even sign, the response of the spectrum to water vapor is considered for both extreme moist (summer tropical) and extreme dry (winter polar) conditions. With the above considerations we provide a proposed selection of channels to be used for temperature and water vapor sounding at submillimeter wavelengths. A uniform distribution of the peaking altitude sensitivity is used as a criterion for channel set selection. The limitation of the absorption model used to compute the incremental weighting functions is also studied by comparing brightness calculations from two models to ground-based SMMW radiometer observations.

An additional motivation for this study is to provide information necessary to define the optimal set of passive submillimeter-wave channels for international frequency allocation purposes. Allocation of frequency bands for various passive and active applications by the International Telecommunications Union (ITU) is currently ongoing, with tradeoffs between active and passive applications of the spectrum above 300 GHz being of immediate interest.[3] Information on the clear-air sounding capability of the spectrum up to 1000 GHz is one basis for making allocation decisions. Other issues to be considered in this process, of course, include observing geometry, receiver technology, antenna characteristics, sharing capabilities, and sensitivity criteria. However, it is prudent to first identify the optimal set of bands for vertical sounding from the basis of their geophysical responses, then to modify the selection of these bands based on technological sharing concerns.

2. Incremental Weighting Functions

The incremental weighting functions describe the relationship between infinitesimal variations in any atmospheric parameter and the upwelling brightness temperature. If $\delta p(z)$ is the profile variation of the atmospheric parameter of concern, then the variation in the upwelling brightness temperature $\delta T_B(f,\theta)$ is:

$$\delta T_B(f,\theta) = \int_0^\infty \delta p(z) W_p(z,f,\theta) dz \tag{1}$$

where W_p is the incremental weighting function for parameter p, and θ is the observation angle measured with respect to nadir. The parameters of concern for this study are temperature and water vapor density, although cloud density, cloud particle size, rain rate etc. are other interesting parameters. Incremental weighting function have been described in the literature e.g. [*Jackson and Gasiewski*, 1995], [*Westwater et al.*, 1990], but are often confused with full weighting functions. For clarification purposes, the full weighting function is defined as follows [*Gasiewski*, 1993]:

---

[3] Of the new issues to be considered at the 1999 World Radio Conference (WRC) is the allocation of frequencies above 300 GHz.

$$T_B(z,\theta)=\int_0^{\infty}T(z)W(f,\theta)dz+T_S W_S+T_{CB}W_{CB} \tag{2}$$

The function $W(f,\theta)$ is recognized as a kernel of the integrated radiative transfer equation, and represents the relative contributions to the overall brightness temperature from various atmospheric levels. The terms T_S, T_{CB} represents the contributions from the surface and cosmic background respectively. In contrast, the incremental weighting function describes the brightness temperature response to small perturbation in an atmospheric parameter. For example, a change of water vapor by $\delta\rho(z)$ will result in change of observed brightness temperature by δT_B:

$$T_B(f,h,\theta)=T_B^0(f,h,\theta)+\delta T_B=T_B^0(f,h,\theta)+\int_0^{\infty}W_\rho(f,z,\theta)\delta\rho(z)dz \tag{3}$$

The incremental weighting function $W_\rho(f,z,\theta)$ provides information about the vertical sensitivity to the observed parameter, what makes it a useful tool for sensitivity studies.

The derivation of the IWF for water vapor and for an upward looking radiometer is shown in Appendix A. Following similar steps the IWF for a downward-looking radiometer and for temperature is also derived. The results of such derivations follow. The water vapor IWF for an upward-looking radiometer at height h is:

$$W_\rho^{\downarrow}(f,z,\theta)=\left.\frac{\partial\alpha(f,T(z),\rho(z))}{\partial\rho}\right|_{\rho^0(z)}\sec\theta e^{-\tau(f,h,z)\sec\theta}\cdot \left\{\begin{array}{l} T_B(f,T(z))-T_B(f,T_{CB})e^{-\tau(f,h,\infty)\sec\theta}- \\ \int_z^{\infty}T_B(f,T(z'))\alpha(f,T(z'),\rho(z'))\sec\theta e^{-\tau(f,z,z')\sec\theta}dz' \end{array}\right\} \tag{4}$$

in units, e.g., of $(K\ km^{-1}\ g^{-1}m^3)$.

The water vapor IWF for a downward-looking radiometer is:

$$W_\rho^{\uparrow}(f,z,\theta)=W_\rho^{\downarrow R}(f,z,\theta)+\left.\frac{\partial\alpha(f,T(z),\rho(z))}{\partial\rho}\right|_{\rho^0(z)}\sec\theta e^{-\tau(f,z,h)\sec\theta}\cdot \left\{\begin{array}{l} T_B(f,T(z))-\int_0^{z}T_B(f,T(z'))\alpha(f,T(z'),\rho(z'))\sec\theta e^{-\tau(f,z',z)\sec\theta}dz \\ -T_B^{0\downarrow RE}e^{-\tau(f,0,z)\sec\theta} \end{array}\right\} \tag{5}$$

where: $\tau(f,z_1,z_2)=\int_{z_1}^{z_2}\alpha(f,T(z'),\rho(z'))dz'$ is the opacity between levels z_1 and z_2,

$T_B=\dfrac{hf}{K\left(e^{\frac{hf}{KT}}-1\right)}$ is the equivalent radiometer temperature (or brightness temperature) in Kelvins, as given by the Planck law, and:

$$W_\rho^{\downarrow R}(f,z,\theta) = e^{-\tau(f,0,h)\cdot\sec\theta}\, r_\beta(\theta) W_\rho^{\downarrow}(f,z,\theta)$$

$$T_B^{0\downarrow RE} = \left(1 - r_\beta(\theta)\right) T_B(f,T_S) + r_\beta(\theta) T_B(f,0,\infty)$$

$$T_B(f,0,\infty) = \int_0^\infty T_B\left(f,T(z)\right) \alpha\left(f,T(z),\rho(z)\right) \sec\theta\, e^{-\tau(f,0,z)\sec\theta} dz + T_B\left(f,T_{CB}\right) e^{-\tau(f,0,\infty)\sec\theta}$$

Other parameters are:

f	frequency (Hz)
α	total absorption coefficient (Np/km)
$T(z)$	physical temperature at atmospheric height z (K)
ρ (z)	water vapor density (g/m^3)
h	Planck constant (6.6252x10^{-34} J s)
h	observation height (m)
K	Boltzman constant (1.38046x10^{-23} J K^{-1})
r_β	is surface reflection coefficient(dimensionless)
T_S	is surface temperature (K)
T_{CB}	is cosmic background temperature (K).

The temperature IWF for an upward-looking radiometer at height h:

$$W_T^{\downarrow}(f,z,\theta) = \sec\theta e^{-\tau(f,h,z)\sec\theta} \left\{ \begin{array}{l} \left.\dfrac{\partial T_B}{\partial T}\right|_{T^o(z)} \alpha(f,T(z),\rho(z)) + \left.\dfrac{\partial \alpha(f,T(z),\rho(z))}{\partial T}\right|_{T^0(z)} \cdot \\ \left[-T_B(f,T(z)) - T_B(f,T_{CB}) e^{-\tau(f,z,\infty)\sec\theta} - \right. \\ \left. \left[-\int_z^\infty T_B(f,T(z')) \alpha(f,T(z'),\rho(z')) \sec\theta e^{-\tau(f,z,z')\sec\theta} dz' - \right. \right. \end{array} \right\} \quad (6)$$

in units of inverse height, e.g. (km^{-1}). The term $\partial T_B/\partial T$ is the first derivative of the Planck law:

$$\frac{\partial T_B}{\partial T} = \left(\frac{hf}{KT}\right)^2 \frac{e^{\frac{hf}{KT}}}{\left(e^{\frac{hf}{KT}} - 1\right)^2}$$

The temperature IWF for a downward-looking radiometer is:

$$W_T^{\uparrow}(f,z,\theta) = \sec\theta e^{-\tau(f,z,h)\sec\theta} \left\{ \begin{array}{l} \left.\dfrac{\partial T_B}{\partial T}\right|_{T^o(z)} \alpha(f,T(z),\rho(z)) + \left.\dfrac{\partial \alpha(f,T(z),\rho(z))}{\partial T}\right|_{T^0(z)} \cdot \\ \left[-\int_0^z T_B(f,T(z')) \alpha(f,T(z'),\rho(z')) \sec\theta e^{-\tau(f,z,z')\sec\theta} dz' - \right. \\ T_B(f,T(z)) - e^{-\tau(f,0,z)\sec\theta} \cdot \\ \left. \left\{ \left(1 - r_\beta(\theta)\right) T_B(f,T_S) + r_\beta(\theta) \left[T_B(f,0,\infty) + W_T^{\downarrow}(f,z,\theta) \right] \right\} \right] \end{array} \right\} \quad (7)$$

in units of inverse distance, e.g. (km^{-1}).

3. Climatological Statistics.

A result of preliminary sensitivity study for the vicinity of the 183.3101 GHz water vapor absorption line based on the 1976 US Standard Atmosphere [*1976 U.S. std. atmosphere*] model is shown in Figure 1. This model of atmosphere was augmented with water vapor profile based on measurements of the HALOE instruments onboard the UARS [*Nedoluha et al.*, 1997] for the altitudes above approximately 12 km and the NOAA AMSU radiosonde set of water vapor measurements below that level. A surface relative humidity of 80% and water vapor distribution up to 80 km is used. It is seen that rather enormous absolute sensitivity to water vapor exists at the highest level of the atmosphere where water vapor is present. This sensitivity is $\sim -4\text{x}10^6 \left(K km^{-1} g^{-1} m^3\right)$ at ~80 km altitude at the center of the 183.3101 GHz water vapor absorption line. Similar results are obtained when water vapor is augmented up to only 40 km altitude [*Chiou* et. al., 1997], with the highest sensitivity again at the highest level of water vapor in augmented atmosphere at the line center. The total mean amount of water vapor, however, is between 2 and 3 ppmv (parts per million by volume) in the upper stratosphere and mesosphere. Thus changes of significance (e.g. $>\sim 10^{-6}$ g m^{-3} over more than 1 km) are not probable, and it can be thus expected that the brightness response to water vapor at these altitudes will be moderate. To properly discuss this response it is necessary to study the natural distribution and variation in water vapor from the surface through the mesosphere.

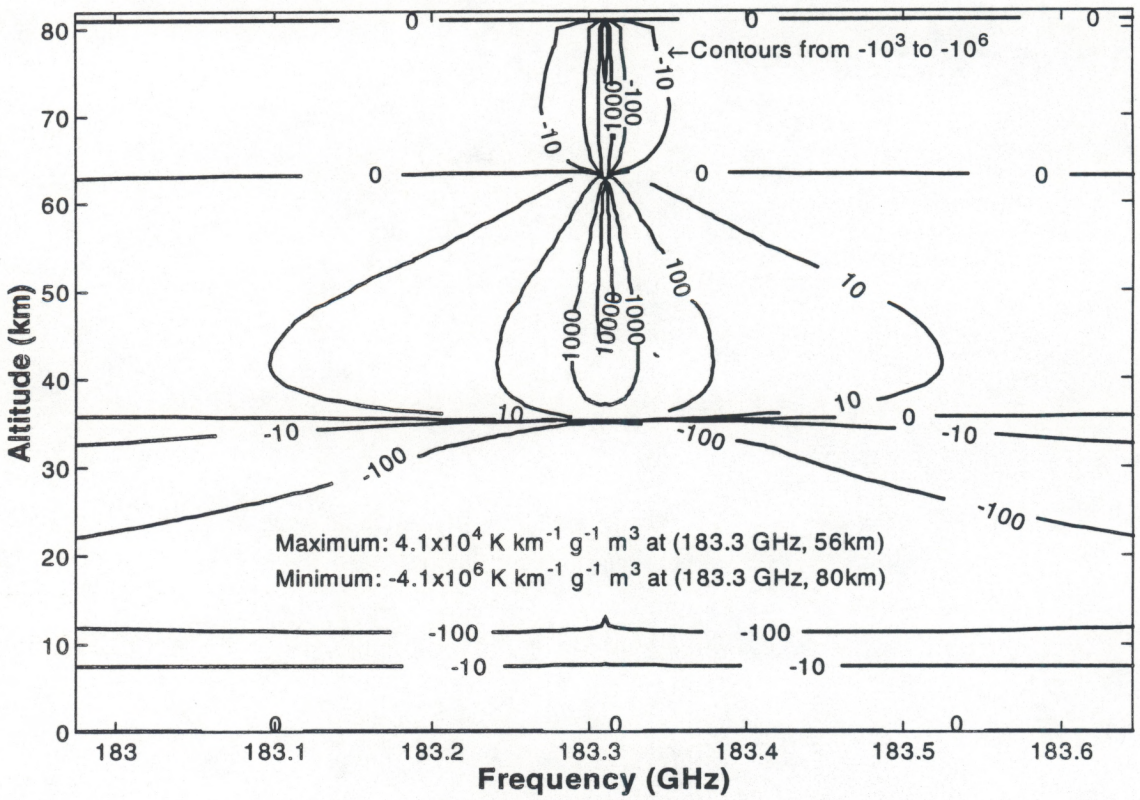

Figure 1. The water vapor IWF contours near 183 GHz in units of $(K\,km^{-1}\ g^{-1}\ m^3)$ for 300 km observation height, ocean background, and nadir view. The calculations use the 1976 U.S. standard atmosphere augmented with water vapor up to 80 km altitude and 80% surface relative humidity.

Three sources of data were used to develop a second-order statistical study of climatology from the surface to ~70 km altitude: (1) the HALOE instrument on board of the UARS [*Russel et al.*, 1993], (2) TOVS Initial Guess Retrieval (TIGR) set [*Chedin et al.*, 1985] based on radiosonde and rocketsonde measurements, and (3) the NOAA AMSU radiosonde set. The data from all three sources were divided into three latitudinal zones: low latitudes (30° south to 30° north), middle latitudes (30° - 60° south or north), and high latitudes (60°-90° south or north), and four seasons: spring (i.e., March, April and May for northern latitudes and September, October and November for southern ones), summer (June, July, August for northern latitudes and December, January, February for southern ones), fall (September, October, November for northern latitudes and March, April, May for southern ones), and winter (December, January, February for northern latitudes and June, July, August for southern ones).

3.1. HALOE Observations.

The HALOE instrument on the UARS was launched on September 12, 1991 and began scientific observations in October 1991. The instrument uses solar occultation of selected portions of the spectral range from 2.45 to 10.04 μm via limb absorption to obtain vertical profiles of O_3, HCl, HF, CH_4, H_2O, NO, NO_2, aerosol extinction, and temperature. A detailed description of the HALOE measurement technique can be found in [*Russel et al.*, 1993].

A limb path contains 30 to 60 times more absorber compared to a nadir sounding path, and thus provides high sensitivity to water vapor at extremely low concentrations. On the other hand, the lower in the atmosphere that a limb path passes, the more altitude levels provide their influence on the final measurement. The retrieval technique is robust enough and the instantaneous field of view is narrow enough, however, to provide vertical resolution better than ~2 km. The HALOE instrument is virtually self calibrating because each gas-mixing ratio vertical profile is determined by computing the ratio of the solar energy attenuated in the atmospheric limb to nonattenuated measurements passing outside the atmosphere.

The disadvantages of this technique are that measurements can be done only at the sunrise and sunset times, thus sampling is limited to 15 sunrises and 15 sunsets each day. Geographic coverage is also constrained in that the satellite covers only latitudes from 80° south to 80° north. In addition, occultation cannot be performed during the polar winters due to the lack of a solar view. Nevertheless, the HALOE profile database contains large number of data profiles, since satellite has been operating for over 6 years.

The second-order HALOE statistics were developed using data from October 1991 to September 1997. For each of the 271 pressure levels for each of the 4 seasons and 3 latitude zones, the total standard deviations of retrieval σ_R^2 were first calculated. The total standard deviation is the sum square of standard deviation of retrieval (including instrument) noise σ_I^2 and the standard deviation of the geophysical parameter σ_P^2, viz.:

$$\sigma_R^2 = \sigma_I^2 + \sigma_P^2 \tag{8}$$

where $p = T$ or ρ. For each parameter in the HALOE database an estimate of the standard deviation of the retrieval noise σ_I^2 is provided. To insure against the propagating instrument noise, only the measurements that complied with condition

$$\sigma_I^2 \leq \frac{\sigma_R^2}{2} \tag{9}$$

were considered as valid samples. In other words, the signal-to-noise ratios (SNR) for samples used in developing the statistics is better than 3 dB. After such evaluation it was concluded, that HALOE temperature measurements satisfy the above condition for altitudes between ~35 to ~75 km and water vapor measurements from ~12 and ~35 km altitude. The number of valid samples found through this procedure for HALOE temperature and water vapor profiles are summarized in Tables 1 and 2, respectively.

The HALOE data were first sorted into appropriate bins according to their latitude and season, then analyzed according to a pressure. For all pressure levels measurement the standard deviation σ_P^2 was evaluated and all the measurements that did not satisfied the condition (9) were rejected. Only profiles that were valid for all selected pressure levels were used in statistical calculation.

Table 1. Number of HALOE temperature profiles used in the second-order climatological study.

Season/Latitude	High (60°-90°)	Middle (30°-60°)	Low (0°-30°)
Spring	5350	4987	3416
Summer	4775	3105	2200
Fall	1544	8585	3615
Winter	0	8733	3380

Table 2. Number of HALOE water vapor profiles used in the second-order climatological study.

Season/Latitude	High (60°-90°)	Middle (30°-60°)	Low (0°-30°)
Spring	3815	3424	2127
Summer	3602	1966	1575
Fall	948	6295	2367
Winter	0	5698	2366

3.2. TIGR Set.

The TOVS Initial Guess Retrieval (TIGR) database was described by *Chedin et al.*, [1985] and since improved [*Cheury et al.*, 1995] and [*Francois and Ottle*, 1996]. The TIGR set groups 1761 representative atmospheric samplings selected from 85000 radiosonde and rocketsonde reports collected around the globe during all seasons for the period from 1976 to 1989. Data are available at 40 pressure levels from the surface to 0.05 mb (~70 km altitude) for temperature, water vapor, and ozone mixing ratio. The primary sources of radiosonde data are files regularly archived by NOAA National Environmental Satellite, Data and Information Service (NESDIS) and the radiosonde archive of the French Meteorological Office.

Although the TIGR database has a smaller number of samples than the HALOE database, it is based on direct measurements (rather than inferred) and covers the entire vertical range from the surface to the mesosphere. The number of samples in each of the defined seasonal/latitudinal bins (Table3) is reasonable large for all bins.

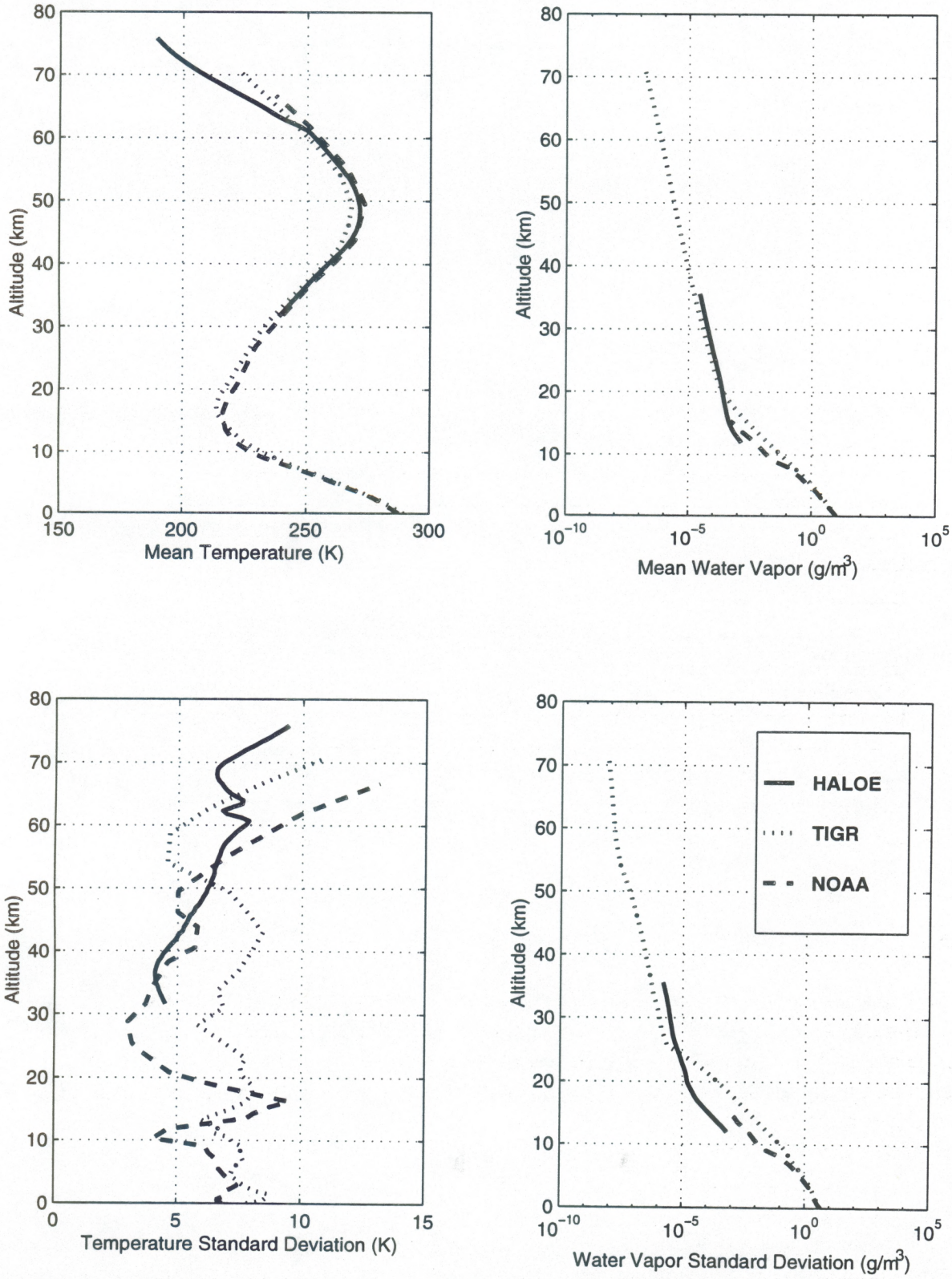

Figure 2. Comparison of the temperature and water vapor density profiles and their standard deviations from the HALOE, TIGR, and NOAA climatologies for the summer and middle latitude case.

Table 3. Number of TIGR temperature and humidity profiles used in the second-order climatological study.

Season/Latitude	High (60°-90°)	Middle (30°-60°)	Low (0°-30°)
Spring	392	110	44
Summer	114	83	44
Fall	102	48	20
Winter	423	292	90

3.3. NOAA AMSU Radiosondes.

The NOAA AMSU database is an ensemble of 715 atmospheric profiles based on radiosonde and rocketsonde reports from several sites around the globe. This data set was first used in the early 1980s for temperature retrieval studies using the proposed NOAA AMSU system.

The AMSU radiosondes provide temperature from the surface to ~0.1 mb pressure (~ 65 km altitude) and provide water vapor profile from surface to ~15 km altitude. The number of samples for each latitudinal/seasonal bin is shown in Table 4.

Table 4. Number of NOAA AMSU profiles used in the second-order climatological study.

Season/Latitude	High (60°-90°)	Middle (30°-60°)	Low (0°-30°)
Spring	50	72	59
Summer	56	90	79
Fall	26	50	50
Winter	43	79	61

3.4. Comparison.

Covariance and correlation matrices were evaluated for all three databases for temperature and water vapor over all valid latitude ranges. Good overall agreement in all latitudinal/seasonal bins was found among the three sets for both mean and standard deviations (e.g. Figure 2). Because of its full global coverage and water vapor profile information over full altitude range, the TIGR database was selected for further studies.

4. Numerical Models.

4.1. Attenuation Model Comparison.

The MRT/Liebe attenuation model [*Liebe*, 1985; 1987] was compared with the Rosenkranz absorption model [*Rosenkranz*, 1993] for the atmospheric species O_2, H_2O_V (water vapor), and N_2. The Rosenkranz absorption model uses fewer absorption lines than MRT/Liebe (about one-half less, see Table 5, and 6) and is valid for frequencies up to ~800 GHz.

The difference spectrum for calculated brightness temperature using the two models for the two extreme atmospheric profiles is shown in Figure 3. The difference in the so-called "continuum" is most significant in between absorption lines below ~400 GHz and counts for ~±5%. Different broadening parameters are responsible for differences in relative absorption up to 25% for regions around the water vapor line centers.

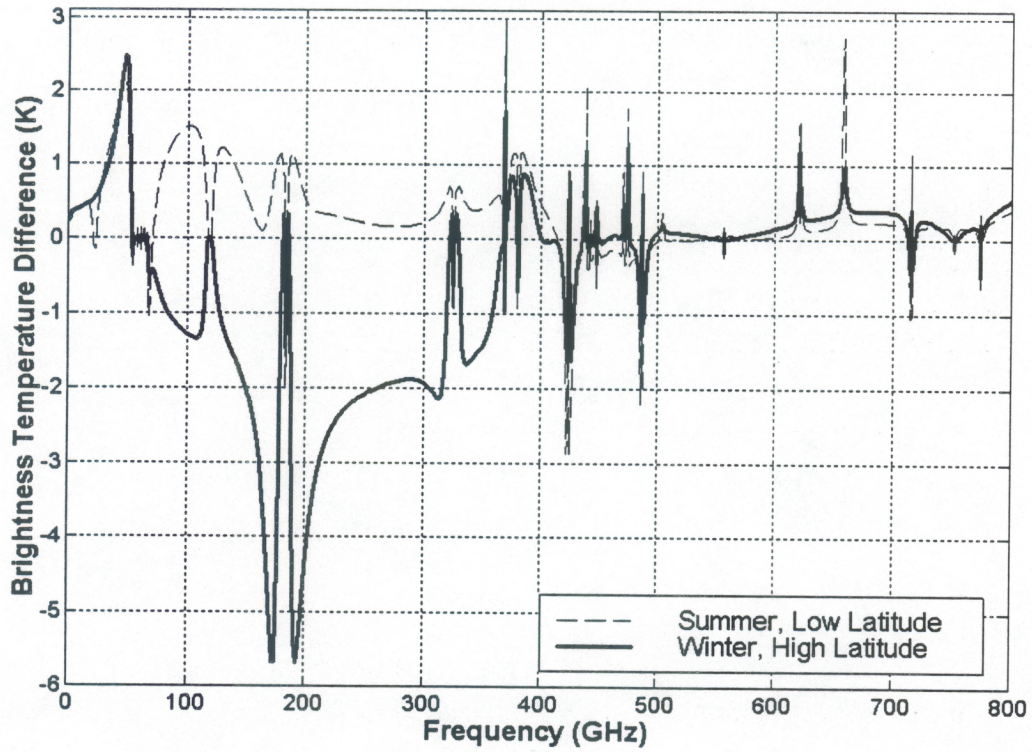

Figure 3. Brightness temperature difference between Rosenkranz and MRT/Liebe absorption models evaluated for nadir satellite view for two extreme atmospheric profiles and ocean background.

To better understand the brightness spectrum differences, consider the attenuation evaluated at the level of one optical depth for the extreme atmospheric cases (Figures 4 and 5). Relative difference R_D (in %) is defined by:

$$R_D = \frac{\tau_{ROS} - \tau_{MRT}}{\tau_{MRT\_TOT}} \times 100 \qquad (10)$$

where τ_{ROS} and τ_{MRT} are the attenuations for a given atmospheric constituent in ($Np\ km^{-1}$) calculated using the Rosenkranz and MRT/Liebe absorption models respectively, and τ_{MRT_TOT} is the total attenuation ($Np\ km^{-1}$) for both water vapor and oxygen evaluated with the MRT/Liebe absorption model. Figure 5 shows that, except for frequencies bellow ~50 GHz, oxygen absorption differs significantly (by ~15%) but only at the absorption line centers and for frequencies above ~368 GHz.

The greatest difference between brightness temperatures calculated using the different methods is ~6°K and occurs in the vicinity of the 183.3101 GHz water vapor absorption line (Figure 3). Only a comparison against measured data can determine which model is more precise. In practice, however, instrumental uncertainties caused by radiometer calibration errors or atmospheric profile measurement errors are usually comparable to the differences between the herein-examined models. Even state-of-the-art radiometer measurements are thus difficult to use to empirically discriminate between these models.

To ensure consistency of the Rosenkranz and MRT/Liebe attenuation models with current line base knowledge the JPL online microwave spectral line catalog [Poynter and Pickett, 1985] was also used for comparison. As can be seen in Table 5, all significant lines from the JPL catalog are included in both the MRT/Liebe and Rosenkranz water vapor absorption models. MRT/Liebe also includes some weak water vapor lines that are not listed in the JPL online catalog, e.g. 67.81396 and 119.99594 GHz. The MRT/Liebe water vapor absorption model has about twice as many absorption lines included as a Rosenkranz model has.

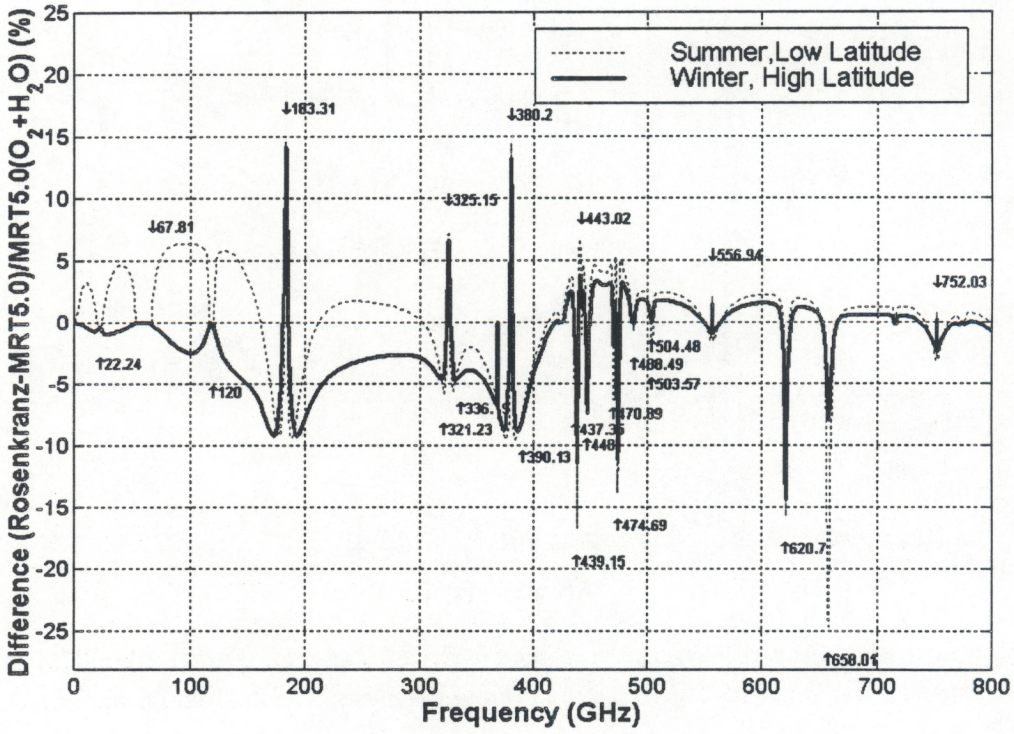

Figure 4. Relative difference spectra of calculated attenuation between Rosenkranz and MRT/Liebe absorption models for water vapor evaluated for two extreme atmospheric states at the level of one optical depth. Arrows point to the centers of the absorption lines.

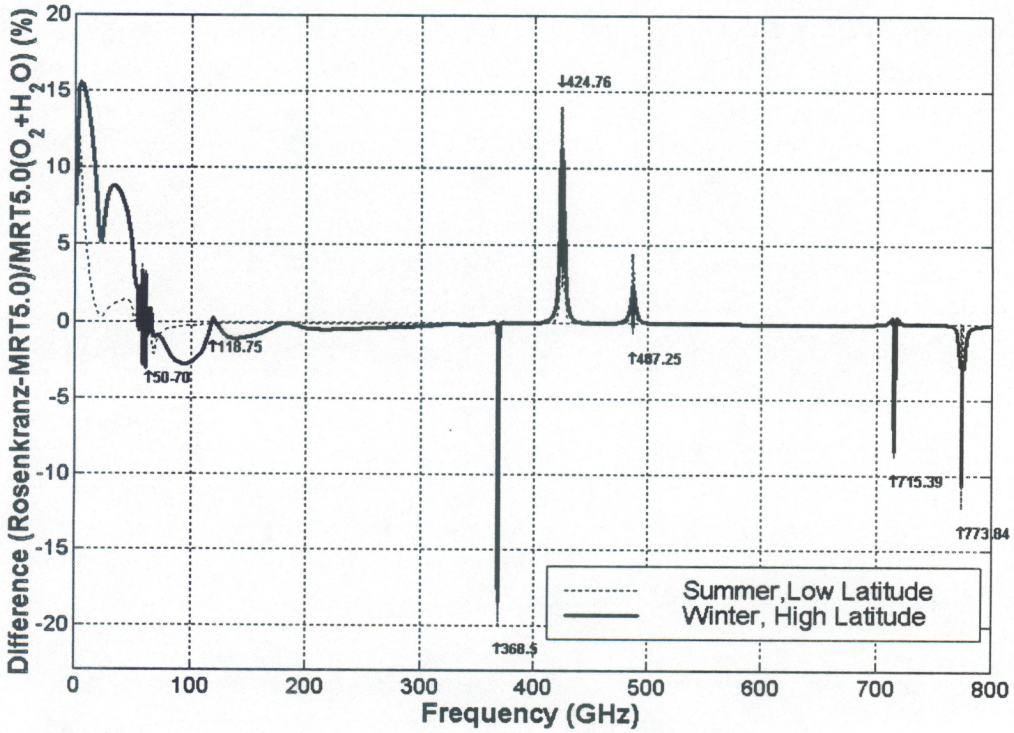

Figure 5. Relative difference spectra of calculated attenuation between Rosenkranz and MRT/Liebe absorption models for oxygen evaluated for two extreme atmospheric states at the level of one optical depth. Arrows point to the centers of the absorption lines.

The comparison in Table 6 shows that MRT/Liebe and Rosenkranz absorption models for oxygen use the same lines. Weaker oxygen absorption lines that are listed in the JPL online catalog are not used in either the MRT/Liebe or the Rosenkranz model, since they are insignificant for this study. For all further calculations presented in this report the MRT/Liebe absorption model was used.

Table 5. Comparison of water vapor absorption line in microwave region

Frequency (MHz) JPL catalog	Line Strength (cm^2Hz) JPL catalog	Frequency (GHz) Rosenkranz	Frequency (GHz) MRT5.0
22235	1.3146e-014	22.2351	22.23508
			67.81396
			119.99594
1.8331e+005	2.2751e-012	183.3101	183.310117
3.2123e+005	8.0742e-014	321.2256	321.225644
3.2515e+005	2.6996e-012	325.1529	325.152919
			336.187000
3.802e+005	2.4423e-011	380.1974	380.197372
3.9013e+005	9.2619e-015		390.134508

Frequency (MHz) JPL catalog	Line Strength (cm^2Hz) JPL catalog	Frequency (GHz) Rosenkranz	Frequency (GHz) MRT5.0
4.3735e+005	1.5024e-013		437.346667
4.3915e+005	2.1812e-012	439.1508	439.150812
4.4302e+005	4.6249e-013	443.0183	443.018295
4.48e+005	2.5651e-011	448.0011	448.001075
4.7089e+005	8.3657e-013	470.8890	470.888947
4.7469e+005	3.2802e-012	474.6891	474.689127
4.8849e+005	6.6988e-013	488.4911	488.491133
5.0357e+005	1.0132e-013		503.568532
5.0448e+005	3.39e-014		504.482692
5.5694e+005	1.5321e-009	556.9360	556.936002
6.207e+005	1.708e-011	620.7008	620.700807
6.4573e+005	7.7321e-015		
6.4587e+005	2.3206e-014		
			658.006500
7.5203e+005	1.0137e-009	752.0332	752.033227
7.668e+005	5.4613e-015		
8.4105e+005	5.9676e-014		841.073593
			859.865000
8.6272e+005	4.7841e-015		
8.6274e+005	1.5948e-015		
			899.407000
			902.555000
9.0621e+005	8.9764e-013		906.205524
9.1617e+005	4.2394e-011	916.1712	916.171582
9.7032e+005	4.7984e-011		970.315022
9.8793e+005	7.357e-010		987.926764

Table 6. Comparison of oxygen absorption line in microwave region

Frequency (MHz) JPL catalog	Line Strength (cm^2 Hz) JPL catalog	Frequency (GHz) Rosenkranz	Frequency (GHz) MRT
44907.0918	8.4528e-025		
45409.1561	4.0402e-024		
45911.794	1.8315e-023		
46415.0628	7.8723e-023		
46919.0273	3.207e-022		
47423.7611	1.2379e-021		
47929.3489	4.5258e-021		
48435.8887	1.5668e-020		
48943.4953	5.1333e-020		
49452.3037	1.5918e-019		
49962.4752	4.6677e-019		
50474.2042	1.2939e-018		
50987.7278	3.3892e-018		
51503.3389	8.3869e-018	51.5034	51.5034
52021.4047	1.9593e-017	52.0214	52.0214
52542.3925	4.3172e-017	52.5424	52.5424
53066.9079	8.9702e-017	53.0669	53.0669
53595.7507	1.7559e-016	53.5957	53.5957
54130.0016	3.2352e-016	54.1300	54.1300
54671.145	5.6027e-016	54.6712	54.6712
55221.372	9.1075e-016	55.2214	55.2214
55783.819	1.3874e-015	55.7838	55.7838
56264.766	8.0408e-016	56.2648	56.2648
56363.393	1.9747e-015	56.3634	56.3634
56968.18	2.617e-015	56.9682	56.9682
57612.4802	3.2129e-015	57.6125	57.6125
58323.885	3.6241e-015	58.3239	58.3239
58446.58	2.2167e-015	58.4466	58.4466
59164.215	3.7042e-015	59.1642	59.1642
59590.978	3.2772e-015	59.5910	59.5910
60306.044	3.3366e-015	60.3061	60.3061
60434.776	3.8735e-015	60.4348	60.4348
61150.57	3.9893e-015	61.1506	61.1506
61800.155	3.7e-015	61.8002	61.8002
62411.223	3.1434e-015	62.4112	62.4112
62486.255	2.4706e-015	62.4863	62.4863
62997.9772	2.4683e-015	62.9980	62.9980
63568.52	1.803e-015	63.5685	63.5685
64127.777	1.2294e-015	64.1278	64.1278

Frequency (MHz) JPL catalog	Line Strength (cm^2 Hz) JPL catalog	Frequency (GHz) Rosenkranz	Frequency (GHz) MRT
64678.8985	7.8487e-016	64.6789	64.6789
65224.0647	4.7011e-016	65.2241	65.2241
65764.744	2.6467e-016	65.7648	65.7648
66302.0821	1.4018e-016	66.3021	66.3021
66836.8204	6.9952e-017	66.8368	66.8368
67369.5887	3.29e-017	67.3696	67.3696
67900.867	1.4598e-017	67.9009	67.9009
68431.005	6.1136e-018		
68960.312	2.4188e-018		
69489.03	9.0427e-019		
70017.3699	3.196e-019		
70545.4815	1.0683e-019		
71073.5108	3.3799e-020		
71601.5781	1.012e-020		
72129.7874	2.8695e-021		
72658.2294	7.7055e-022		
73186.9841	1.9611e-022		
73716.123	4.7315e-023		
74245.7103	1.0827e-023		
74775.804	2.3496e-024		
118750.343	2.9431e-015	118.7503	118.7503
368498.3443	6.4313e-016	368.4984	368.4983
424763.12	7.117e-015	424.7631	424.7631
487249.3755	3.0896e-015	487.2494	487.2494
715393.072	1.7956e-015	715.3932	715.3931
773839.691	1.1639e-014	773.8397	773.8397
834145.7191	4.1267e-015	834.1453	834.1453

4.2. Ocean Surface Model.

All the evaluation of sensitivities is done assuming an ocean surface background. The ocean surface model used in MRT depends on wind speed and ocean temperature and is based on the model described by [*Wilheit*, 1979]. The model frequency dependence for different wind speed and surface temperature conditions is shown in Figure 6. The values of ocean surface temperature are based on *Isemer et al.* [1985] and vary from 275 K for high latitude to 301 K for low latitude region, and the mean wind speed is 7 m/s.

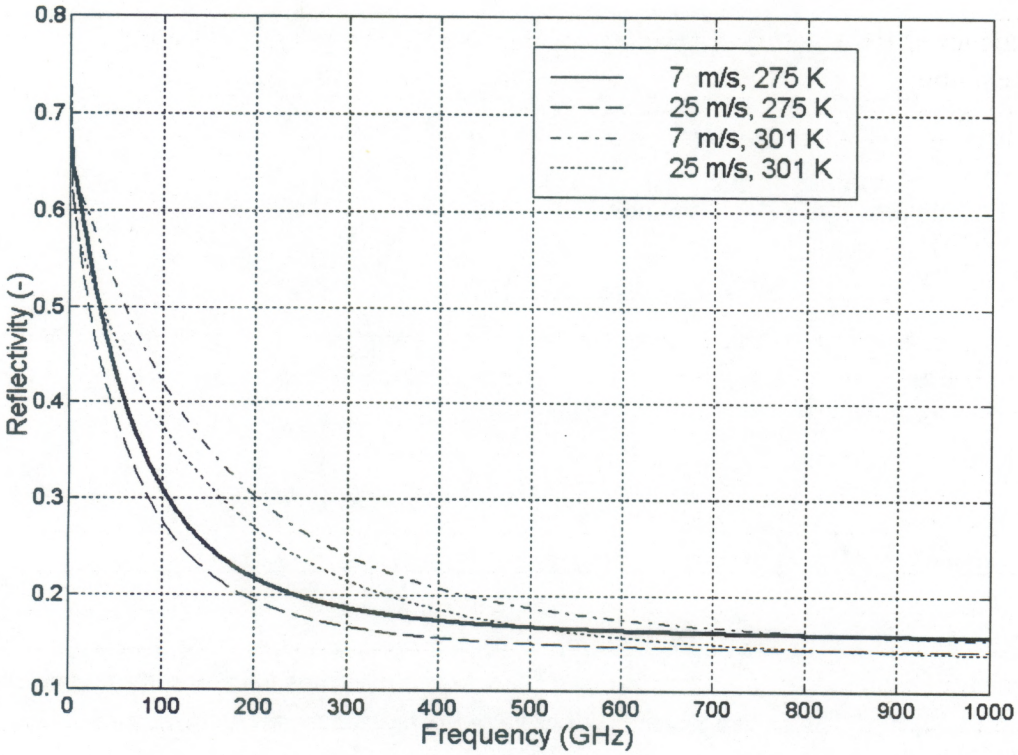

Figure 6. MRT ocean surface model reflectivity frequency dependence for varying wind speed and temperature, for nadir incidence.

4.3. Frequency Grid.

A nonlinear frequency grid was used in calculations for the frequency range form 1 to 1000 GHz. Points are symmetrical around the absorption lines centers and closer together in the vicinity of a line. The lack of a Zeeman splitting model in the MRT/Liebe oxygen absorption model requires excluding line centers frequencies in the frequency grid. Thus frequency points no closer than 2.5 MHz to the line centers are used.

4.4. Discretization and Numerical Integration.

Numerical quadrature in pressure levels is used for the evaluation of the IWFs. Terms such as:

$$\int_z^\infty T_B(f,T(z'))\alpha(f,T(z'),\rho(z'))\sec\theta e^{-\tau(f,z,z')\sec\theta}dz' \tag{11}$$

are calculated by casting the solution into an integral over the transmissivity t:

$$\int_z^\infty T_B(f,T(z'))\alpha(f,T(z'),\rho(z'))\sec\theta e^{-\tau(f,z,z')\sec\theta}dz' = \int_0^1 T(t)dt \tag{12}$$

where t and the opacity $\tau(f,z_1,z_2)$ are:

$$t = e^{-\tau(f, z_1, z_2)} \tag{13}$$

$$\tau(f, z_1, z_2) = \int_{z_1}^{z_2} \alpha(f, T(z), \rho(z)) \sec\theta \, dz \,. \tag{14}$$

The incremental transmissivity dt is evaluated as[4]:

$$dt = \alpha(f, T(z), \rho(z)) \sec\theta \, e^{-\int_{z_1}^{z_2} \alpha(f, T(z'), \rho(z')) \sec\theta \, dz'} \, dz \,, \tag{15}$$

with the Planck law being used to evaluate the brightness temperature at each atmospheric level as well as for the cosmic background and surface. The surface temperature is assumed to be independent of the temperature of the bottom layer of the atmospheric profile.

5. Incremental Weighting Function Statistics.

The IWFs are evaluated for the nadir viewing radiometer located above the atmosphere, at the altitude of 150 km, assuming an ocean background and clear air conditions. No clouds are considered in this study. Figures 8, 14, and 15 (in Appendix A) show the effective water vapor sensing heights $h_{eff,\rho}$ for two extreme climatological cases along with the IWF widths $\sigma_{h,\rho}$ defined by:

$$h_{eff,\rho} = \frac{\int_0^\infty z \left| W_\rho(f, z, \theta) \, \sigma_\rho \right| dz}{\int_0^\infty \left| W_\rho(f, z, \theta) \, \sigma_\rho \right| dz} \tag{16}$$

$$\sigma_{h,\rho} = \sqrt{\frac{\int_0^\infty (z - h_{eff})^2 \left| W_\rho(f, z, \theta) \, \sigma_\rho \right| dz}{\int_0^\infty \left| W_\rho(f, z, \theta) \, \sigma_\rho \right| dz}} \tag{17}$$

In equations (16) and (17) the water vapor IWFs W_ρ were multiplied by the standard deviation profile of water vapor σ_ρ for the appropriate seasons and latitudinal zones. The effective temperature sounding heights $h_{eff,T}$ together with the width $\sigma_{h,T}$ for the same extreme atmospheric situations are shown on Figures 9, 22, and 23 and were evaluated as follows:

$$h_{eff,T} = \frac{\int_0^\infty z \left| W_T(f, z, \theta) \right| dz}{\int_0^\infty \left| W_T(f, z, \theta) \right| dz} \tag{18}$$

---

[4] The detailed description of this method can be found in *Gasiewski, A. J.*, [1993], chapter 3.3.2 "Numerical Quadrature: Nonscattering Solution."

$$\sigma_{h,T} = \sqrt{\frac{\int_0^\infty (z - h_{eff})^2 |W_T(f,z,\theta)| dz}{\int_0^\infty |W_T(f,z,\theta)| dz}} \tag{19}$$

Figure 9 shows the corresponding upwelling brightness temperature variations $\sigma_{TB,\rho}$ due to the natural variation of water vapor in the atmosphere.

$$\sigma_{TB,\rho} = \sqrt{\overline{W}_p^t \overline{\overline{R}}_{pp} \overline{W}_p} \tag{20}$$

where $\overline{W}_p$ is the incremental (column) weighting vector and $\overline{\overline{R}}_{pp}$ is the covariance matrix for parameter p, where p is either water vapor or temperature. The variation σ_{TB} is thus the minimum sensitivity that the radiometer measuring the parameter of interest must possess in order to be able to sense natural atmospheric variations.

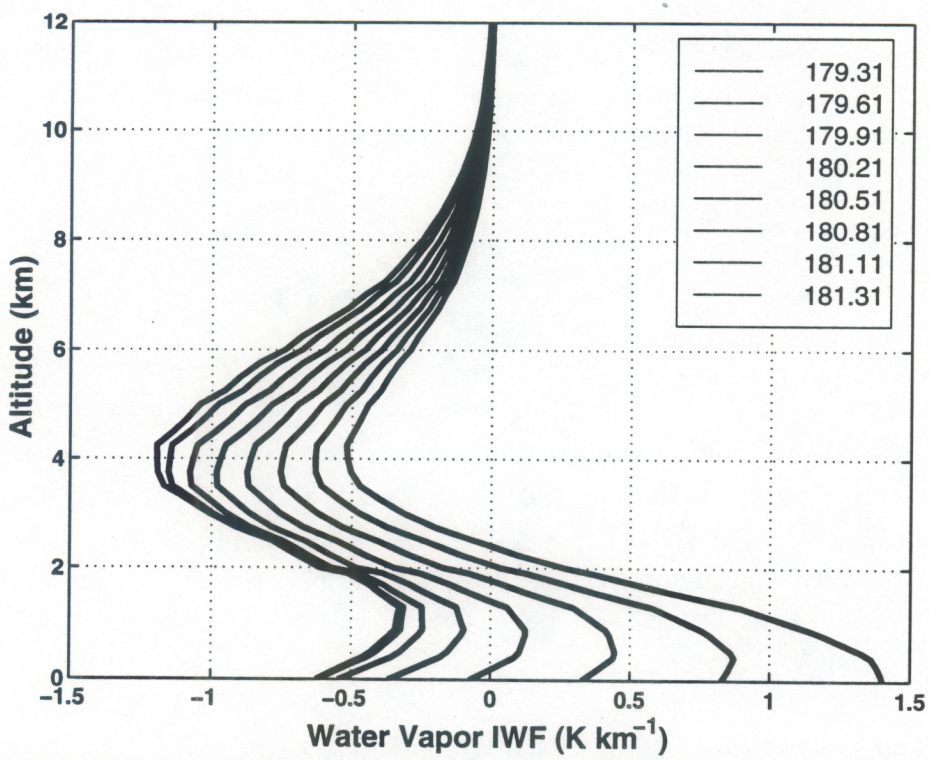

Figure 7. Water vapor IWFs for single frequencies on the lower wing of the 183.3101 GHz absorption line. Numbers in the legend are valid for curves from right to left.

Figures 12, 13, 20, and 21 (in Appendix A) are plots of the brightness temperature variations indexed by sensing height rather than by frequency. Plots are printed separately for each significant absorption line in the frequency range of concern, with the absorption line frequency given above each plot. Both upper and lower wings of each absorption line are plotted, and the bullets, arrows, and numbers show the frequency offset from the center of the absorption line. An interesting feature can be seen in Figures 13a and 13b for the 183.3101 and 325.1529 GHz water vapor absorption lines, and in

Figure 21a for the 118.7503 GHz oxygen absorption line. The effective sensing height monotonically decreases with offset from the line center (e.g. to ~2 GHz for the 183.3101 GHz line) and then increases. At the offset where the change occurs, the upwelling brightness temperature becomes sensitive to the surface reflectivity resulting in a sign change of the IWF at low altitudes (Figure 7). In changing sign, the IWF undergoes a zero crossing which is manifested as an increase in calculated sounding height, as defined by (16).

Figures 13, 14, 17, and 18 are expanded plots of the effective sensing height h_{eff} for the IWF along with the effective height standard deviation σ_h. Here, σ_h is plotted only if the IWF has a distinct peak as defined using the following half power criterion:

$$\left|W_{pMAX}\right| \geq \frac{\sqrt{2}}{2} W_p(f,z,\theta)\Big|_{z=0} \tag{21}$$

where W_{pMAX} is the maximum absolute value of IWF for the given profile and frequency, and $W_p(f,z,\theta)\big|_{z=0}$ is the IWF value at the surface. Those IWF that do not satisfy condition (20) do not have a distinct peak and their standard deviation of effective height σ_h is not plotted. At the centers of some absorption lines the σ_h for the water wapor IWF increases significantly, e.g. Figure 14b at the 380.1974 GHz line. This feature is caused by a secondary IWF peak at higher altitude that is not as well pronounced as the first one, but is strong enough to influence σ_h.

The natural available bandwidth B_N for a given frequency point f can be defined as follows:

$$B_N = f_H - f_L \tag{22}$$

where:

$$\begin{aligned} f_H > f \quad &and \quad h_{eff}(f_H) = h_{eff}(f) \pm \alpha\sigma_h(f) \\ f_L < f \quad &and \quad h_{eff}(f_L) = h_{eff}(f) \pm \alpha\sigma_h(f) \end{aligned} \tag{23}$$

Thus, B_N is the bandwidth available for sounding provided that the effective height is within the limit given by the standard deviation of the effective sounding height $\sigma_h(f)$ times a scaling coefficient α. The value of α selected for the Figures 16, 17, 24, and 25 is 0.25. For the points where σ_h is not defined, B_N is not plotted, for example near the 22.2351 GHz absoption line.

We can now prescribe a minimum signal-to-noise ratio SNR_m necessary to sense natural brightness temperature variations in the presence of radiometer noise. Denoting the radiometer sensitivity as ΔT_{RMS} the minimum SNR becomes:

$$SNR_m = \frac{\sigma_{TB}}{\Delta T_{RMS}}. \tag{24}$$

Since ΔT_{RMS} is fundamentally determined by the radiometer noise characteristics T_{SYS}, the channel bandwidth B, and the integration time τ by

$$\Delta T_{RMS} = \frac{T_{SYS}}{\sqrt{B\tau}}, \tag{25}$$

we can determine the minimum integration time τ_{min} required for unambigious detection of natural atmospheric variations:

$$\tau_{\min}(f) = \frac{T_{SYS}^2(f)}{B_N(f) SNR_m^{\ 2} \sigma_{TB}^2(f)}. \tag{26}$$

As an example, we plot τ_{min} in Figures 21, 22, 25, and 26 for $SNR_m = 10$ (20 dB at the radiometer detector outputs) and $\alpha = 0.25$. The system temperature T_{SYS} is conservatively modelled as:

$$T_{SYS}(f) = \begin{cases} 300K & f < 30GHz \\ 10f & f > 30GHz \end{cases} \tag{27}$$

where f is in units of GHz. Given a value of α, SNR_m, and a receiver noise model, the above time τ_{min} is fundamental in determining the sensing capabilities at any given frequency.

6. Discussion.

There are several motivating factors for vertical sounding of temperature and moisture using microwave channels that are higher in frequency (i.e., ~200 to ~1000 GHz) than those currently employed on satellites. First, water vapor lines in this higher frequency range are generally stronger than those below 200 GHz and it is thus possible to sense at altitudes above the middle troposphere. Second, for diffraction-limited antennas of a given size, improved spatial resolution can be obtained since the spot area decreases with the square of the frequency. Third, the scattering coefficient α_S for spherical Rayleigh ice cloud particles follows $f^4 a^6$ where f is the frequency and a is the particle diameter, see, e.g., *Gasiewski* [1993], p.102. A result of this sharp increase of α_S with frequency (Tables 9 and 10) is the potential to measure cirrus cloud ice water path. This possibility was first discussed by *Gasiewski* [1993] within the context of submillimeter-wave radiometry and by *Evans et al.* [In press] using Fourier transform spectrometry.

The primary disadvantages of using frequencies in this range include the adverse effects of increased cloud opacity on water vapor sounding. However, this disadvantage can be partially offset by using sets of water vapor sounding bands spaced approximately one to three octaves apart. Other disadvantages of using higher frequency channels are associated with the higher water vapor continuum absorption that obscures the lower troposphere under all but high latitude or winter conditions. Finally, the nascent receiver and detector technology at submillimeter wave frequencies results in higher system noise temperatures.

An overview of the anticipated sounding capabilities for the millimeter- and submillimeter-wave frequency range considered in this paper is shown in Figures 8 through 11 and summarized for the most significant water vapor and oxygen absorption lines in Tables 9 and 10. More detailed plots showing the sounding capabilities of the most significant water vapor and oxygen absorption lines are shown in Appendix A, Figures 12 through 27. These plots can be used to determine the clear-air microwave sounding capabilities for a particular atmospheric level.

As an example, consider the sounding of water vapor in the upper stratosphere between 30 and 40 km altitudes. Using Figures 14 and 15, one can determine suitable water vapor absorption lines by requiring that the range of effective sensing heights span this altitude range. For this example, lines at 556.9360, 752.0332, and 987.9268 GHz are suitable. Using Figures 12c, 12d, 12e and 13c, 13d, 13e it can be seen that for these three lines we require frequencies approximately ±80, ±100, and ±80 MHz from the line centers, respectively. The variation of brightness temperature due to the natural variation of water vapor

at these frequencies and altitudes is ~0.2 K for summer and low latitudes and ~0.3-0.4 K for winter and high latitudes, thus requiring exceptional radiometric stability. The natural available bandwidth can be determined, using Figures 16c, 16d, 16e and 17c, 17d, 17e, to be ~20 MHz for all three lines and both extreme atmospheric conditions. Assuming a total power radiometer and requiring an SNR of 20 dB, the necessary integration time would be ~10^3 to ~10^4 sec, as determined from Figures 18c, 18d, 18e and 19c, 19d, 19e. Thus, a state-of-the-art microwave radiometer for vertical sounding of moisture in the upper stratosphere must be geostationary to provide adequate sensitivity.

6.1. Channels for Water Vapor Sounding.

Seasonally and latitudinally varying amounts of moisture cause significant variation in sounding altitudes. For the two extreme cases considered, the vertical moisture content varies by more than one order of magnitude, resulting in the effective height for the same frequency varying by a factor of nearly 2. The variability of water, along with the nonlinear relationship of the brightness temperature with moisture content, indicates the necessity of nonlinear or geographically and seasonally indexed water vapor retrieval methods. The brightness temperature standard deviation σ_{TB} is also influenced by the season, latitude, and diurnal phase, and should be similarly indexed within retrieval algorithms. It must also be noted that water vapor sounding requires an accurate knowledge of the temperature profile around the altitude of interest, and thus cannot practically be performed independent of temperature sounding.

Tables 9 and 10 in Appendix A summarize the sounding capabilities for frequencies from 89 through 557 GHz. This range spans the frequency bands currently being considered for use on the NASA/NOAA Advanced Geosynchronous Sensor satellite [*Adler*, 1998], and specifically includes those allocated for passive sensing on either primary or shared basis [*NTIA*, 1995]. For each frequency the effective sounding height h_{eff} is listed for the two extreme atmospheric conditions, along with natural available bandwidth B_N, minimum integration time τ_m, and subsatellite 3 dB footprint diameter assuming a circular, uniformly illuminated, aperture antenna on either a low-Earth orbiting (LEO) or geosynchronous (GEO) sensor. For the LEO sensor a 0.5 m diameter aperture at an altitude of 833 km (the Defense Meteorological Satellite Program (DMSP) satellites' orbital altitude) is assumed, and for the GEO sensor a 2-m diameter at an altitude of 35 782 km is assumed. An equatorial spatial resolution of ~20 km or better can be achieved using channels above ~320 GHz. Such resolution is adequate for a variety of synoptic applications, including severe weather mapping, nowcasting and forecasting, atmospheric dynamics research, and numerical weather prediction (NWP) model initialization. Additional improvements in resolution (by ~15-25%) might be obtained by the use of antenna pattern deconvolution techniques.

The water vapor absorption lines at 325.1529, 380.1974, 448.0011, and 556.9360 GHz as well as windows in between them at ~318, ~341, ~410, and ~492 GHz are thus good candidates for moisture sounding. The available effective sounding heights vary from ~6.5 km to the upper stratosphere at ~40 km, although for the highest altitudes the minimum integration time exceeds one hour. In order to achieve comparable resolution using lower frequencies around the 183.3101 GHz absorption line, however, the required aperture diameter increases to ~4 m for geostationary orbit. Since sensor cost is driven to a large extent by aperture size and varying as size to the power of approximately three, the cost savings from using higher frequencies is considerable. None of these frequencies can directly probe

emissions from the surface except under winter high-latitude conditions. For high-resolution water vapor sounding in the lower to middle troposphere it is thus considered necessary to use one or several low orbiting sensors operating around the 183.3101 GHz line and in the window at ~142 GHz, albeit with significant compromises in temporal resolution.

With regard to the 183.3101 GHz line it is noted that the IWF's at the International Telecommunication Union (ITU) allocated frequency bands of 150-151 and 164-168 show distinct differences in the peak response height and sign (Figure 14a and 15a). These two channels are far enough apart from each other relative to their offset from the 183 GHz line center to warrant being used simultaneously for water vapor sounding, particularly if equivalent vertical sensitivity in both warm moist and cold dry climates are of concern. The fact that current systems do not use both is a technological shortcoming that could be corrected in future systems, with e.g. broadband Monolithic Microwave Integrated Circuit (MMIC) receiver. If one considers a progression of sidebands spaced at successive octaves from the 183.3101 GHz line center (and hence at progressively lower opacities) and starting with a 1 GHz offset, one can obtain approximately the following sequence of offsets: 1,3,7,17,33. These offsets coincide with 182, 180, 176, 166, and 150 GHz. Since 150 GHz is close to the center of the absorption minimum between 118 and 183 GHz, a set that includes both 150 and 166 GHz is warranted purely from the standpoint of being able to observe at a variety of well-distributed levels of opacity around the 183 GHz line.

6.2. Channels for Temperature Sounding.

Since oxygen is much more uniformly mixed in the atmosphere than water vapor, the seasonal and latitudinal variations in the effective sounding height for temperature are considerably smaller than for water vapor (Figure 9). Indeed, most such variation in sounding height occurs for altitudes in the lower troposphere and is the result of water vapor absorption dominating the spectrum in the wings of the O_2 lines. Thus, a similar situation to the above applies in that temperature sounding cannot practically be performed independent of water vapor sounding, particularly in the lower-to-middle troposphere.

From Table 10, suitable channel sets for temperature sounding are available around several O_2 lines or bands, including 50-70 GHz, 118.7503, 368.4983, 424.6891, and 487.2494 GHz. The corresponding sounding altitudes can range from near the surface to ~40 km. (Since Zeeman splitting is not included in the oxygen absorption model used in this study, sounding at altitudes above ~40 km altitude is not considered.) A significant difference exists in the frequency sensitivity of the effective height for water vapor and temperature sounding, with the greater sensitivity seen in the temperature sounding channels. One result of this difference is that the natural available bandwidth for temperature sounding channels is significantly smaller (by approximately one order of magnitude) than for water vapor channels of comparable sounding height. The channel bandwidths for stratospheric temperature sounding are restricted to only a few MHz. The minimum integration times are, however, shorter than for water vapor sounding since $\sigma_{TB,T} >> \sigma_{TB,\rho}$.

Temperature sounding using the submillimeter wave O_2 lines at 368.4983, 424.6891, or 487.2494 GHz can provide considerably higher spatial resolution than that available using the 50-70 GHz band or the 118.7503 GHz line. Use of these submillimeter lines should include window channels at ~342, ~407, and ~464 GHz (respectively) to provide the best possible low-altitude sensitivity.

6.3. Geosynchronous Sensing.

For geosynchronous sounding and imaging it is suggested that a suite of several channels around the following window, water line, and oxygen line frequencies would provide good vertical coverage from the surface to the lower stratosphere with good spatial resolution down through the middle troposphere. A combination of channels at the 118.7503 GHz and 424.7631 GHz lines provides vertical temperature coverage nearly comparable to that of the 50-60 GHz band, but with spatial resolution adequate for GEO imaging and observable degrees of freedom related to cloud absorption and scattering. Similarly, a combination of channels at the 183.3101 GHz water vapor line and another submillimeter wave water vapor line provides adequate vertical water vapor coverage, useful GEO spatial resolution, and additional spectral degrees of freedom necessary to compensate water vapor soundings for clouds:

a) 118.7503/150/166/183.3101 GHz (for cloud penetrability, temperature and water vapor profiling, and water vapor observational heritage);

b) 220/325.1529 or 340/380.1974 GHz or 410/448.0011 (for cloud detection and high spatial resolution, here, 380.1974 or 448.0011 GHz would provide unique upper troposphere/lower stratosphere water vapor sensitivity);

c) 410/424.7631 GHz (for temperature profiling and high spatial resolution raincell mapping).

Several channels in the vicinity of the 556.9360, 752.0332, and 987.9268 GHz water vapor lines would provide better high-altitude cirrus cloud detectability and the capability for middle-to-upper stratospheric water vapor sounding, but at considerably lower temporal resolution. The mapping of deeply convective storm tops, however, would require much less radiometric precision and the improvements in spatial resolution available from such channels might warrant their inclusion.

References:

1976 US std. Atmosphere: United States Committee on Extension to the Standard Atmosphere:"U.S. standard atmosphere, 1976", Washington: National Oceanic and Atmospheric Administration, 1976

Adler, R. F. Science benefits of advanced geosynchronous observation, NASA Goddard Space Flight Center, 1998, in press.

Chedin, A., Scott, N. A., Wahiche, C., and Mouliner, P., The improved initialization inversion method, A high resolution physical method for temperature retrievals from satellites of the TIROS-N series, *J. of Climate and Appl. Meteor.*, 24, 128-143, February 1985.

Cheury, F., Chevallier, F., Scott, N. A., Chedin, A., A new generation of radiative transfer models for climate studies based on neural networks, *IGARSS'* 1995.

Chiou, E. W., McCormick, M. P., and Chu, W. P., Global water vapor distribution in the stratosphere and upper troposphere derived from 5.5 years of SAGE II observations, *J. Geophys. Res.*, 102, D15, 19,105-19,118, August 20, 1997.

Evans, K. F., Stephens, G. L., A new polarized atmospheric radiative transfer model, *J. Quant. Spectr. and Rad. Trans.*, 46, 5, 413-423, November 1991.

Evans, K. F., Evans, A. H., Marshall, B. T., Nolt, I. G., The prospect for remote sensing of cirrus clouds with a submillimeter-wave spectrometer, *J. Appl. Meteor.*, in press.

Francois, C., Ottle, C., Atmospheric corrections in the thermal infrared, global and water vapor dependent split-window algorithms-applications to ATSR and AVHRR data, *IEEE Trans. on Geosci. Remote Sens.*, 34, 2, 457-470, March 1996.

Gasiewski, A. J., and Staelin, D. H., Numerical modeling of passive microwave O_2 observations over precipitation, *Radio Sci.*, 25, 3, 217-235, May-June 1990.

Gasiewski, A. J., Numerical sensitivity analysis of passive EHF and SMMW channels to tropospheric water vapor, clouds, and precipitation, *IEEE Trans. on Geosci. Remote Sens.*, 30, 5, 859-870, September 1992.

Gasiewski, A. J., Microwave radiative transfer in hydrometeors, in *Atmospheric Remote Sensing by Microwave Radiometry*, edited by Janssen, M. A., Wiley & Sons, New York, 1993, ch. #3.

Isemer, H. J., Bunker, A. F., Hasse, L. The Bunker Climate Atlas of the North Atlantic Ocean", Berlin, New York, Springer-Verlag, 1985.

Jackson, D. M., Gasiewski, A. J., Millimeter-wave radiometric observation of the troposphere: A comparison of measurements and calculations based on radiosonde and Raman lidar, *IEEE Trans. on Geosci. Remote Sens.*, 33, 1, 3-14, January 1995.

Liebe, H. J., An atmospheric millimeter wave propagation model, NTIA Report 83-137, U.S. Department of Commerce, December 1983.

Liebe, H. J., A contribution to modeling atmospheric millimeter-wave properties, *Frequenz*, 41, 1-2, 31-36, January-February 1987.

Nedoluha, G. E., Bevilacqua, R. M., Gomez, R. M., Siskind, D. E., Hicks, B. C., Russell, Increases in middle atmospheric water vapor as observed by HALOE and ground-based water vapor millimeter-wave spectrometer from 1991-1997, *J. Geophys. Res.*, submitted for publication

NTIA Tables of frequency allocation and other extract from: *Manual of Regulations and Procedures for Federal Radio Frequency Management*, U.S. Department of Commerce, National Telecommunications and Information Administration, September 1995.

Poynter, R. L., Pickett, H. M., 1985, Submillimeter, millimeter, and microwave spectral line catalog, *Appl. Opt.*, 24, 14, 2235-2240, July 1985.

Rosenkranz, P. V., Absorption of microwaves by atmospheric gases, in *Atmospheric Remote Sensing by Microwave Radiometry*, edited by Janssen, M. A., 37-90, John Wiley & Sons, New York, 1993.

Russel, J.M. III, L. L. Gordley, J. H. Park, S. R. Drayson, W. D. Hesketh, R. J. Cicerone, A. F. Tuck, J. E. Frederick, J. E. Harries, P. J. Crutzen, The halogen occultation experiment, *J. Geophys. Res.*, 98, D6, 10, 777-10 797, June 20, 1993.

Staelin, D. H., Kerekes, J. P., Solman, F. J. III, Geosynchronous microwave sounder working group: Final report, Massachusetts Institute of Technology, Lincoln Laboratory, Lexington, Mass., August 22, 1997.

Westwater, E. R., Snider, J. B., and Falls, M. J., Ground-based radiometric observation of atmospheric emission and attenuation at 20.6, 31.65, and 90.0 GHz: A comparison of measurements and theory, *IEEE Trans. on Geosci. Remote Sens.*, 38, 10, 1569-1580, October 1990.

Wilheit, T. T., Jr., A model for the microwave emissivity of the ocean's surface as a function of wind speed, *IEEE Trans. Geosci. Electron.*, GE-17, 4, 244-249, October 1979.

APPENDIX A

Derivation of the Incremental Weighting Function.

To characterize the sensitivity of the radiometric temperature to a given geophysical parameter it is essential to develop an incremental weighting function. The radiative transfer equation for a downward looking radiometer in the absence of scattering can be expressed as follows:

$$T_B(f,z,\theta)=\int_0^h T_B(f,T(z))\,\alpha(f,T(z),\rho(z))\sec\theta\, e^{-\tau(f,z,h)\cdot\sec\theta}dz+e^{-\tau(f,0,h)\cdot\sec\theta}\cdot$$
$$\cdot\left\{\begin{array}{l}(1-r_\beta(\theta))T_B(f,T_S)+\\ +r_\beta(\theta)\left[\begin{array}{l}\int_0^\infty T_B(f,T(z))\alpha(f,T(z),\rho(z))\sec\theta\, e^{-\tau(f,0,z)\cdot\sec\theta}dz+\\ +T_B(f,T_{CB})\,e^{-\tau(f,0,\infty)\cdot\sec\theta}\end{array}\right]\end{array}\right\} \qquad (1)$$

where T_B is brightness temperature (K),
f is frequency (Hz)
θ is observation angle from nadir (deg)
α is total absorption (Np/km)
$T(z)$ is physical temperature at the atmospheric layer z (K)
ρ (z) is water vapor density (g/m^3)
h is observation height (m)
r_β is surface reflection coefficient(-)
T_S is surface temperature (K)
T_{CB} is cosmic background temperature (K),

$$\tau(f,z_1,z_2)=\int_{z_1}^{z_2}\alpha(f,T(z'),\rho(z'))dz'$$

is attenuation between level z_1 and z_2, and

$$T_B=\frac{h\cdot f}{K\cdot\left(e^{\frac{h\cdot f}{K\cdot T}}-1\right)}$$

is equivalent radiometric temperature (or brightness temperature) for a black body at temperature T, as given by the Planck law.

The first term of the equation represents the upwelling atmospheric radiation from above the surface to the radiometer height h, the second term consists of three terms where the first is surface emission, the second is reflected emissions from the all levels of atmosphere above surface, and the third is the cosmic background contribution.

Consider changing the water vapor density $\rho(z)$ at height level z by a small amount $\delta\rho(z)$:

$$\rho(z) = \rho^0(z) + \delta\rho(z)$$

Then the brightness temperature also changes by a small amount δT_B:

$$T_B(f,h,\theta) = T_B^0(f,h,\theta) + \delta T_B$$

In order to know at what height a change in water vapor would impact T_B we desire an expression of the following form:

$$\delta T_B = \int_0^\infty W_\rho(f,z,\theta)\,\delta\rho(z)dz$$

In this expression $W_\rho(f,z,\theta)$ is the incremental water vapor weighting function.

To find $W_\rho(f,z,\theta)$, a perturbation approach is used. For the upward looking radiometer the radiative transfer equation is:

$$T_B^{\downarrow}(f,z,\theta) = \int_h^\infty T_B(f,T(z))\alpha(f,T(z),\rho(z))\sec\theta\, e^{-\tau(f,h,z)\sec\theta}dz + T_B(f,T_{CB})\,e^{-\tau(f,h,\infty)\sec\theta}$$

By perturbing $\rho(z)$ and collecting only first order perturbations in $T_B^{\downarrow}$ we have:

$$T_B^{\downarrow}(f,z,\theta) \cong \int_h^\infty T_B(f,T(z))\left(\alpha(f,T(z),\rho(z)) + \left.\frac{\partial\,\alpha(f,T(z),\rho(z))}{\partial\rho}\right|_{\rho^0(z)}\delta\rho(z)\right)\sec\theta\, e^{-\tau(f,h,z)\sec\theta}\cdot$$

$$\cdot\left[1 - \int_h^z \left.\frac{\partial\,\alpha(f,T(z'),\rho(z'))}{\partial\rho}\right|_{\rho^0(z')}\delta\rho(z)\sec\theta\,dz'\right]dz +$$

$$+ T_B(f,T_{CB})\,e^{-\tau(f,h,\infty)\sec\theta}\left[1 - \int_h^\infty \left.\frac{\partial\,\alpha(f,T(z),\rho(z))}{\partial\rho}\right|_{\rho^0(z)}\delta\rho(z)\sec\theta\,dz\right]$$

$$\cong \int_h^\infty T_B(f,T(z))\alpha(f,T(z),\rho(z))\sec\theta\, e^{-\tau(f,h,z)\sec\theta}dz + T_B(f,T_{CB})e^{-\tau(f,h,\infty)\sec\theta} +$$

$$+ \int_h^\infty T_B(f,T(z))\left.\frac{\partial\,\alpha(f,T(z),\rho(z))}{\partial\,\rho(z)}\right|_{\rho^0(z)}\delta\rho(z)\sec\theta\, e^{-\tau(f,h,z)\sec\theta}dz -$$

$$- \int_h^\infty T_B(f,T(z))\alpha(f,T(z),\rho(z))\sec\theta\, e^{-\tau(f,h,z)\cdot\sec\theta}\int_h^z \left.\frac{\partial\,\alpha(f,T(z'),\rho(z'))}{\partial\,\rho}\right|_{\rho^0(z')}\delta\rho(z')\sec\theta\,dz'dz -$$

$$- T_B(f,T_{CB})e^{-\tau(f,h,\infty)\sec\theta}\int_h^\infty \left.\frac{\partial\,\alpha(f,T(z),\rho(z))}{\partial\,\rho}\right|_{\rho^0(z)}\delta\rho(z)\sec\theta\,dz \qquad (2)$$

In the fourth term change in order of integration from order 1 to order 2 can be done as shown in Figure A1:

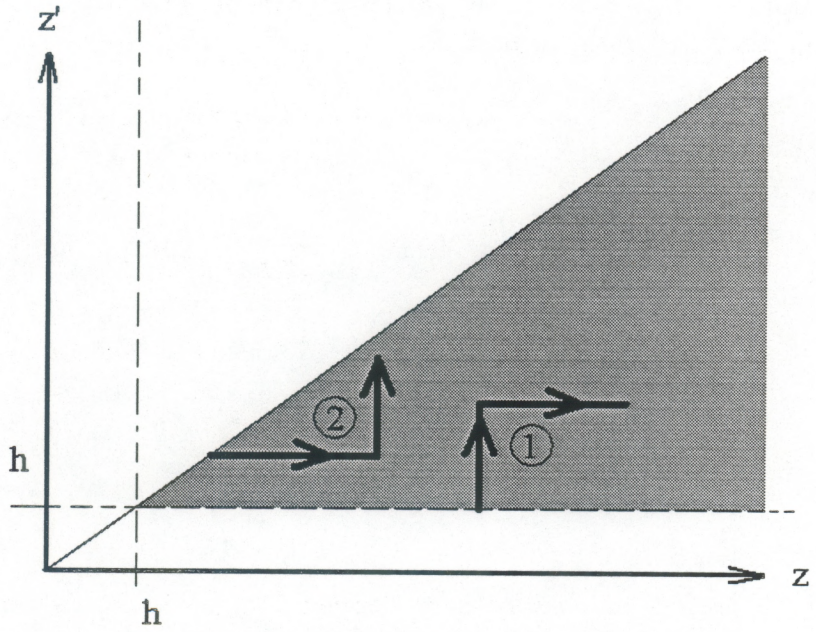

Figure A1: Change of integration order.

$$\int_h^\infty T_B(f,T(z))\alpha(f,T(z),\rho(z))\sec\theta e^{-\tau(f,h,z)\sec\theta}\int_h^z \left.\frac{\partial\,\alpha(f,T(z'),\rho(z'))}{\partial\,\rho}\right|_{\rho^0(z')}\delta\rho(z')\sec\theta\,dz'dz =$$

$$=\int_h^\infty \left.\frac{\partial\,\alpha(f,T(z),\rho(z))}{\partial\,\rho}\right|_{\rho^0(z)}\delta\rho(z)\sec^2\theta\int_z^\infty T_B(f,T(z'))\alpha(f,T(z'),\rho(z'))e^{-\tau(f,h,z')\sec\theta}\,dz'dz$$

The first two terms in equation (2) are the unperturbated terms:

$$T_B^{0\downarrow}=\int_h^\infty T_B(f,T(z))\alpha(f,T(z),\rho(z))\sec\theta e^{-\tau(f,h,z)\sec\theta}\,dz+T_B(f,T_{CB})e^{-\tau(f,h,\infty)\sec\theta}$$

After evaluating terms in the above, equation (2) can now be rewritten:

$$=T_B^{0\downarrow}+\int_h^\infty T_B(f,T(z))\left.\frac{\partial\,\alpha(f,T(z),\rho(z))}{\partial\,\rho(z)}\right|_{\rho^0(z)}\delta\rho(z)\sec\theta e^{-\tau(f,h,z)\sec\theta}\,dz-$$

$$-\int_h^\infty \left.\frac{\partial\,\alpha(f,T(z),\rho(z))}{\partial\,\rho}\right|_{\rho^0(z)}\delta\rho(z)\sec^2\theta\int_z^\infty T_B(f,T(z'))\alpha(f,T(z'),\rho(z'))e^{-\tau(f,h,z')\sec\theta}\,dz'dz-$$

$$-T_B(f,T_{CB})e^{-\tau(f,h,\infty)\sec\theta}\int_h^\infty \left.\frac{\partial\,\alpha(f,T(z),\rho(z))}{\partial\,\rho}\right|_{\rho^0(z)}\delta\rho(z)\sec\theta\,dz=$$

$$=T_B^{0\downarrow}+\int_h^\infty W_\rho(f,z,\theta)\delta\rho(z)dz$$

It is now possible to identify the incremental water vapor weighting function for an upward looking radiometer at height h easily - by inspection:

$$W_\rho(f,z,\theta)=T_B(f,T(z))\left.\frac{\partial\,\alpha(f,T(z),\rho(z))}{\partial\,\rho}\right|_{\rho^0(z)}\sec\theta\,e^{-\tau(f,h,z)\sec\theta}-$$

$$-\left.\frac{\partial\,\alpha(f,T(z),\rho(z))}{\partial\,\rho}\right|_{\rho^0(z)}\sec^2\theta\int_z^\infty T_B(f,T(z'))\alpha(f,T(z'),\rho(z'))e^{-\tau(f,h,z')\sec\theta}dz'-$$

$$-T_B(f,T(z))e^{-\tau(f,h,\infty)\sec\theta}\left.\frac{\partial\,\alpha(f,T(z),\rho(z))}{\partial\,\rho}\right|_{\rho^0(z)}\sec\theta$$

The second term can be rewritten:

$$\left.\frac{\partial\,\alpha(f,T(z),\rho(z))}{\partial\,\rho}\right|_{\rho^0(z)}\sec^2\theta\int_z^\infty T_B(f,T(z'))\alpha(f,T(z'),\rho(z'))\,e^{-\tau(f,h,z')\sec\theta}dz'=$$

$$=\left.\frac{\partial\,\alpha(f,T(z),\rho(z))}{\partial\,\rho}\right|_{\rho^0(z)}\sec^2\theta\int_z^\infty T_B(f,T(z'))\alpha(f,T(z'),\rho(z'))\,e^{-[\tau(f,h,z)+\tau(f,z,z')]\sec\theta}dz'=$$

$$=\left.\frac{\partial\,\alpha(f,T(z),\rho(z))}{\partial\,\rho}\right|_{\rho^0(z)}\sec^2\theta\,e^{-\tau(f,h,z)\sec\theta}\int_z^\infty T_B(f,T(z'))\alpha(f,T(z'),\rho(z'))e^{-\tau(f,z,z')\sec\theta}dz'$$

Thus, the final form of the incremental water vapor weighting function for an upward looking radiometer is:

$$W_{\rho_v}^{\downarrow}(f,z,\theta)=\left.\frac{\partial\,\alpha(f,T(z),\rho(z))}{\partial\,\rho}\right|_{\rho^0(z)}\sec\theta\,e^{-\tau(f,h,z)\sec\theta}\cdot$$

$$\cdot\left\{\begin{aligned}&T_B(f,T(z))-T_B(f,T_{CB})e^{-\tau(f,z,\infty)\sec\theta}-\\&-\int_z^\infty T_B(f,T(z'))\alpha(f,T(z'),\rho(z'))\sec\theta\,e^{-\tau(f,z,z')\sec\theta}dz'\end{aligned}\right\}$$

where the units are e.g. $\left(K\ km^{-1}\ g^{-1}\ m^3\right)$.

Table 9: Moisture sounding capabilities of selected window and water vapor line frequencies.

f (GHz)	h_{eff} (summer, low) (km)	h_{eff} (winter, high) (km)	B_N (MHz)	τ_{min} (s)	3 dB Spot size diameter LEO (km)	3 dB Spot size diameter GEO (km)	Relative Rayleigh Scattering Coefficient
89.0	2.4	1.9			7.15	76.98	1.0
141.8	1.9	1.8			4.49	48.31	6.4
151.0	2.2	1.8			4.21	45.37	8.3
166.0	4.8	1.8			3.83	41.27	12.1
180.3	7.7	4.6	7.7E+02	1.5E-02	3.53	38.00	16.8
182.3	9.9	5.3	3.7E+02	1.4E-02	3.49	37.58	17.6
183.1	11.4	6.0	3.7E+02	1.1E-02	3.48	37.42	17.9
219.3	5.0	1.7	8.5E+04	4.0E-04	2.90	31.24	36.9
318.2	6.5	3.0	3.0E+03	1.0E-02	2.00	21.53	163.3
322.2	7.9	4.1	1.0E+03	2.2E-02	1.98	21.27	171.7
324.2	9.8	5.3	3.7E+02	4.8E-02	1.96	21.14	176.0
325.0	11.3	6.0	3.7E+02	5.4E-02	1.96	21.08	177.8
341.5	6.2	2.2	2.1E+04	2.0E-03	1.86	20.06	216.8
373.2	8.7	5.0	1.7E+03	3.5E-02	1.71	18.36	309.2
377.2	10.7	6.3	7.0E+02	6.4E-02	1.69	18.16	322.6
379.2	12.8	7.8	3.0E+02	1.2E-01	1.68	18.07	329.5
380.2	18.0	15.4	4.0E+00	8.8E+01	1.67	18.02	333.0
410.2	7.0	4.0	2.3E+04	6.0E-03	1.55	16.70	451.3
441.0	9.0	5.1	2.0E+03	3.9E-02	1.44	15.54	602.8
445.5	10.4	6.1	7.3E+02	9.4E-02	1.43	15.38	627.8
447.0	12.6	7.7	2.8E+02	2.0E-01	1.42	15.33	636.3
448.0	18.7	16.6	3.5E+00	2.2E+02	1.42	15.29	642.0
492.5	8.6	4.9	1.1E+04	1.2E-02	1.29	13.91	937.7
540.0	11.9	7.4	3.7E+03	3.4E-02	1.18	12.69	1355.2
550.0	14.0	8.9	1.5E+03	2.2E-01	1.16	12.46	1458.4
554.0	15.8	10.8	5.0E+02	1.4E+01	1.15	12.37	1501.3
556.0	20.2	19.8	1.3E+02	6.6E+03	1.14	12.32	1523.1
556.7	32.2	31.4	4.0E+01	1.8E+03	1.14	12.31	1530.8
556.9	62.8	60.0	1.3E+00	4.6E+04	1.14	12.30	1533.0

Table 10: Temperature sounding capabilities of selected windows and oxygen line frequencies.

f (GHz)	h_{eff} (summer, low) (km)	h_{eff} (winter, high) (km)	B_N (MHz)	τ_{min} (s)	3 dB Spot size diameter LEO (km)	3 dB Spot size diameter GEO (km)	Relative Rayleigh Scattering Coefficient
89.0	2.5	3.0			7.15	76.98	1.0
111.8	5.9	7.8			5.69	61.28	2.5
115.8	7.5	6.6	2.2E+03	1.8E-02	5.50	59.16	2.9
117.8	11.2	9.1	2.7E+02	2.4E-03	5.40	58.16	3.1
118.7	44.8	42.8	1.1E+00	1.3E+00	5.36	57.72	3.2
341.5	5.0	3.1	2.1E+04	3.3E-03	1.86	20.06	216.8
362.5	5.9	3.4	4.4E+03	1.8E-02	1.76	18.90	275.2
365.5	6.4	3.8	1.2E+03	6.0E-02	1.74	18.74	284.4
367.5	8.0	5.6	3.8E+02	2.1E-01	1.73	18.64	290.7
368.5	34.3	32.5	1.7E+00	3.8E+01	1.73	18.59	293.9
407.2	6.0	3.5	1.9E+04	5.0E-03	1.56	16.82	438.2
417.8	6.5	4.2	4.2E+03	1.6E-02	1.52	16.40	485.6
421.8	8.3	6.2	9.0E+02	1.1E-01	1.51	16.24	504.5
423.8	13.6	11.4	1.8E+02	3.6E-01	1.50	16.17	514.1
424.8	48.5	46.2	1.0E+00	4.8E+01	1.50	16.13	519.0
464.2	7.1	3.9	1.1E+04	1.1E-02	1.37	14.76	740.0
480.2	7.6	4.3	5.9E+03	2.1E-02	1.33	14.27	847.5
484.2	8.2	5.2	1.4E+03	7.3E-02	1.31	14.15	876.1
486.2	11.5	8.9	2.3E+02	4.5E-01	1.31	14.09	890.6
487.2	45.1	43.1	1.1E+00	6.7E+01	1.31	14.06	898.0

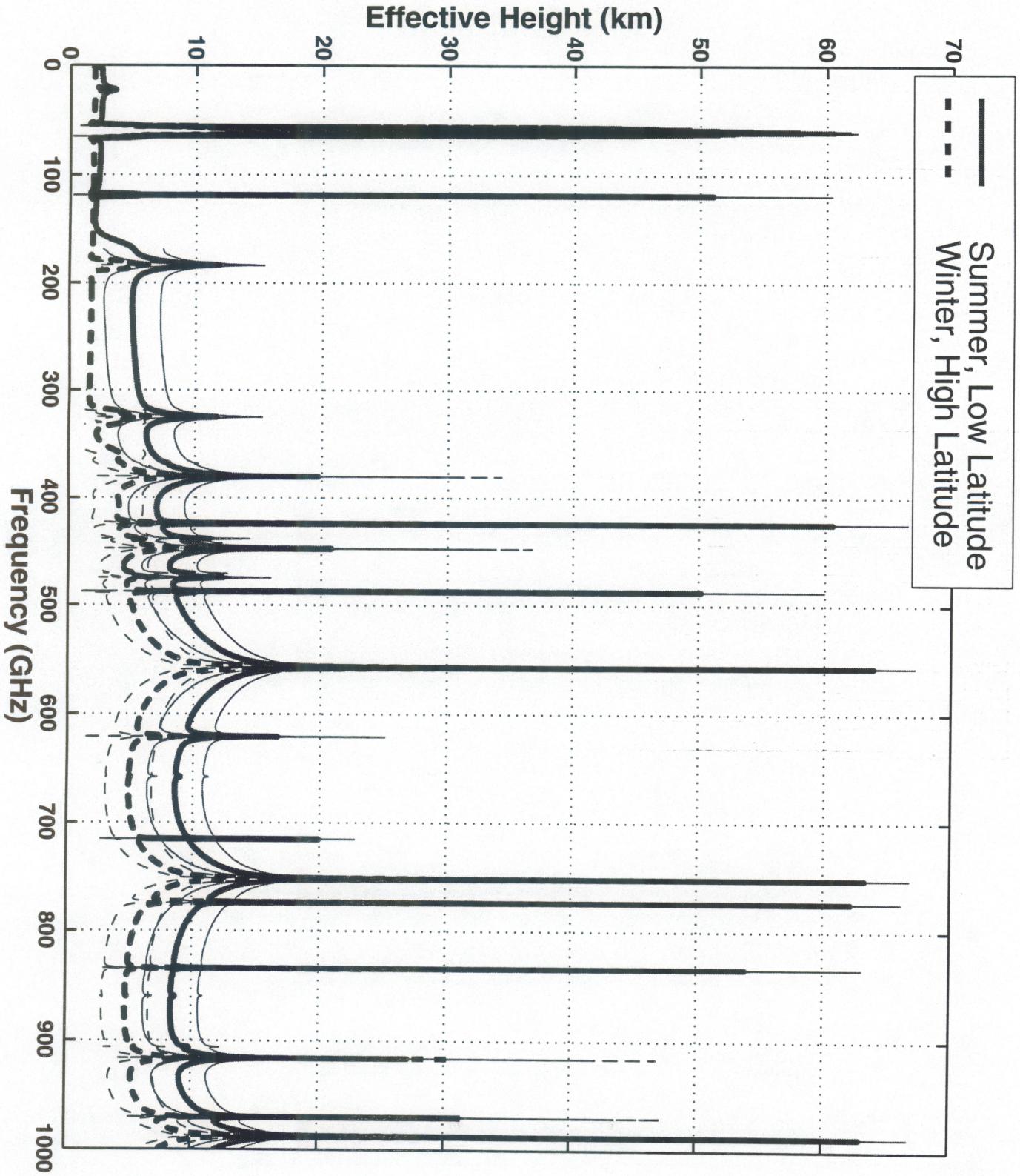

Figure 8: Effective water vapor sensing height $h_{eff,\rho}$ along with $h_{eff,\rho} \pm \sigma_{h,\rho}$ for two extreme atmospheric profiles, satellite nadir view over ocean background.

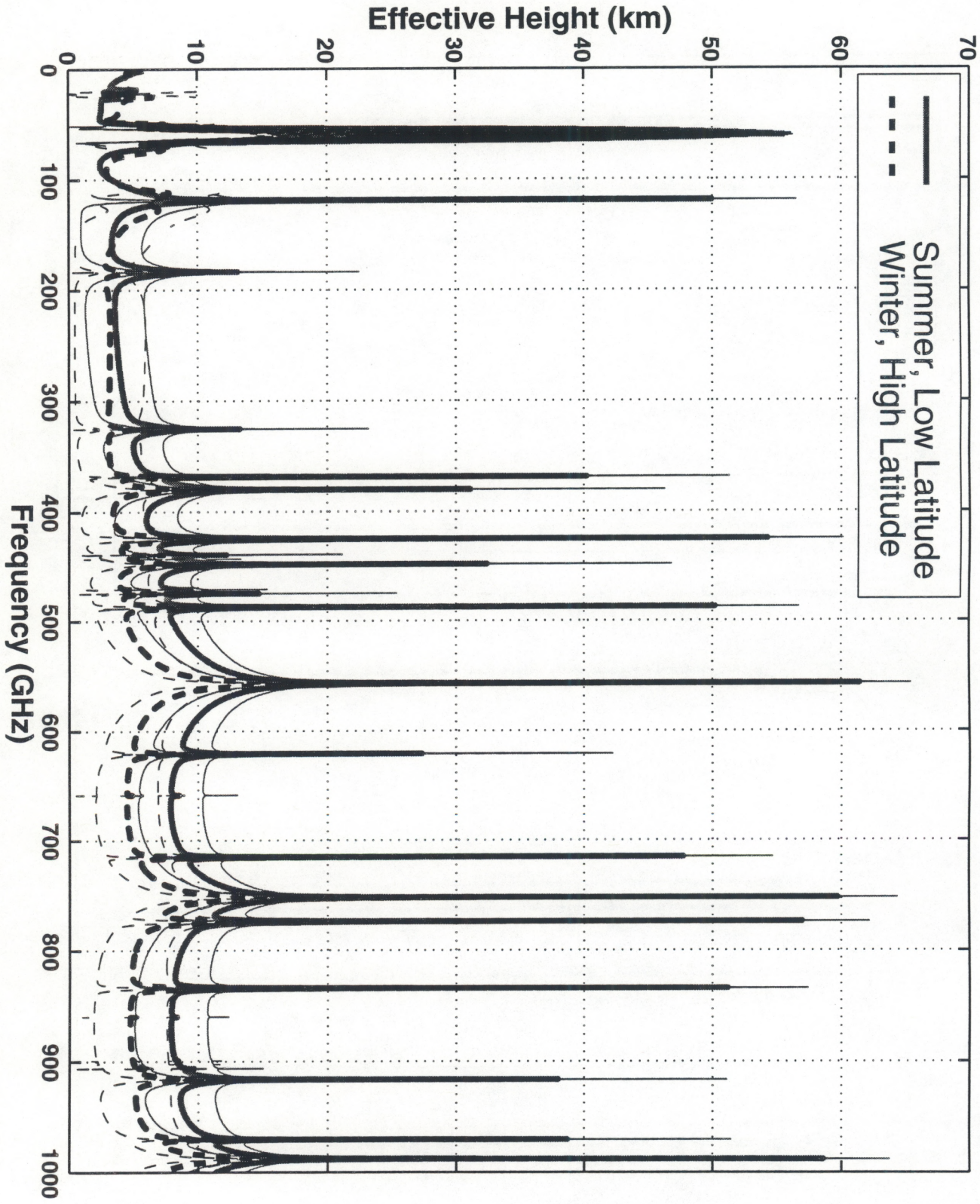

Figure 9: Effective temperature sensing height $h_{eff,T}$ along with $h_{eff,T} \pm \sigma_{h,T}$ for two extreme atmospheric profiles, satellite nadir view over ocean background.

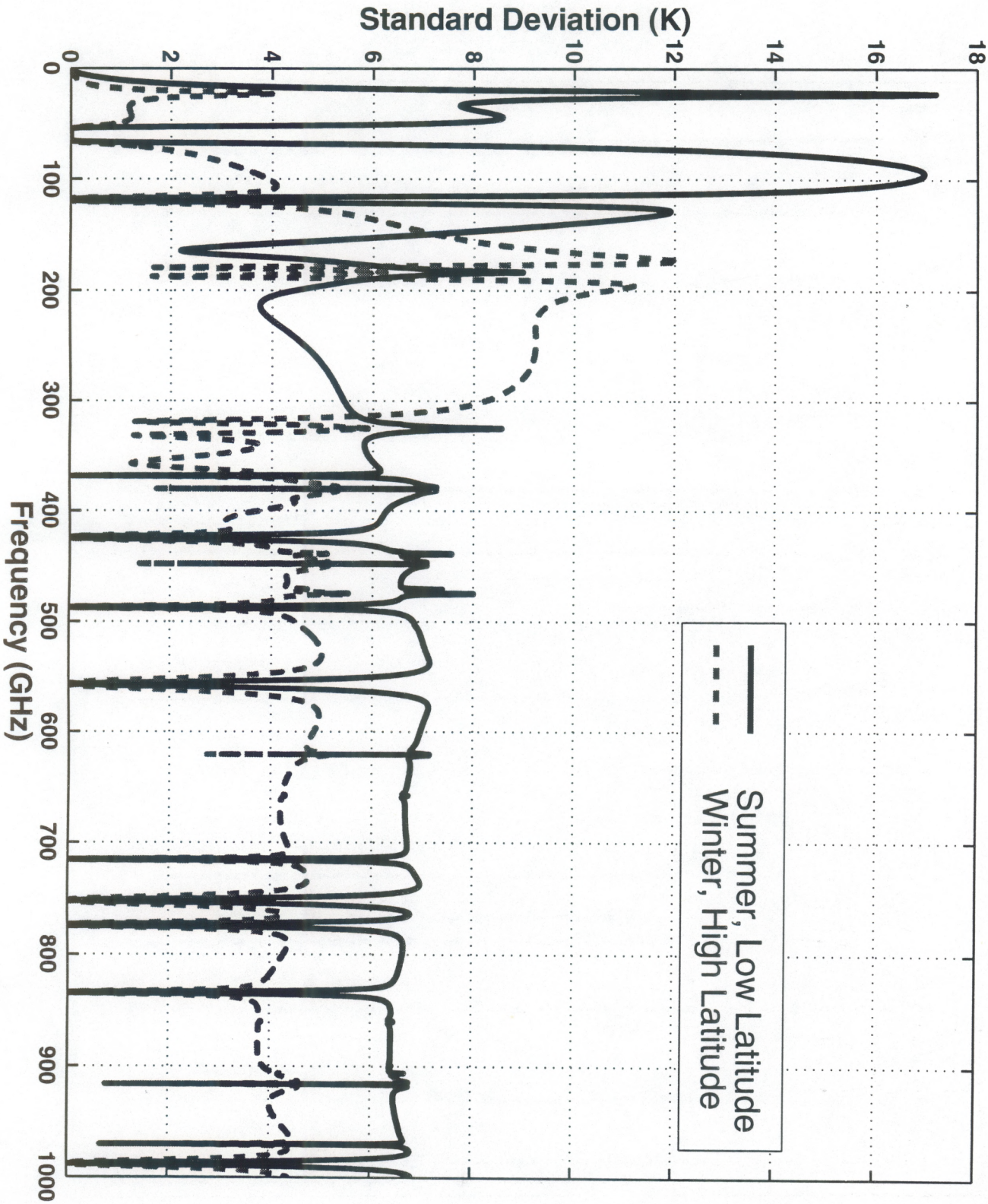

Figure 10: Standard deviation $\sigma_{TB,\rho}$ of upwelling brightness temperature due to the water vapor variations for two extreme atmospheric profiles, nadir view over ocean background.

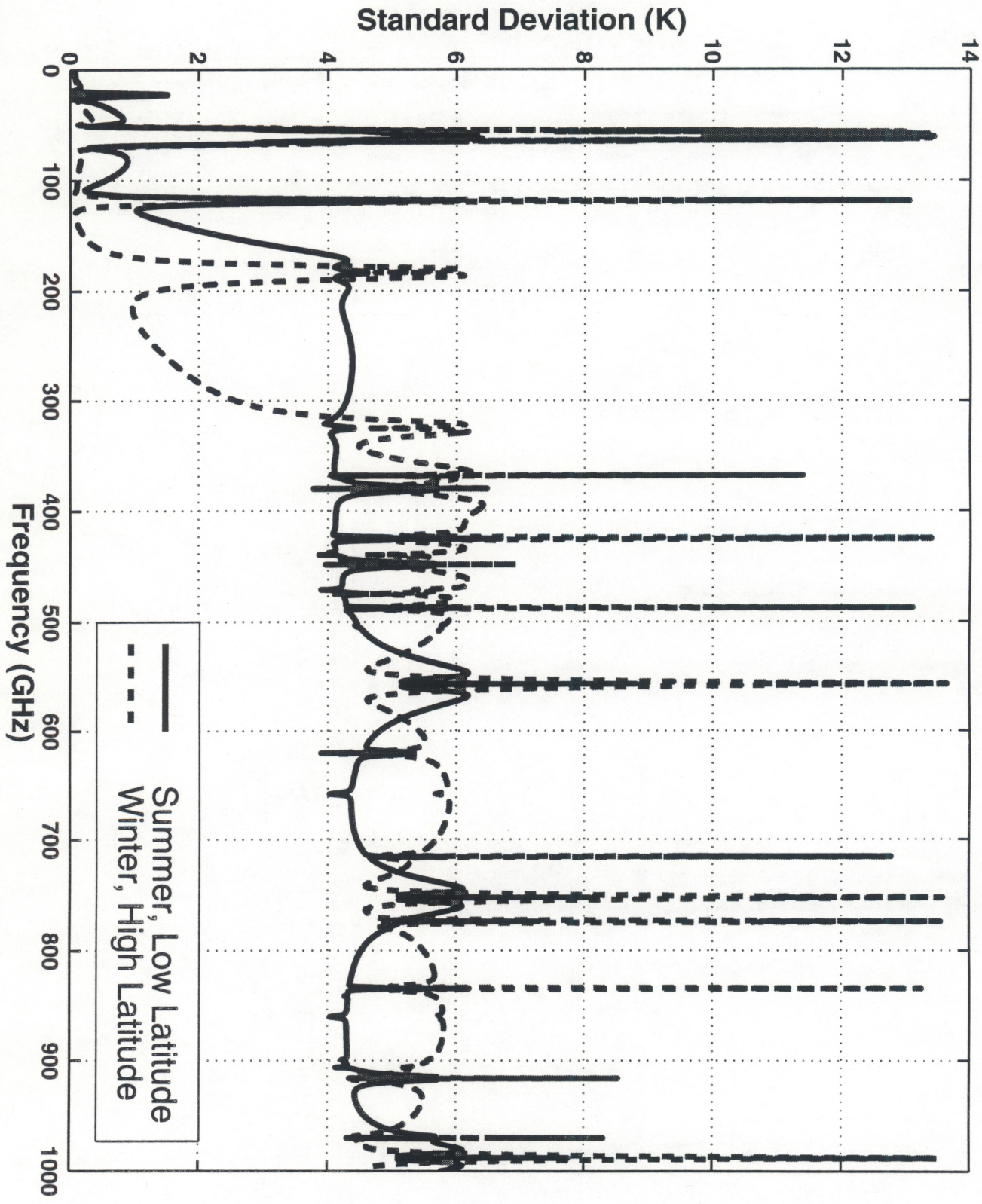

Figure 11: Standard deviation $\sigma_{TB,T}$ of upwelling brightness temperature due to the temperature variations for two extreme atmospheric profiles, nadir view over ocean background.

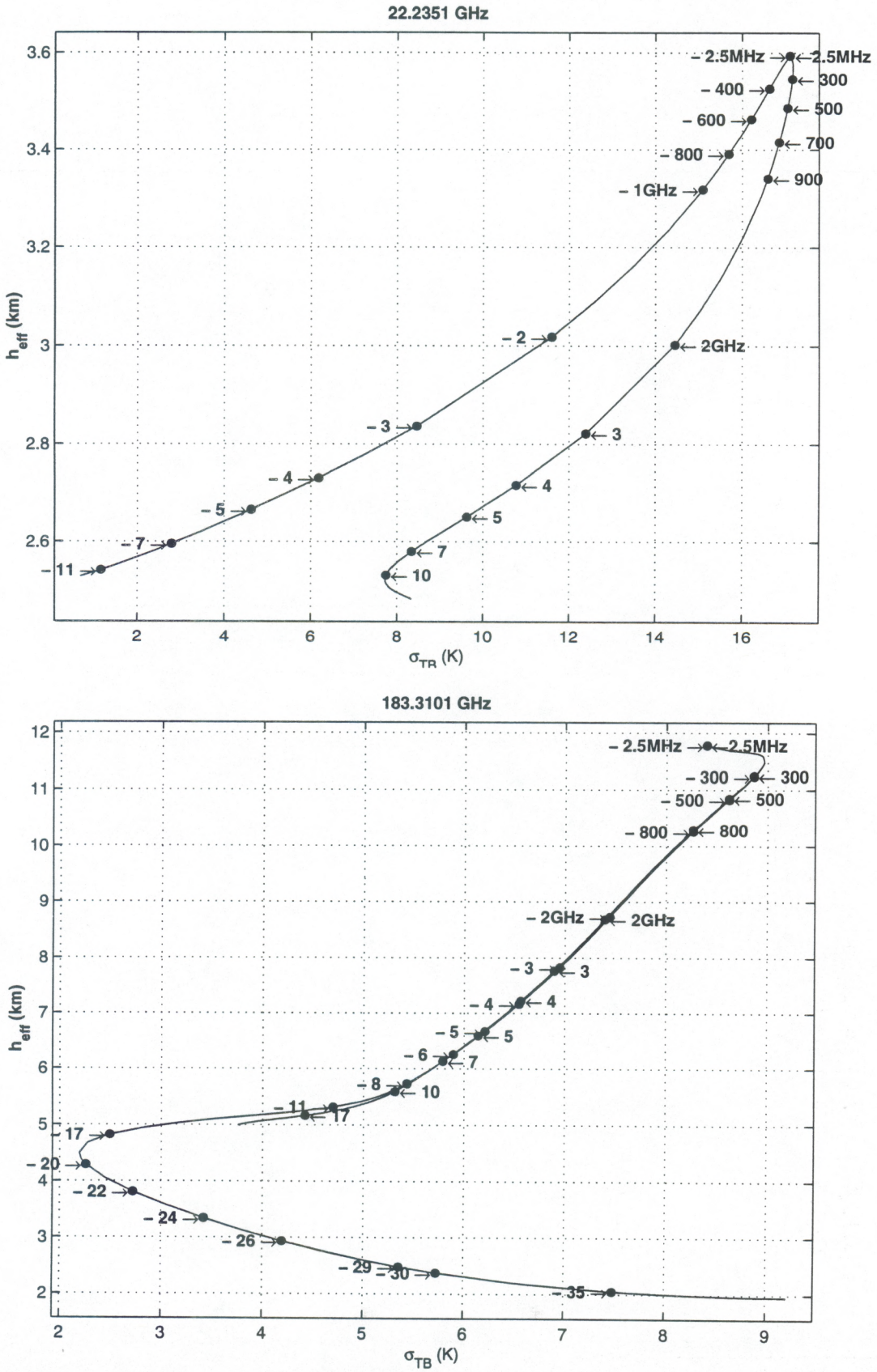

Figure 12a: RMS signal versus sounding height for 22.2351 and 183.3101 GHz water vapor lines for summer and low latitude conditions, satellite nadir view over ocean background. The arrows and numbers indicate frequency offsets from the respective absorption line center.

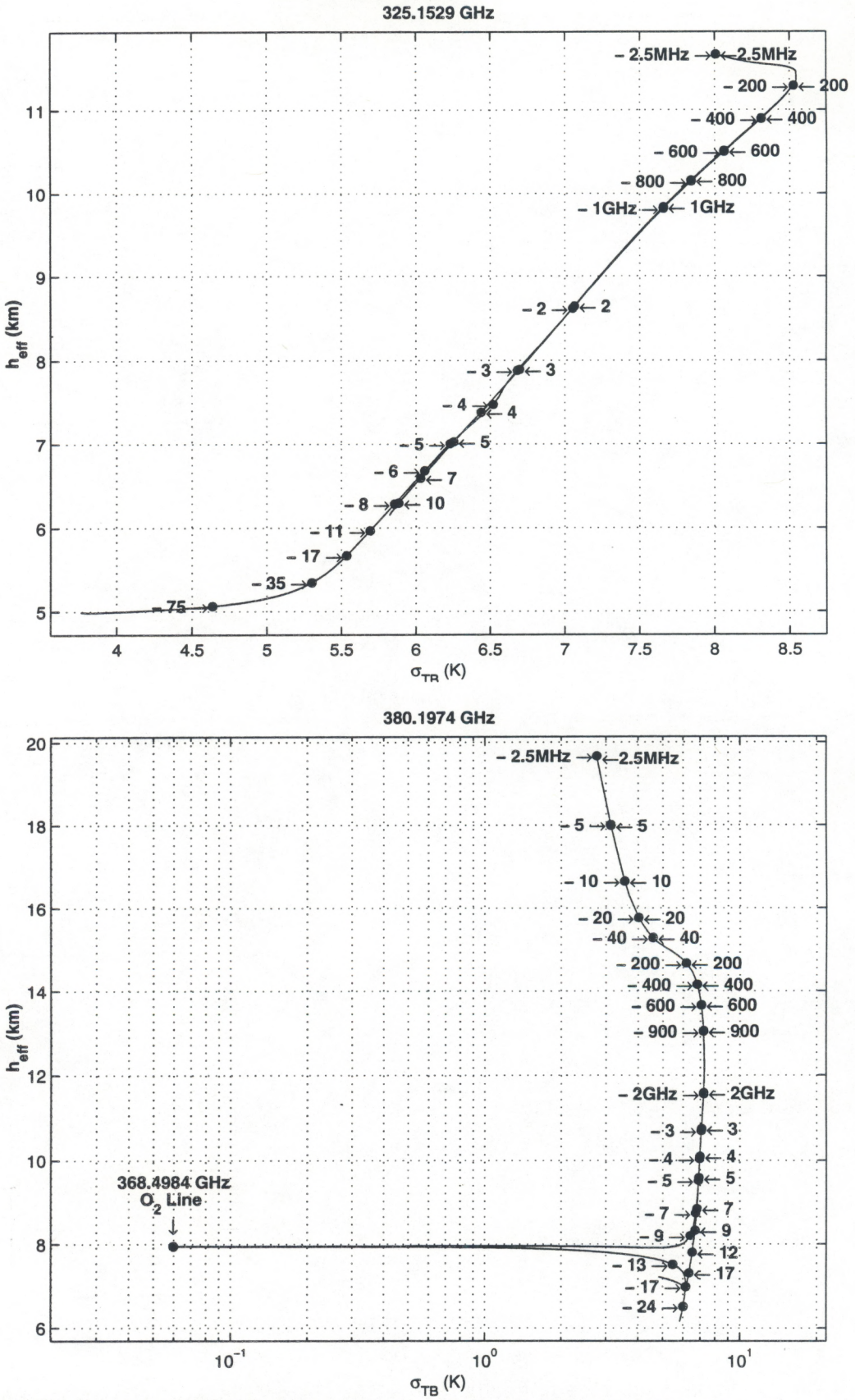

Figure 12b: RMS signal versus sounding height for 325.1529 and 380.1974 GHz water vapor lines for summer and low latitude conditions, satellite nadir view over ocean background. The arrows and numbers indicate frequency offsets from the respective absorption line center.

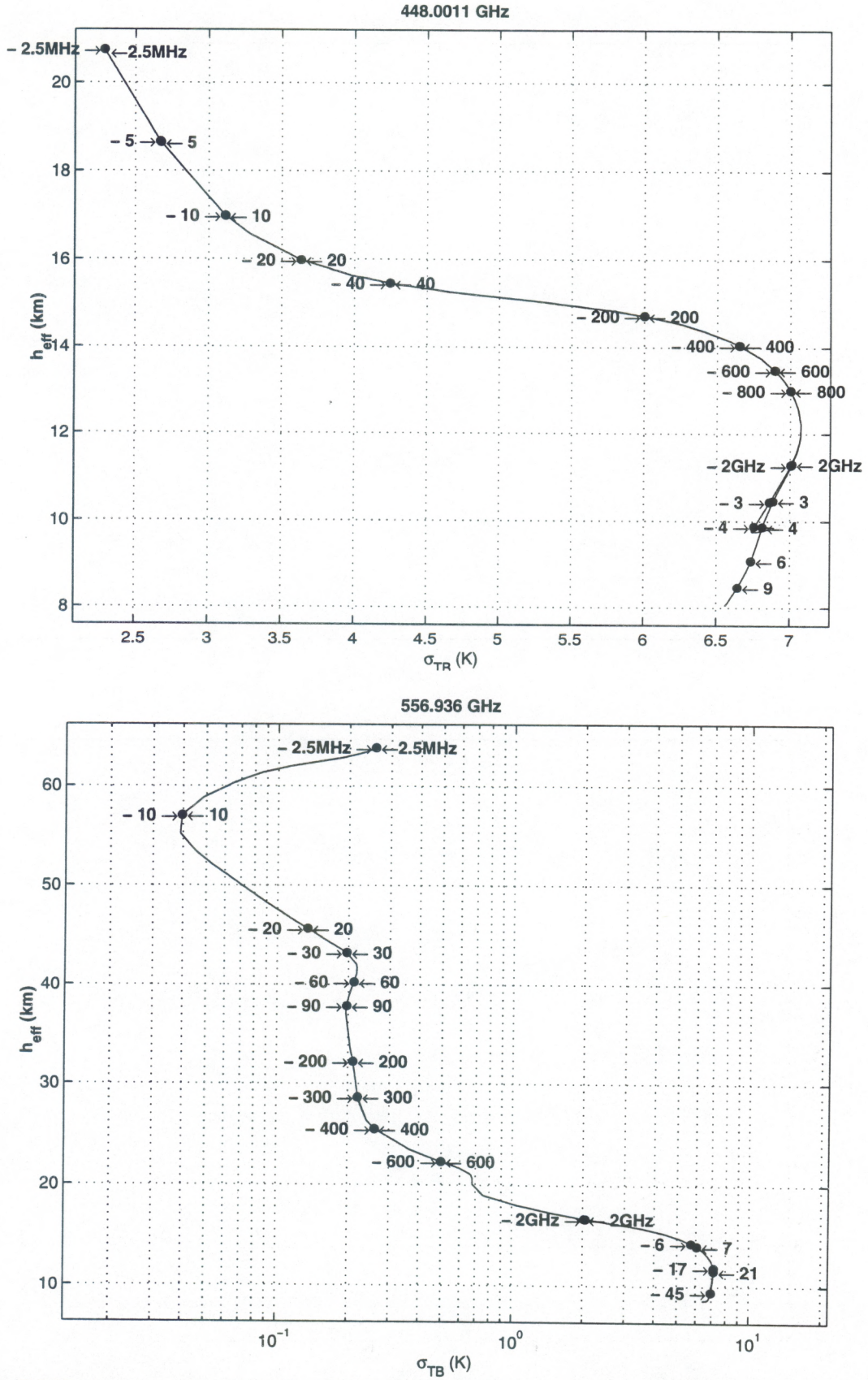

Figure 12c: RMS signal versus sounding height for 448.0011 and 556.9360 GHz water vapor lines for summer and low latitude conditions, satellite nadir view over ocean background. The arrows and numbers indicate frequency offsets from the respective absorption line center.

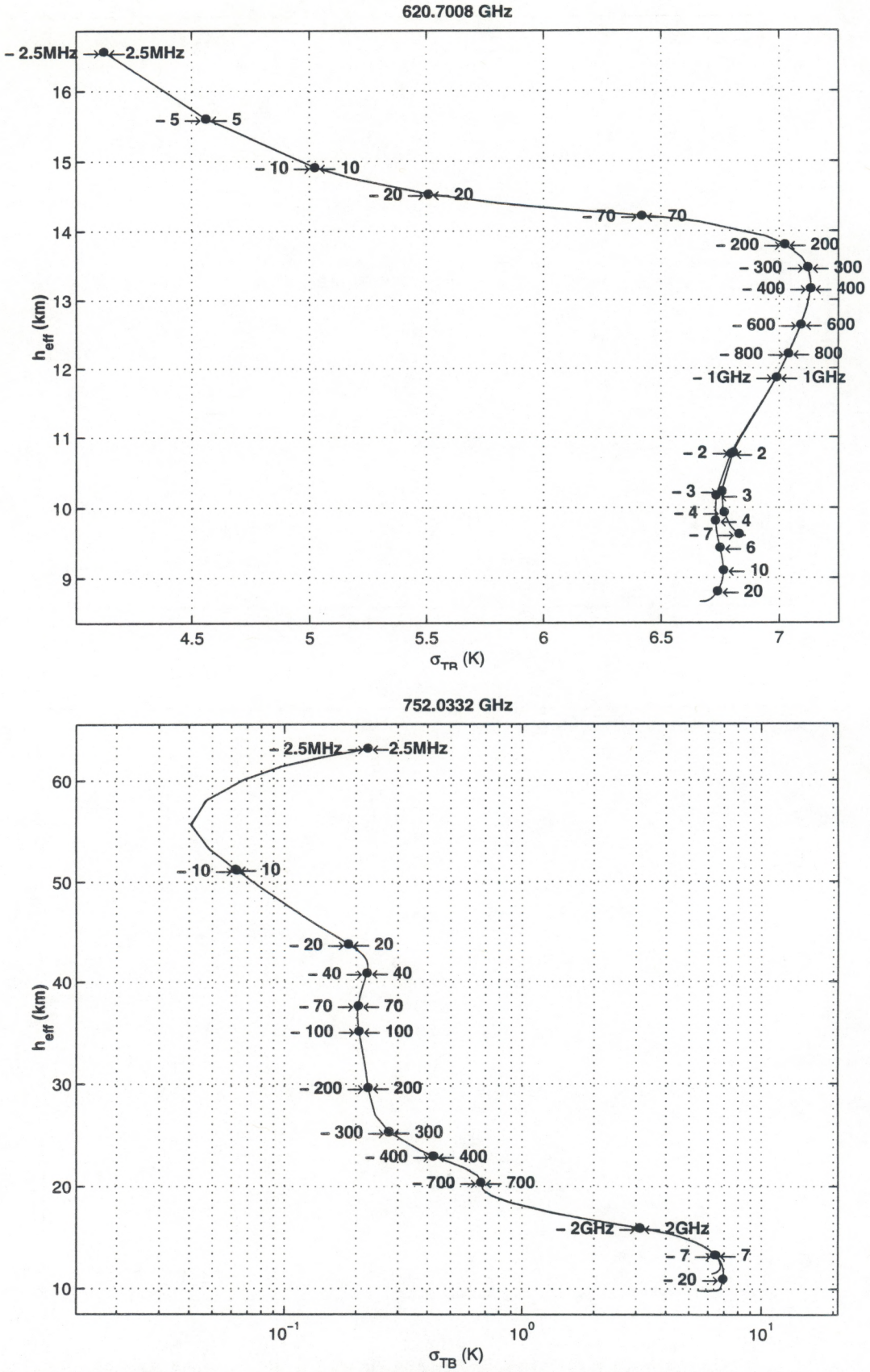

Figure 12d: RMS signal versus sounding height for 620.7008 and 752.0332 GHz water vapor lines for summer and low latitude conditions, satellite nadir view over ocean background. The arrows and numbers indicate frequency offsets from the respective absorption line center.

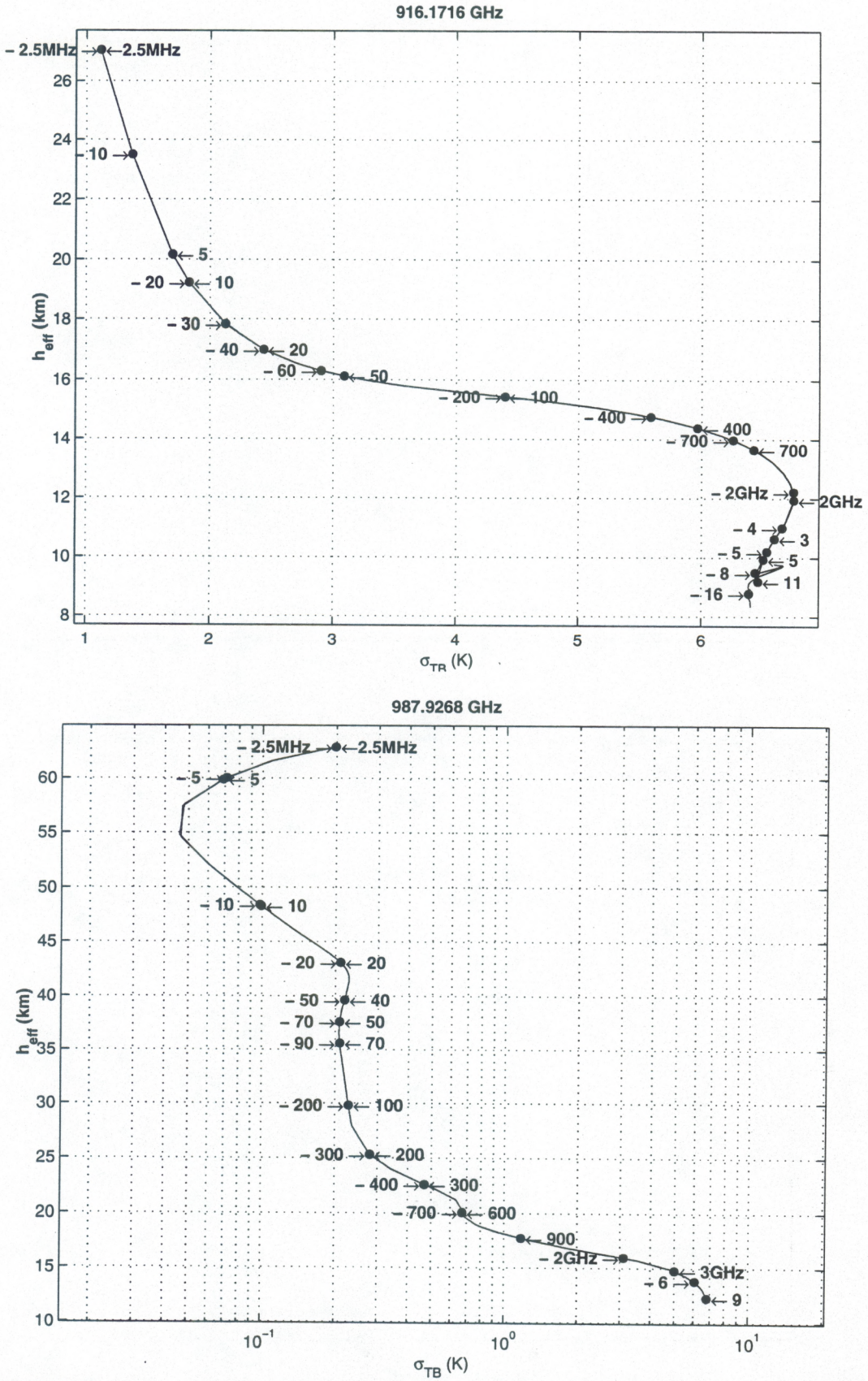

Figure 12e: RMS signal versus sounding height for 916.1716 and 987.9268 GHz water vapor lines for summer and low latitude conditions, satellite nadir view over ocean background. The arrows and numbers indicate frequency offsets from the respective absorption line center.

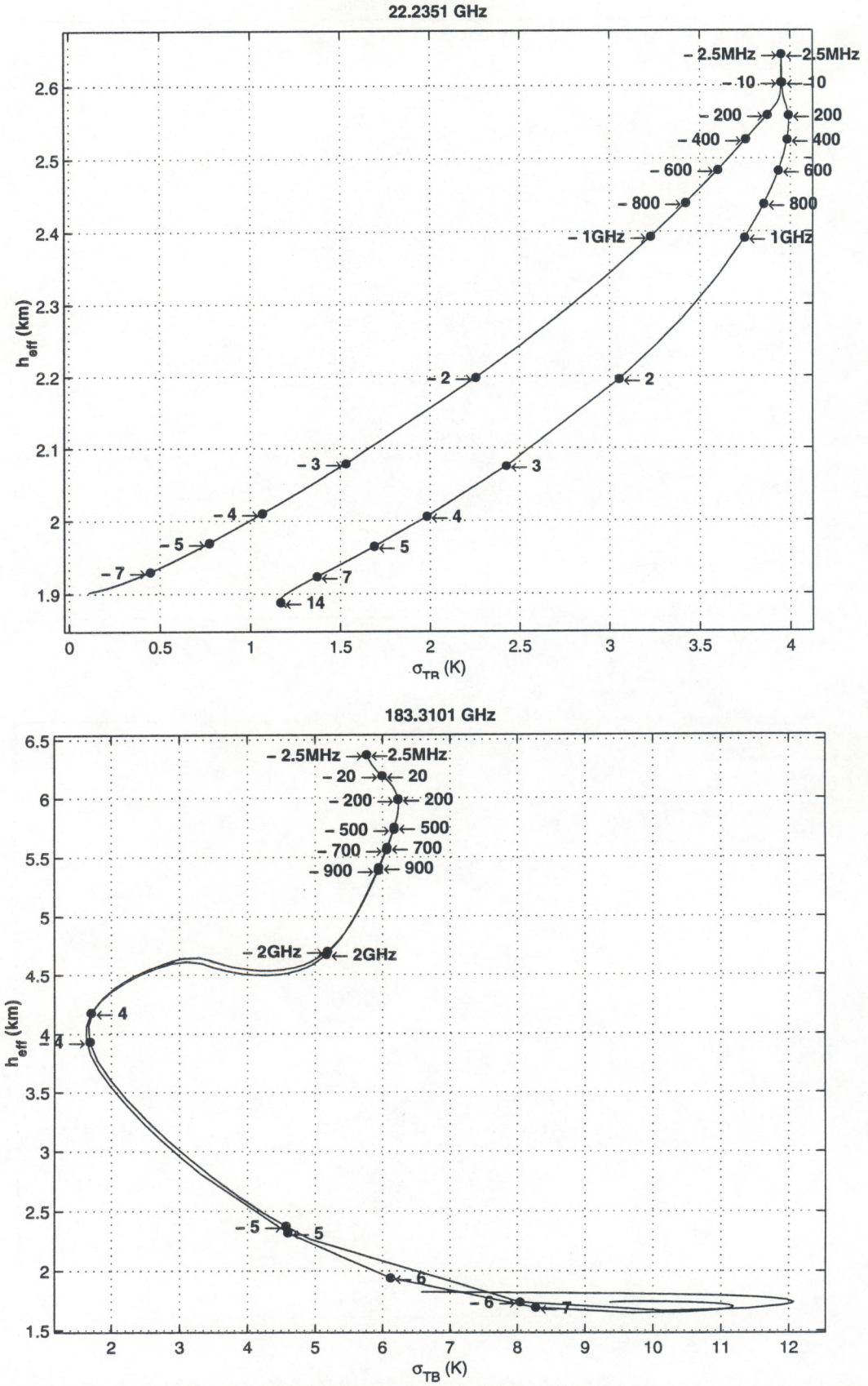

Figure 13a: RMS signal versus sounding height for 22.2351 and 183.3101 GHz water vapor lines for winter and high latitude conditions, satellite nadir view over ocean background. The arrows and numbers indicate frequency offsets from the respective absorption line center.

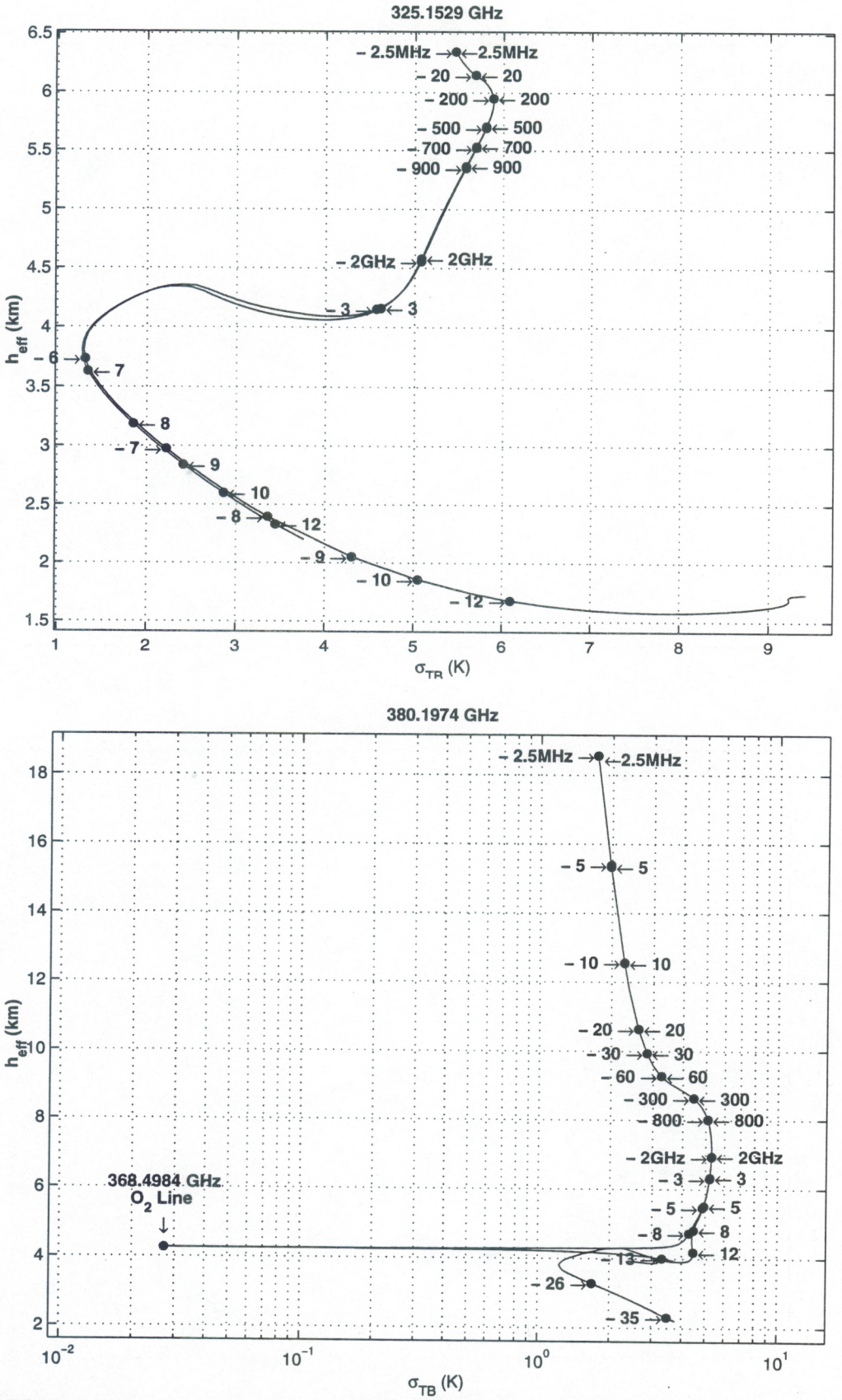

Figure 13b: RMS signal versus sounding height for 325.1529 and 380.1974 GHz water vapor lines for winter and high latitude conditions, satellite nadir view over ocean background. The arrows and numbers indicate frequency offsets from the respective absorption line center.

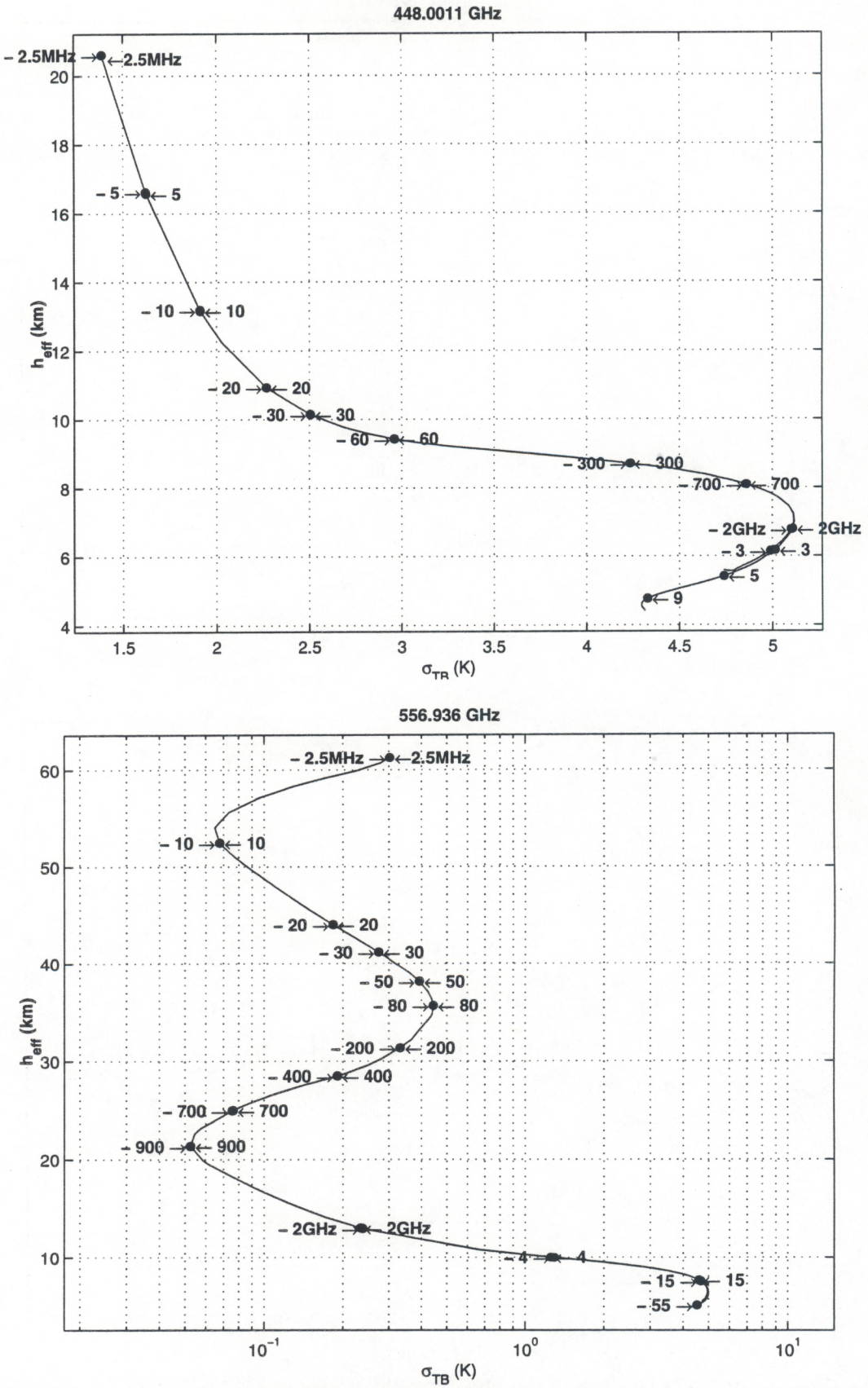

Figure 13c: RMS signal versus sounding height for 448.0011 and 556.9360 GHz water vapor lines for winter and high latitude conditions, satellite nadir view over ocean background. The arrows and numbers indicate frequency offsets from the respective absorption line center.

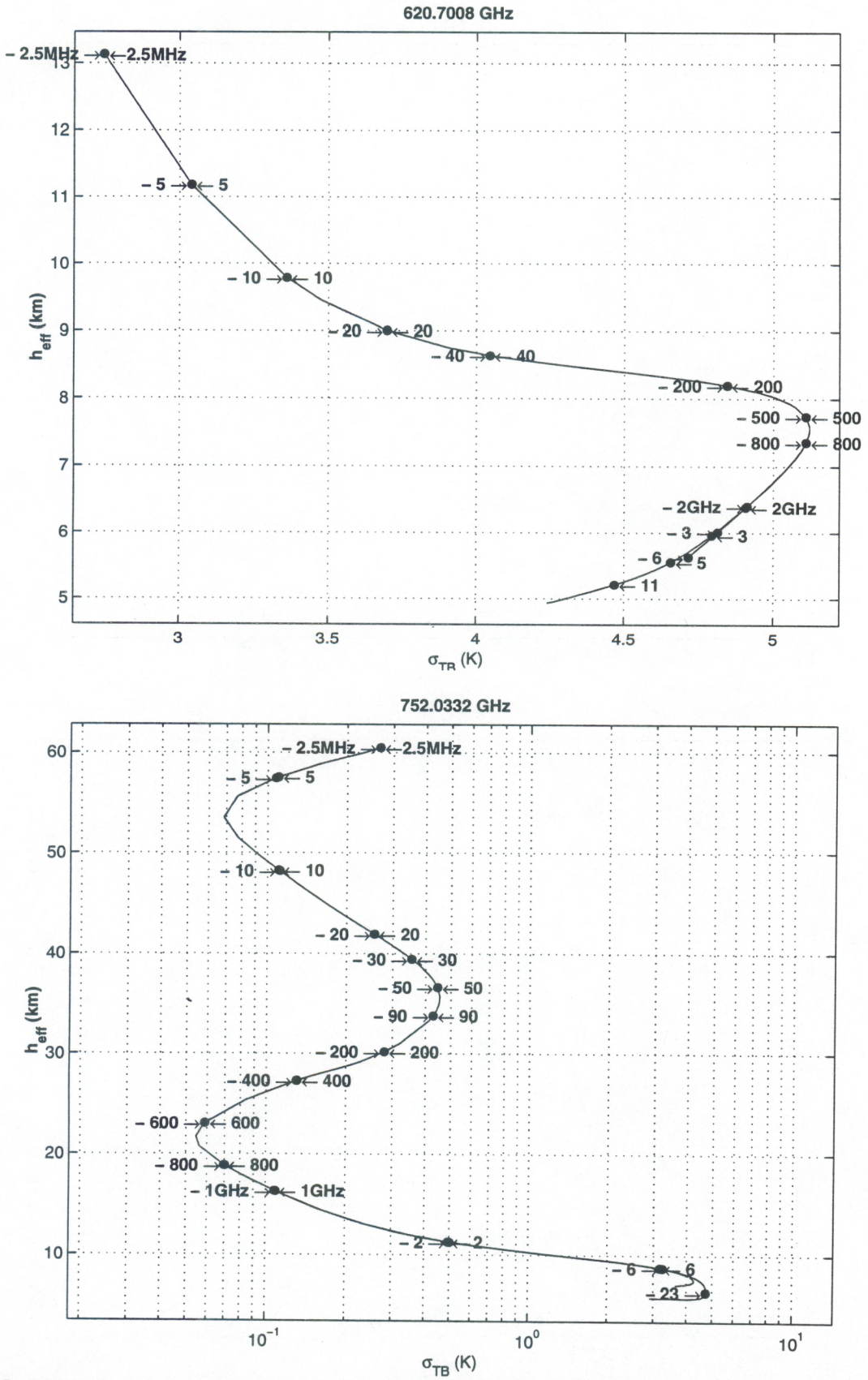

Figure 13d: RMS signal versus sounding height for 620.7008 and 752.0332 GHz water vapor lines for winter and high latitude conditions, satellite nadir view over ocean background. The arrows and numbers indicate frequency offsets from the respective absorption line center.

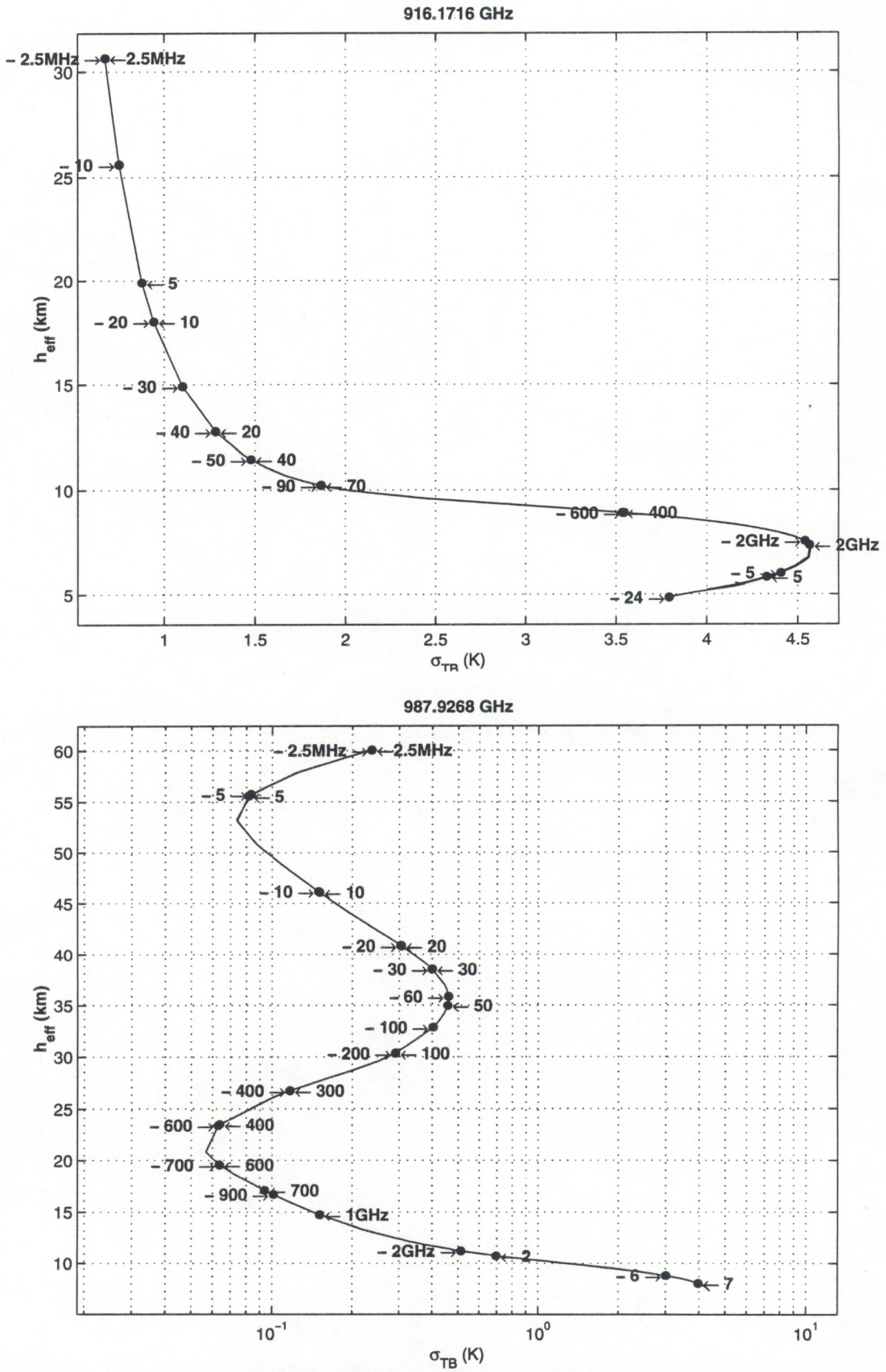

Figure 13e: RMS signal versus sounding height for 916.1716 and 987.9268 GHz water vapor lines for winter and high latitude conditions, satellite nadir view over ocean background. The arrows and numbers indicate frequency offsets from the respective absorption line center.

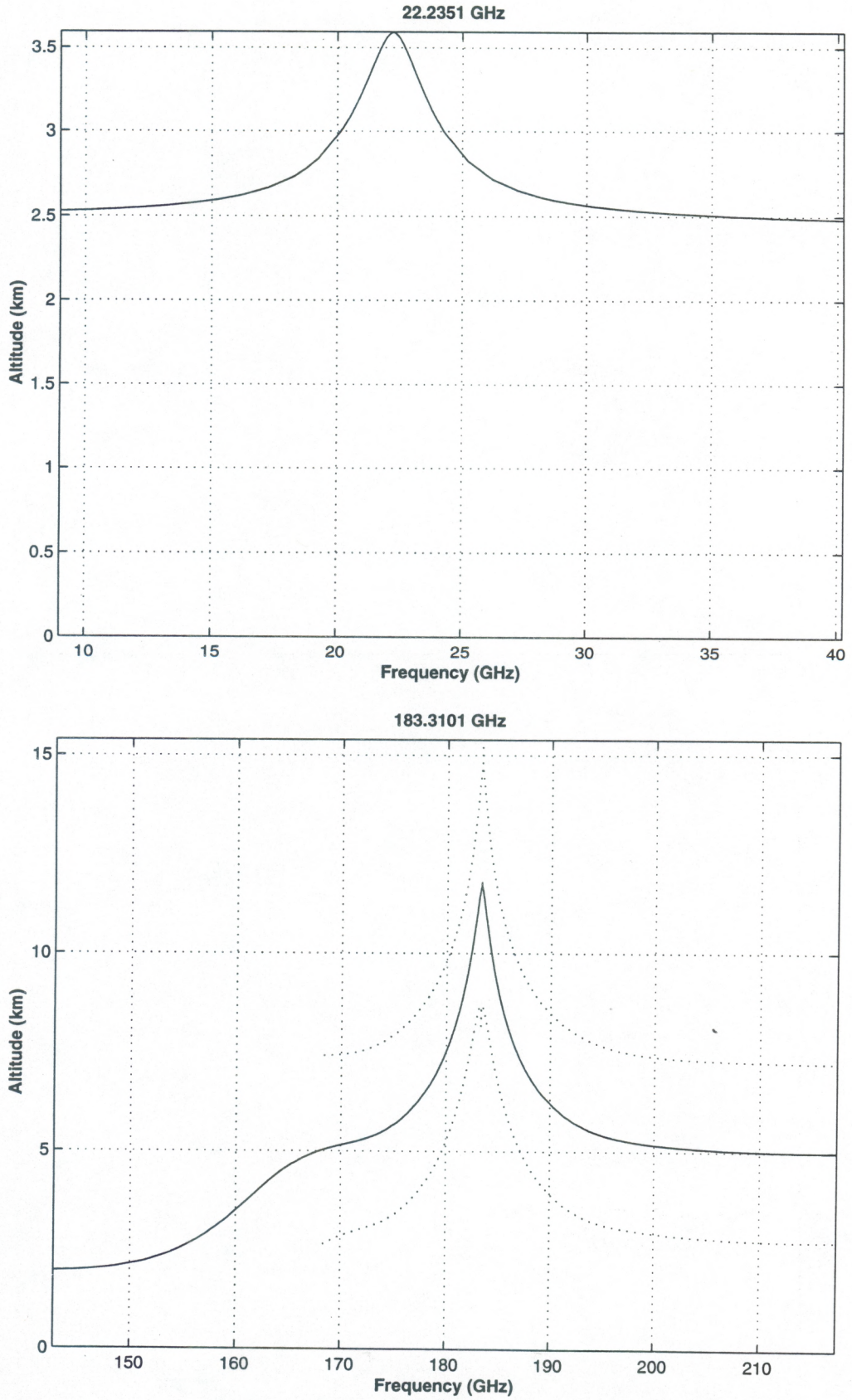

Figure 14a: Effective water vapor sounding height h_{eff} along with $h_{eff} \pm \sigma_h$ for 22.2351 and 183.3101 GHz water vapor lines for summer and low latitude conditions, satellite nadir view over ocean background.

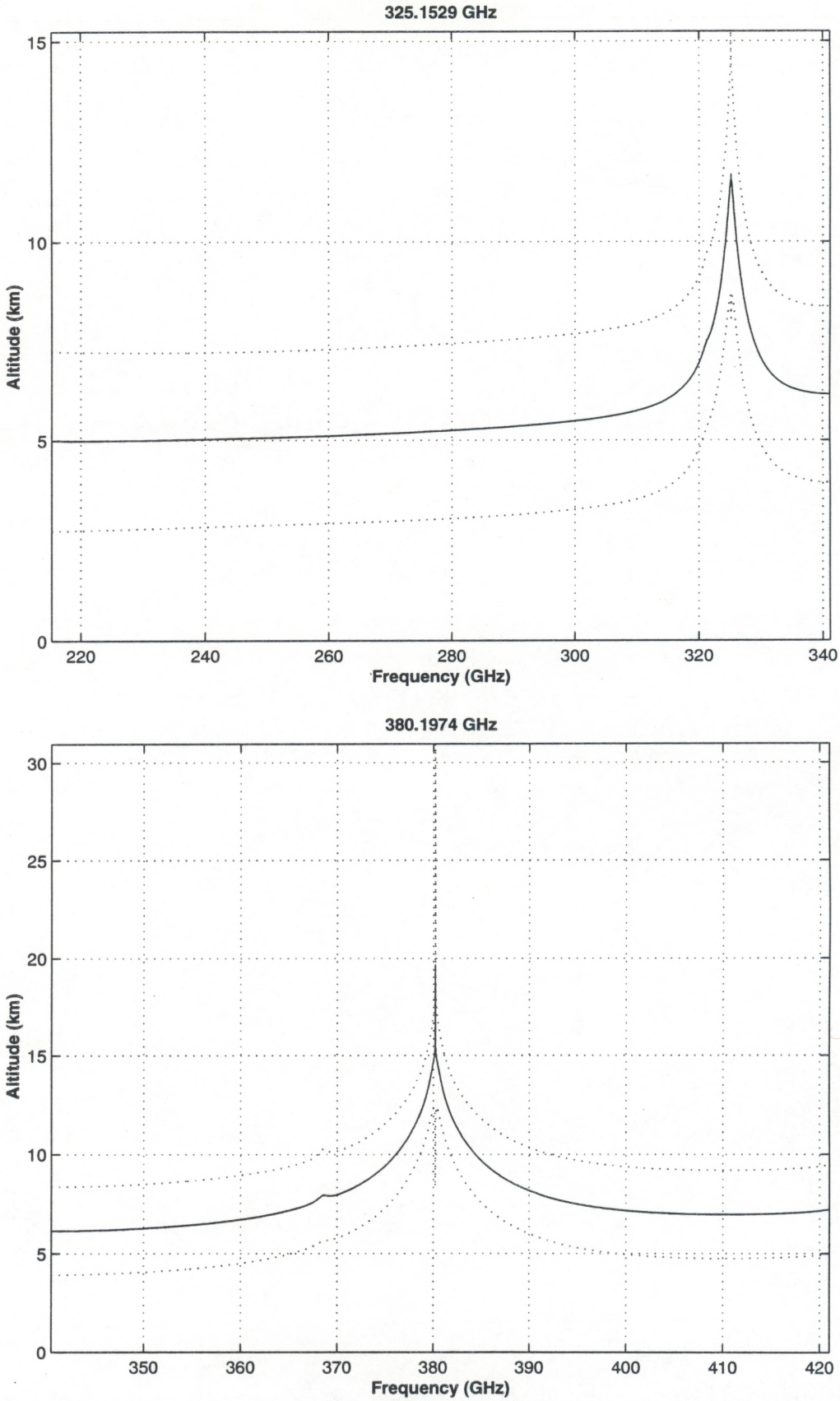

Figure 14b: Effective water vapor sounding height h_{eff} along with $h_{eff} \pm \sigma_h$ for 22.2351 and 183.3101 GHz water vapor lines for summer and low latitude conditions, satellite nadir view over ocean background.

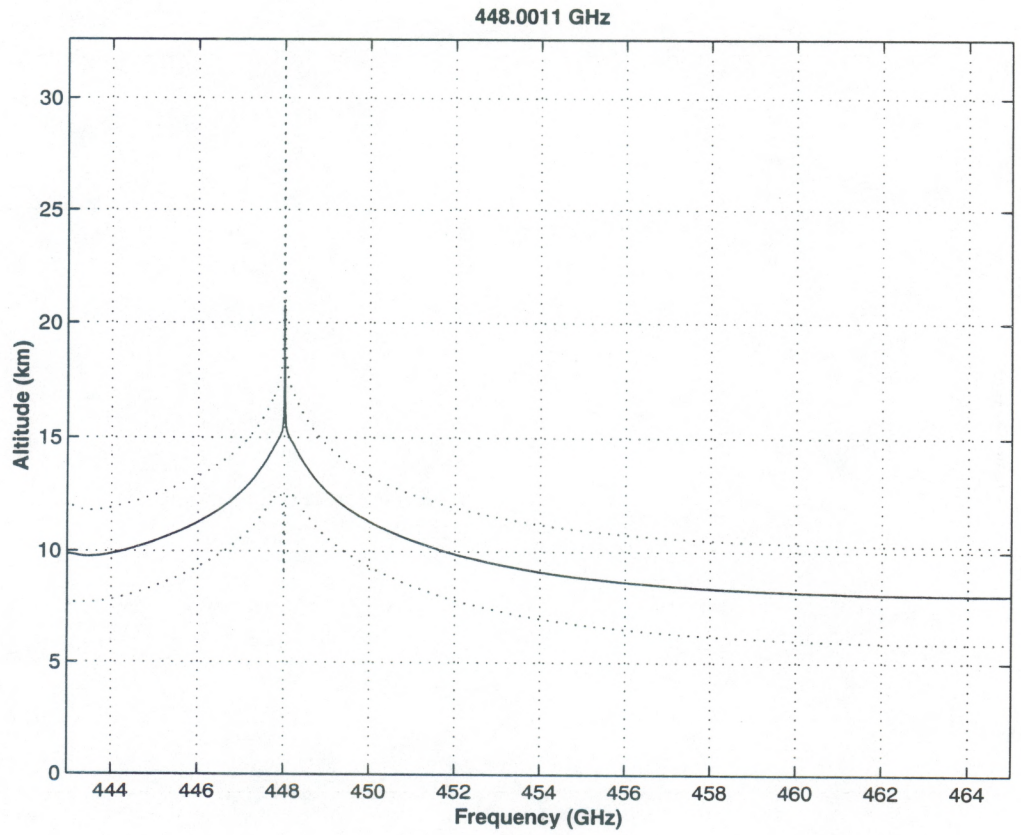

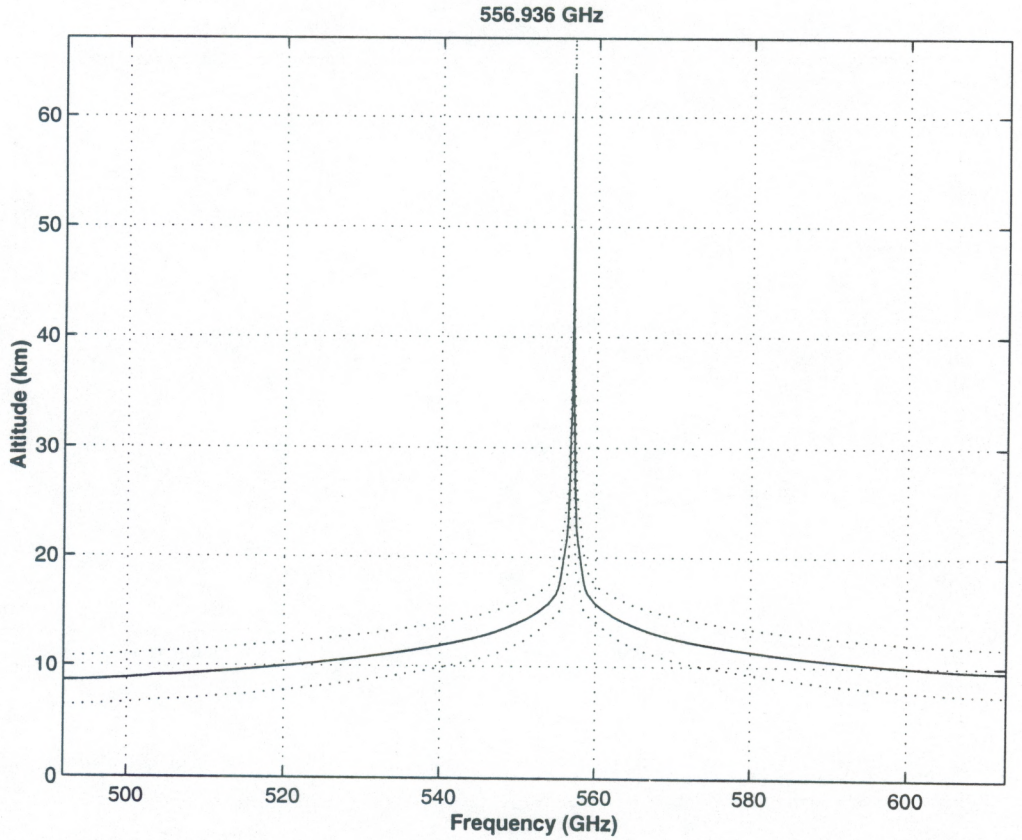

Figure 14c: Effective water vapor sounding height h_{eff} along with $h_{eff} \pm \sigma_h$ for 448.0011 and 556.9360 GHz water vapor lines for summer and low latitude conditions, satellite nadir view over ocean background.

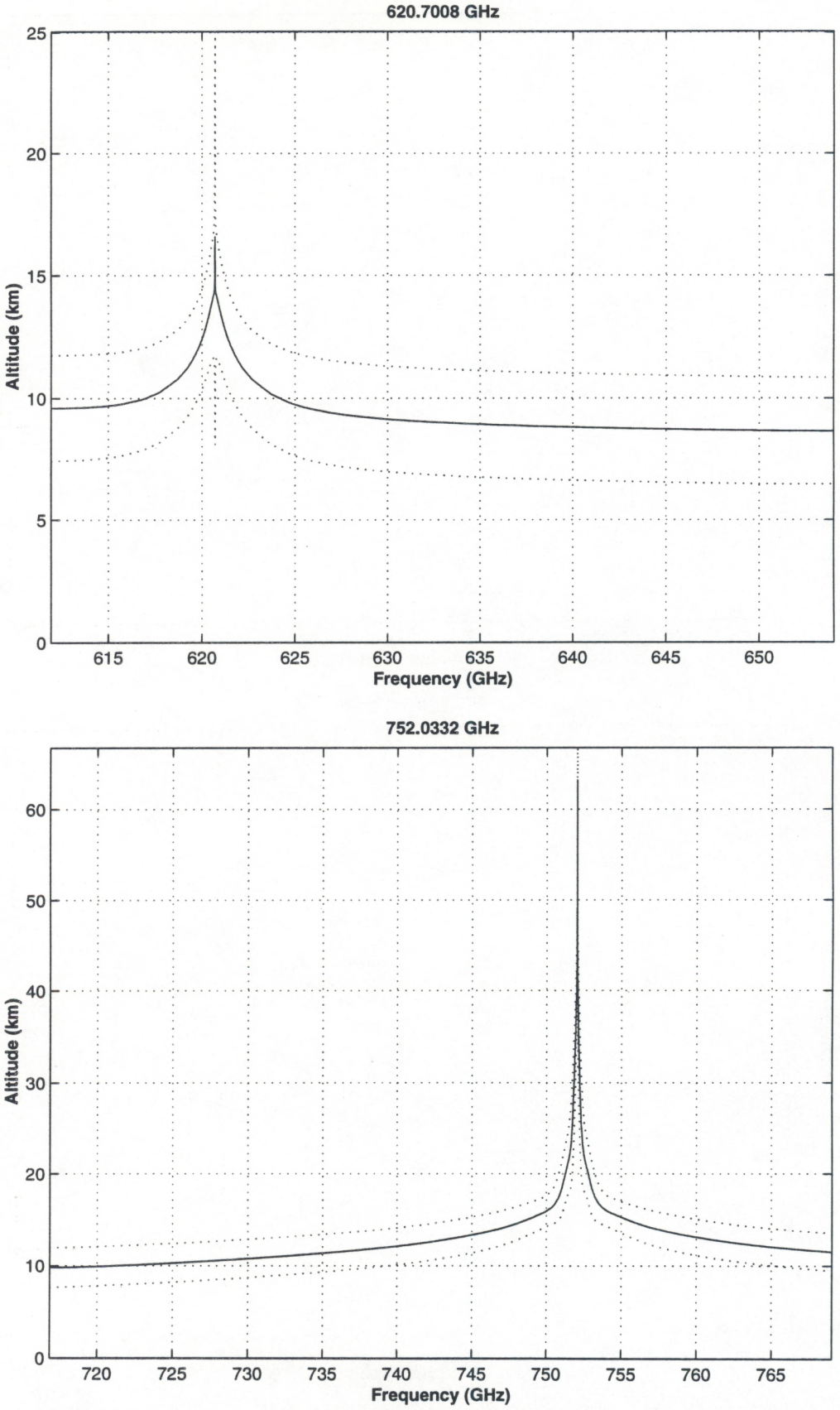

Figure 14d: Effective water vapor sounding height h_{eff} along with $h_{eff} \pm \sigma_h$ for 620.7008 and 752.0332 GHz water vapor lines for summer and low latitude conditions, satellite nadir view over ocean background.

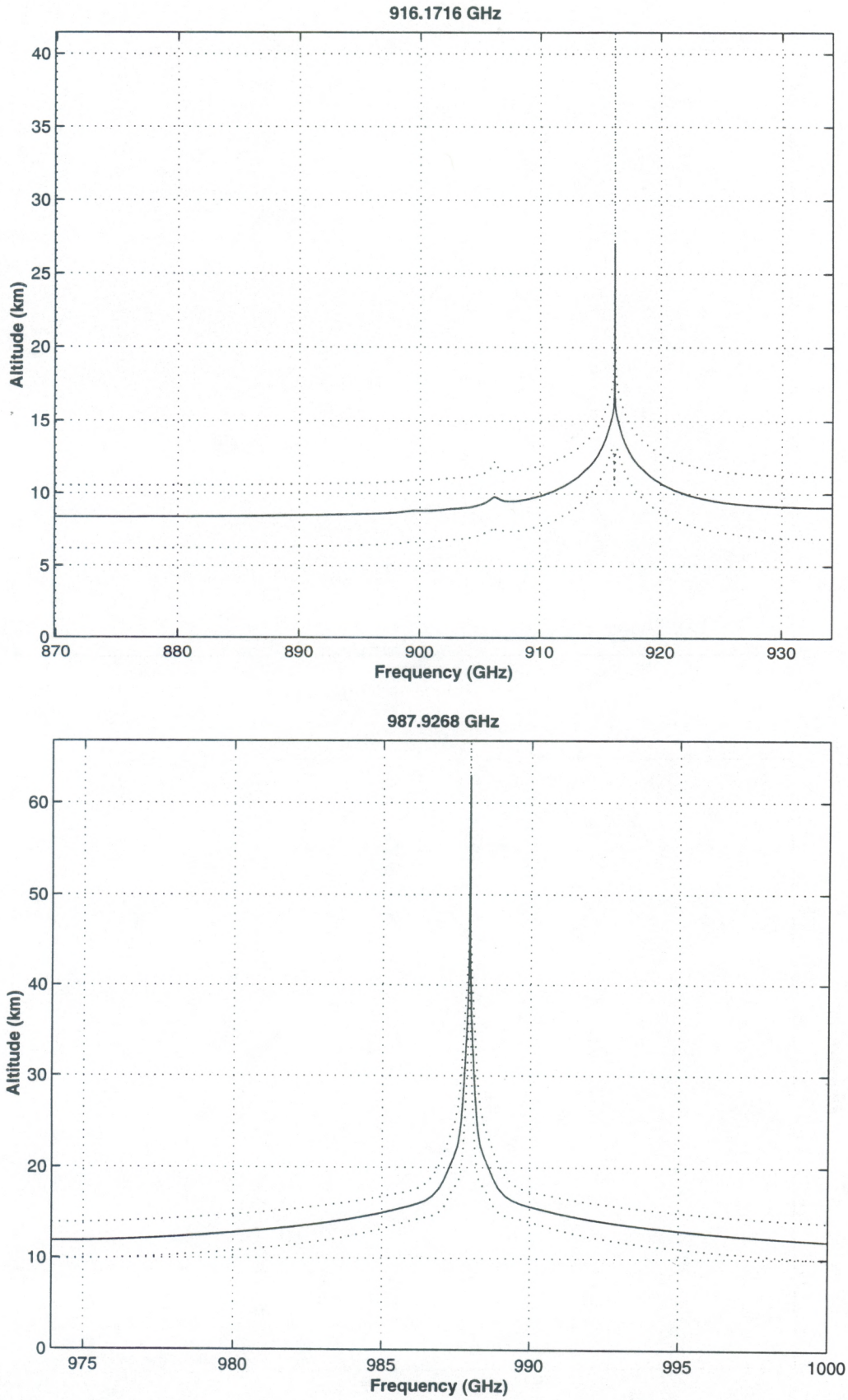

Figure 14e: Effective water vapor sounding height h_{eff} along with $h_{eff} \pm \sigma_h$ for 916.1716 and 987.9268 GHz water vapor lines for summer and low latitude conditions, satellite nadir view over ocean background.

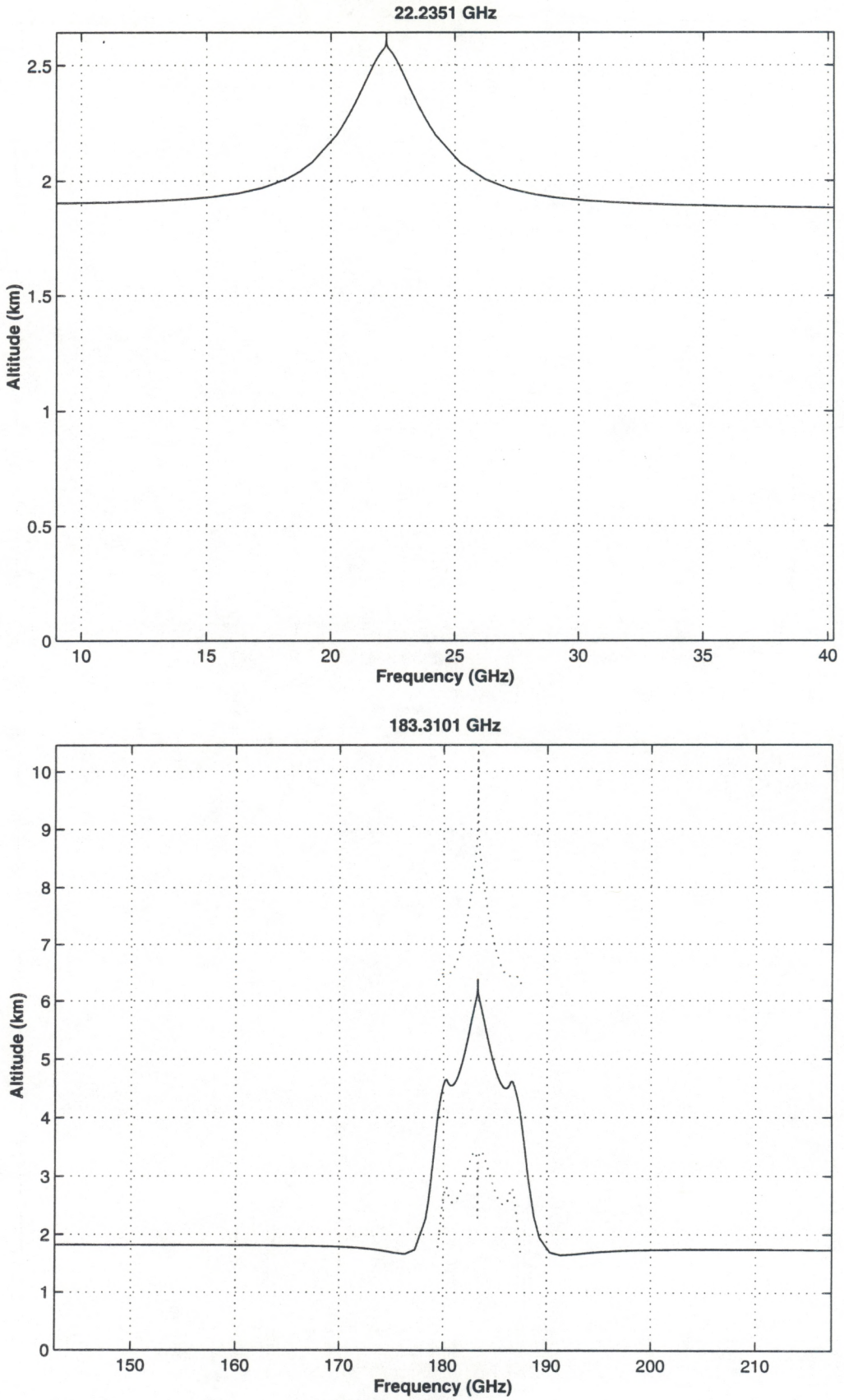

Figure 15a: Effective water vapor sounding height h_{eff} along with $h_{eff} \pm \sigma_h$ for 22.2351 and 183.3101 GHz water vapor lines for winter and high latitude conditions, satellite nadir view over ocean background.

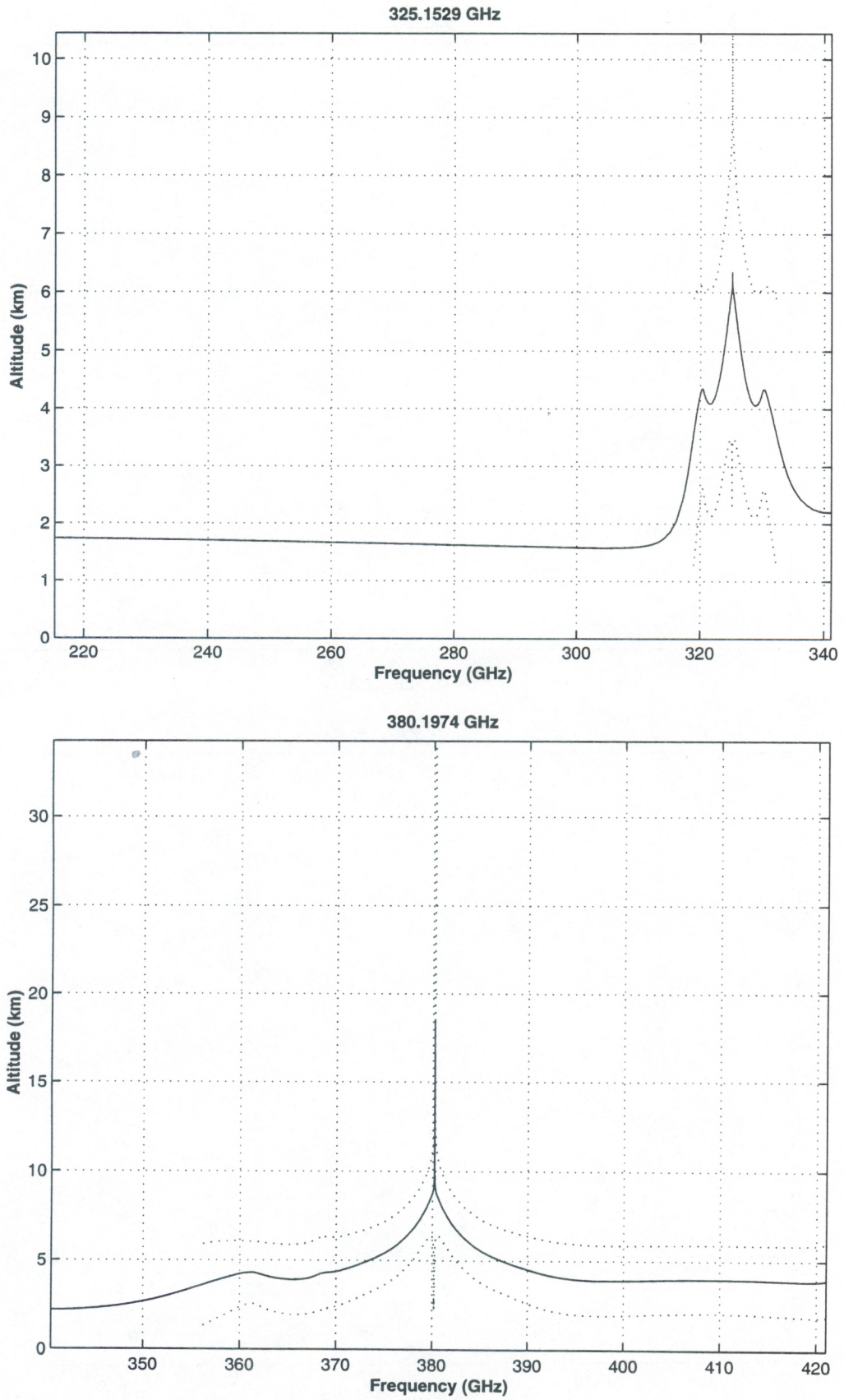

Figure 15b: Effective water vapor sounding height h_{eff} along with $h_{eff} \pm \sigma_h$ for 325.1529 and 380.1974 GHz water vapor lines for winter and high latitude conditions, satellite nadir view over ocean background.

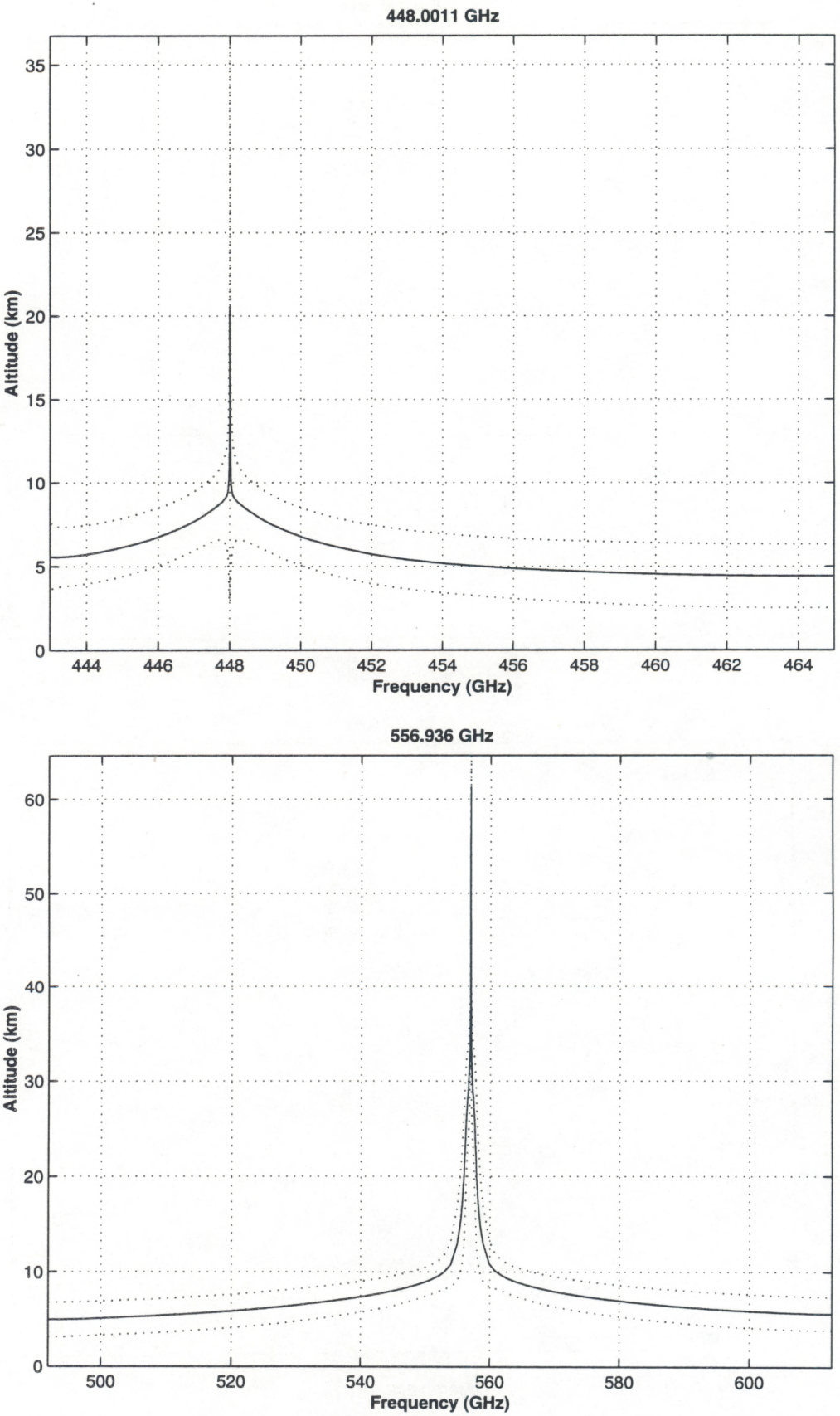

Figure 15c: Effective water vapor sounding height h_{eff} along with $h_{eff} \pm \sigma_h$ for 448.0011 and 556.9360 GHz water vapor lines for winter and high latitude conditions, satellite nadir view over ocean background.

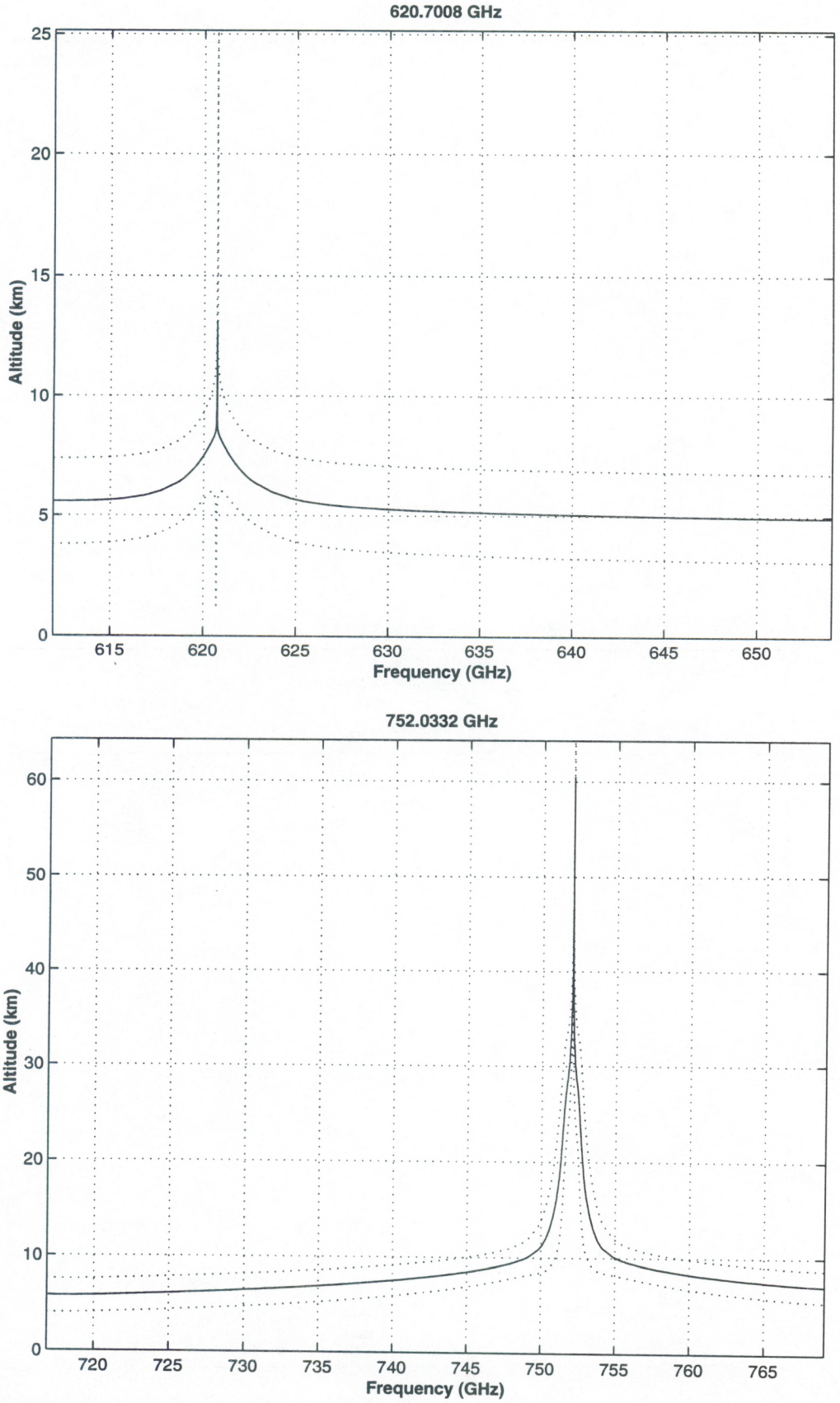

Figure 15d: Effective water vapor sounding height h_{eff} along with $h_{eff} \pm \sigma_h$ for 620.7008 and 752.0332 GHz water vapor lines for winter and high latitude conditions, satellite nadir view over ocean background.

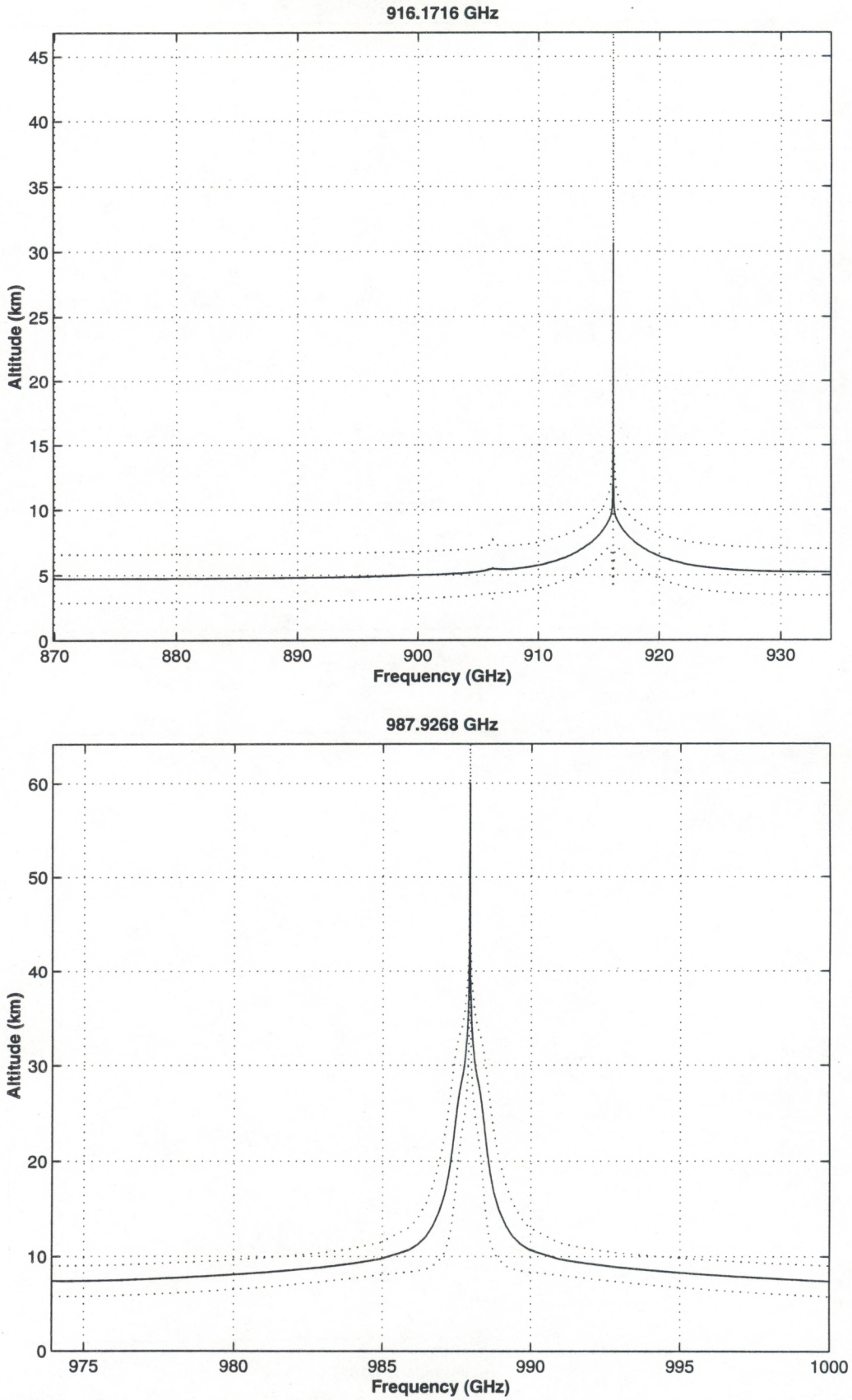

Figure 15e: Effective water vapor sounding height h_{eff} along with $h_{eff} \pm \sigma_h$ for 916.1716 and 987.9268 GHz water vapor lines for winter and high latitude conditions, satellite nadir view over ocean background.

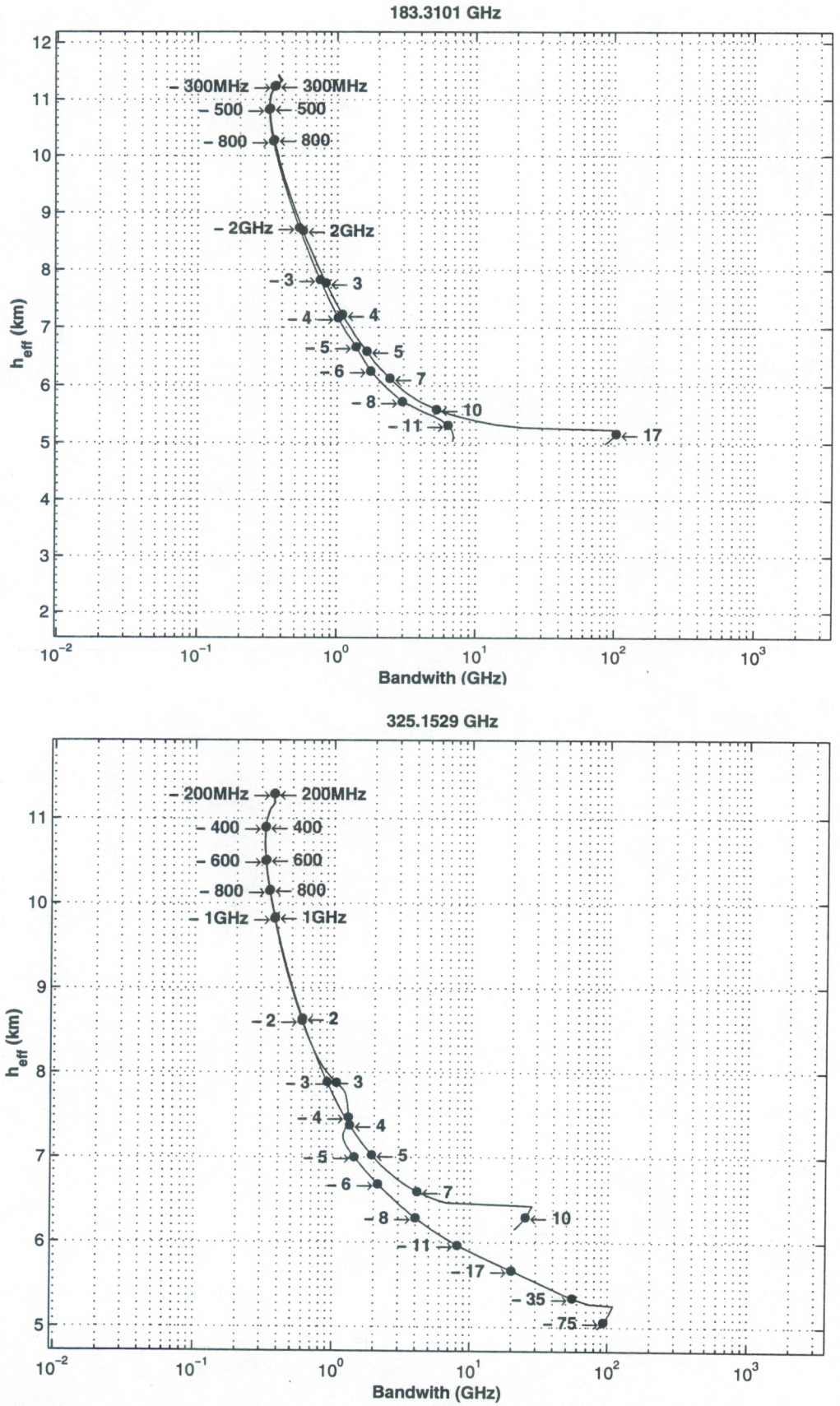

Figure 16a: Natural available bandwidth for water vapor sounding for 183.3101 and 325.1529 GHz water vapor lines for summer and low latitude conditions, satellite nadir view over ocean background. The arrows and numbers indicate frequency offsets from the respective absorption line center.

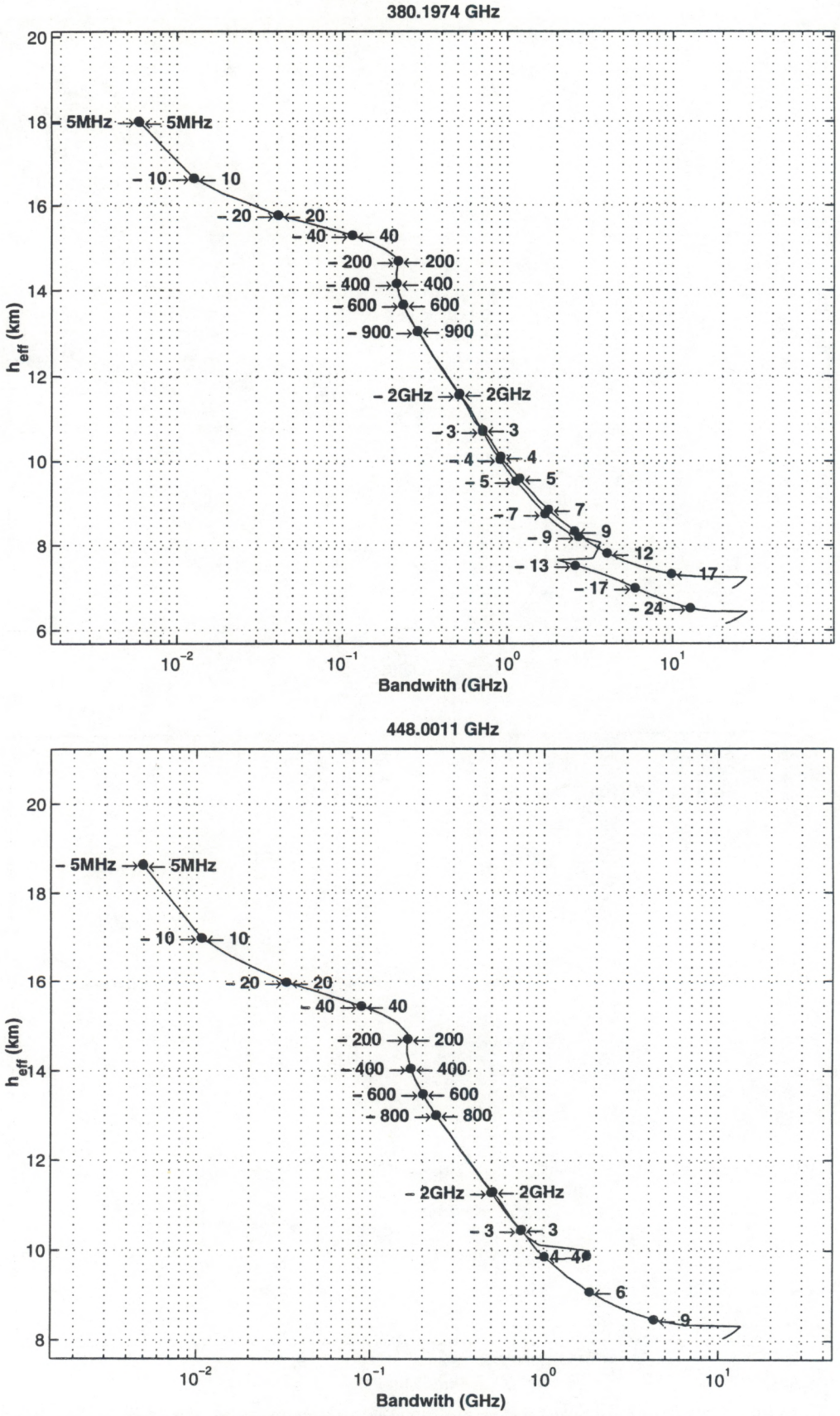

Figure 16b: Natural available bandwidth for water vapor sounding for 380.1974 and 448.0011 GHz water vapor lines for summer and low latitude conditions, satellite nadir view over ocean background. The arrows and numbers indicate frequency offsets from the respective absorption line center.

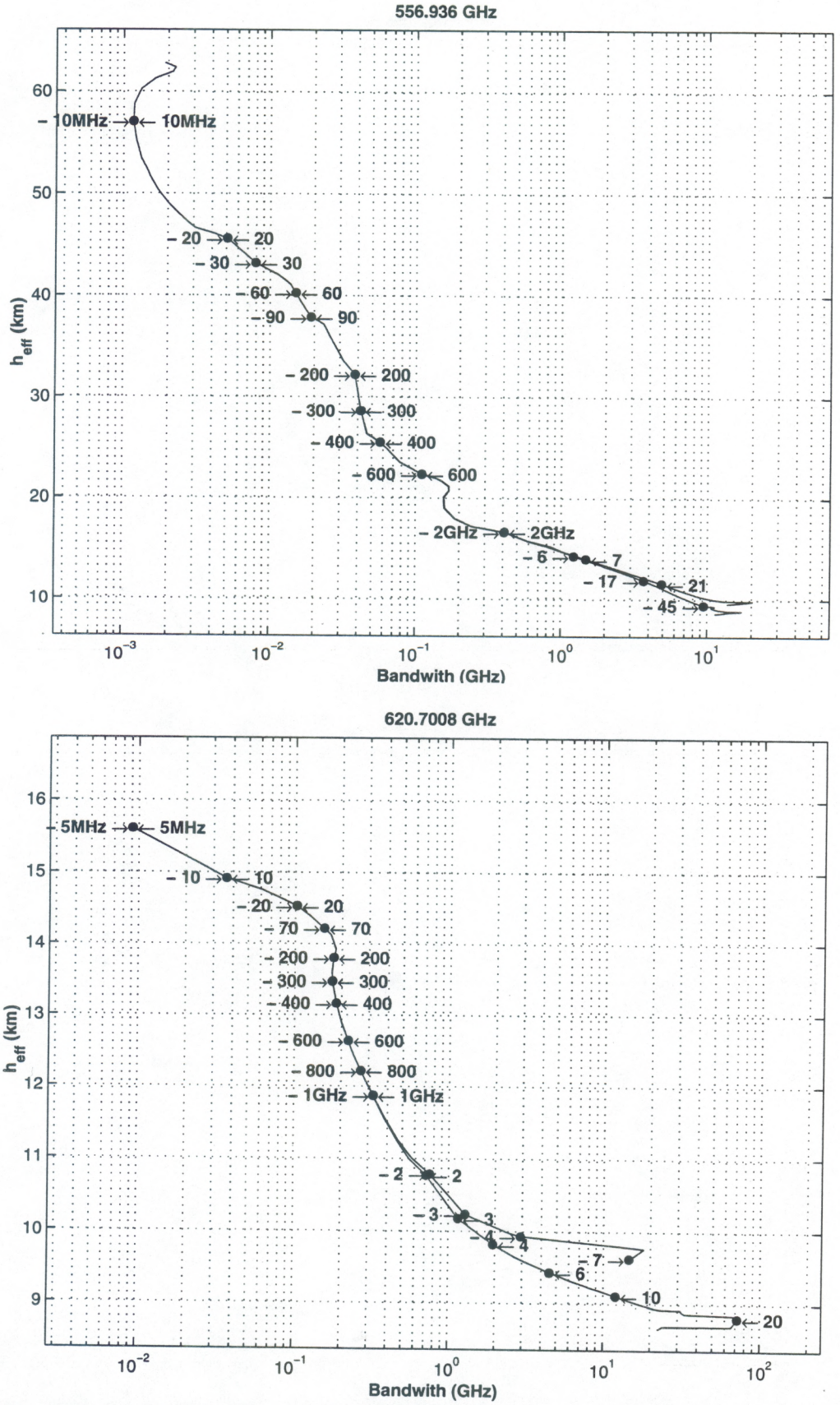

Figure 16c: Natural available bandwidth for water vapor sounding for 556.9360 and 620.7008 GHz water vapor lines for summer and low latitude conditions, satellite nadir view over ocean background. The arrows and numbers indicate frequency offsets from the respective absorption line center.

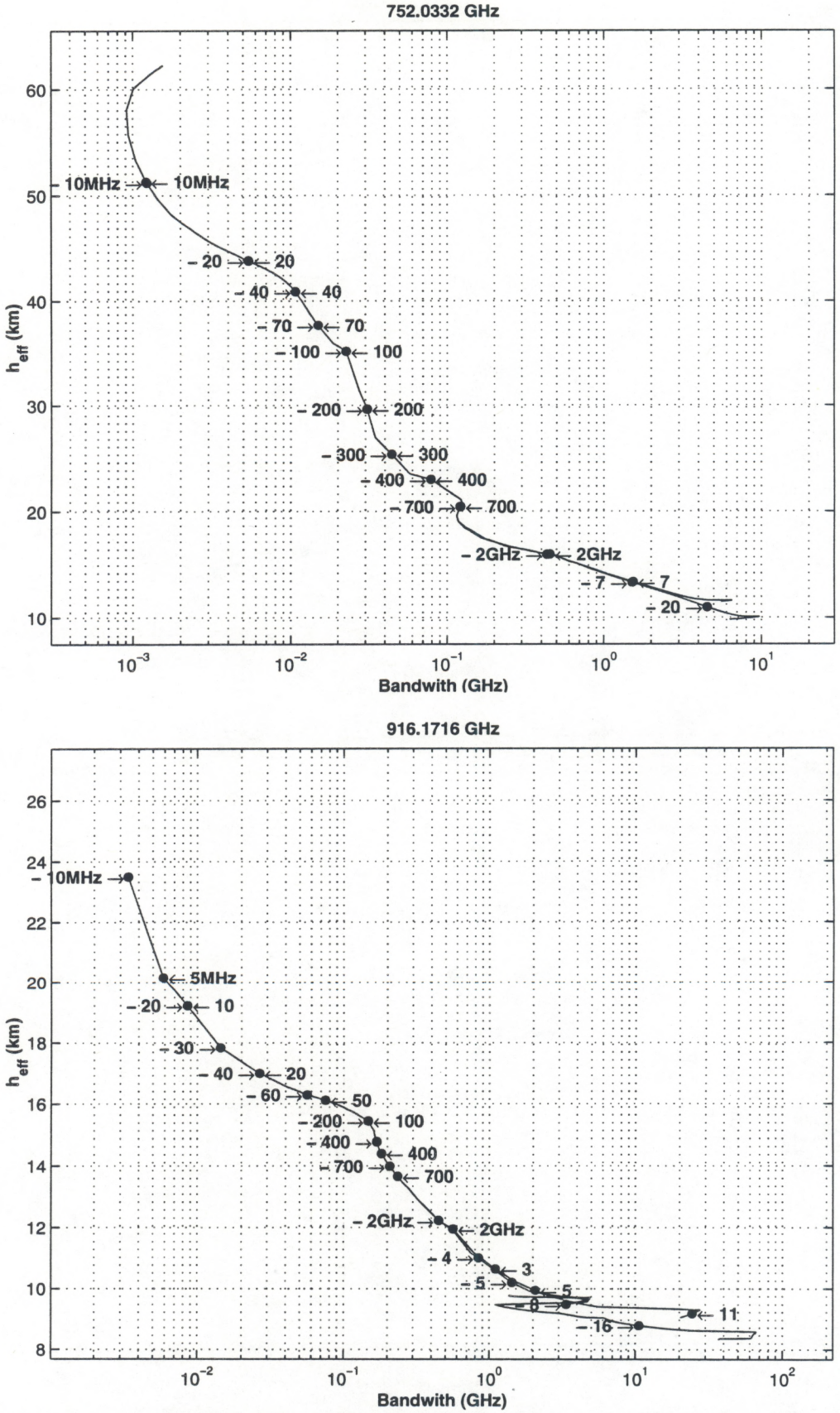

Figure 16d: Natural available bandwidth for water vapor sounding for 752.0332 and 916.1716 GHz water vapor lines for summer and low latitude conditions, satellite nadir view over ocean background. The arrows and numbers indicate frequency offsets from the respective absorption line center.

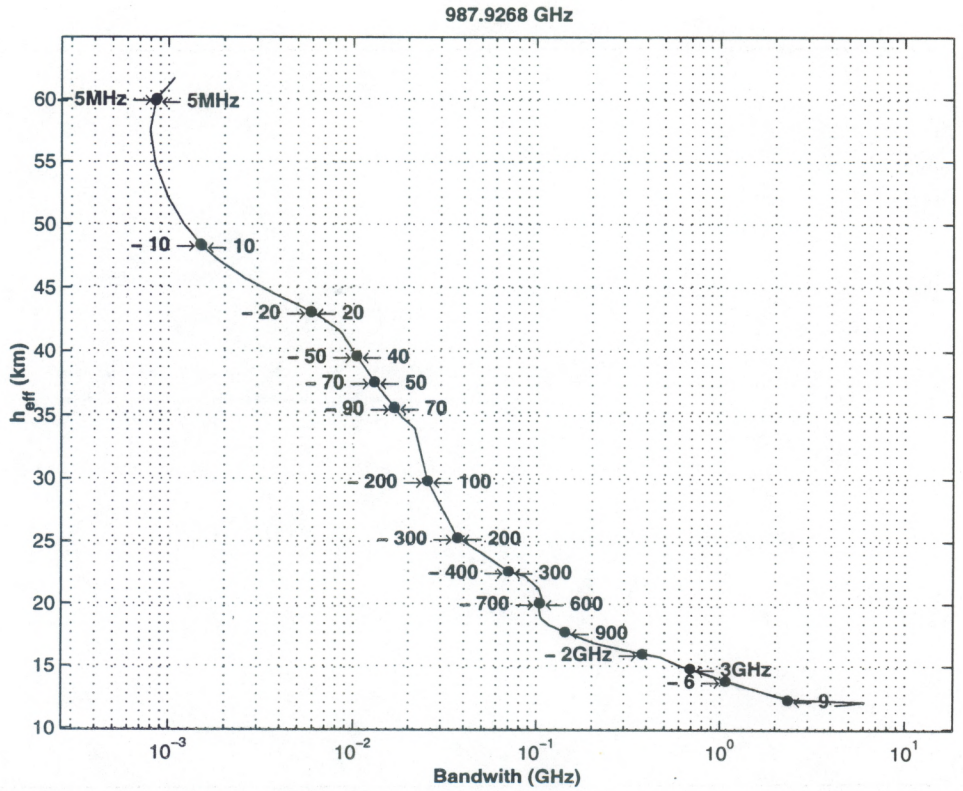

Figure 16d: Natural available bandwidth for water vapor sounding for 987.9268 GHz water vapor line for summer and low latitude conditions, satellite nadir view over ocean background. The arrows and numbe

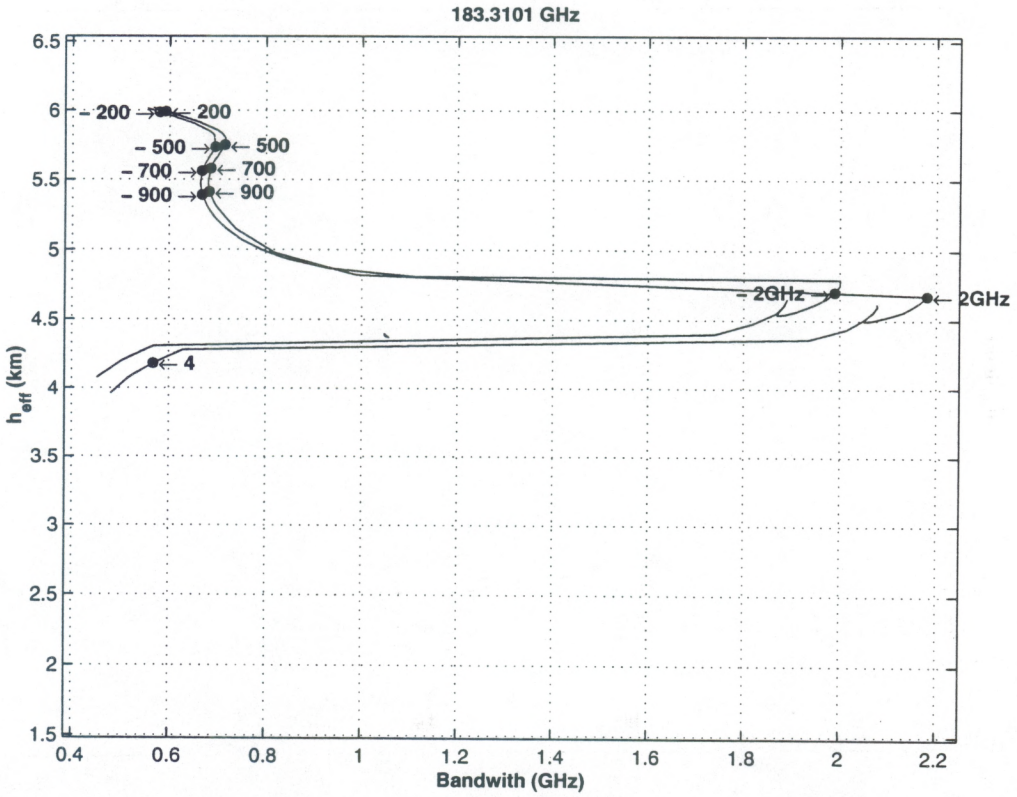

Figure 17a: Natural available bandwidth for water vapor sounding for 183.3101 GHz water vapor line for winter and high latitude conditions, satellite nadir view over ocean background. The arrows and numbers indicate frequency offsets from the respective absorption line center.

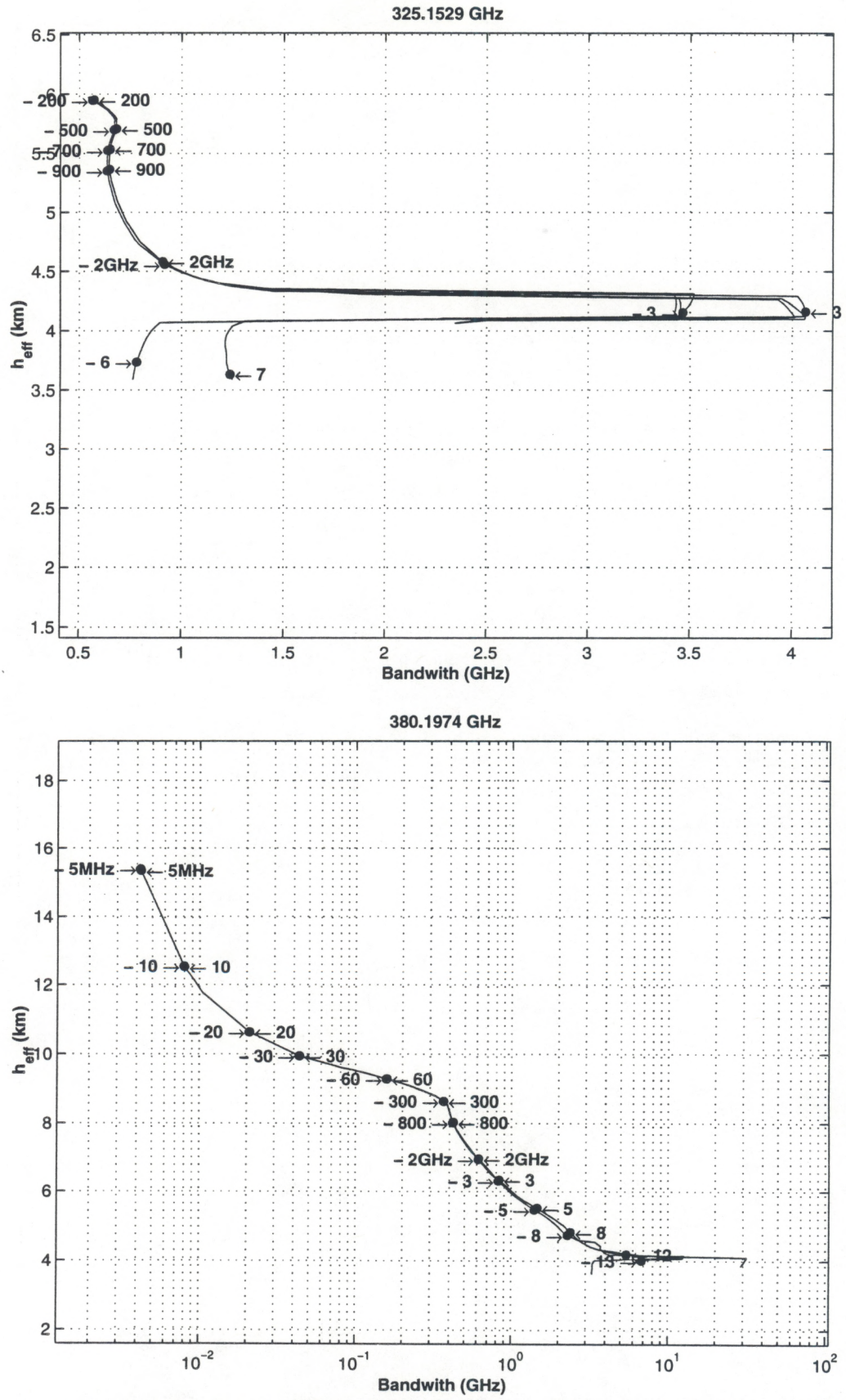

Figure 17b: Natural available bandwidth for water vapor sounding for 325.1529 and 380.1974 GHz water vapor lines for winter and high latitude conditions, satellite nadir view over ocean background. The arrows and numbers indicate frequency offsets from the respective absorption line center.

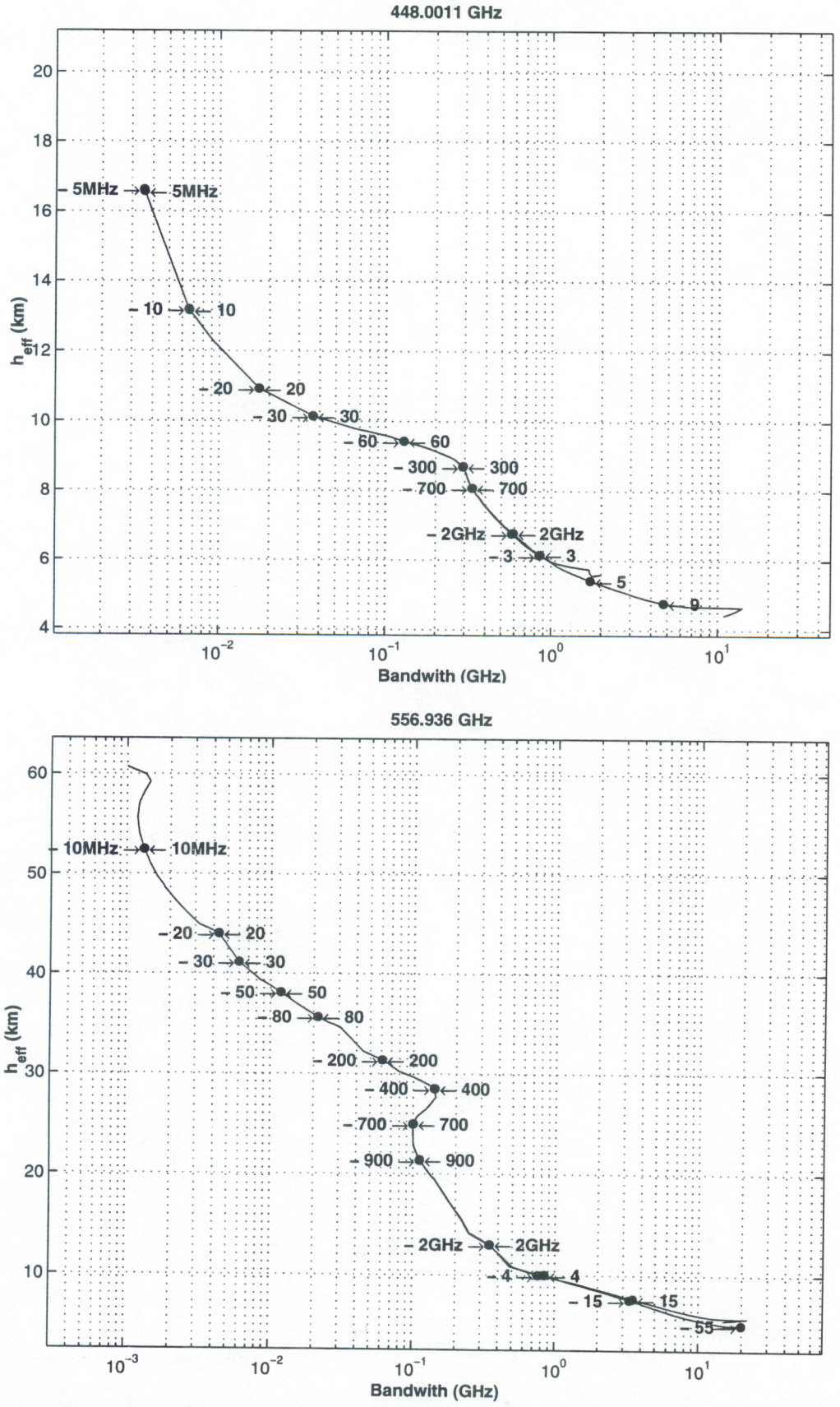

Figure 17c: Natural available bandwidth for water vapor sounding for 448.0011 and 556.9360 GHz water vapor lines for winter and high latitude conditions, satellite nadir view over ocean background. The arrows and numbers indicate frequency offsets from the respective absorption line center.

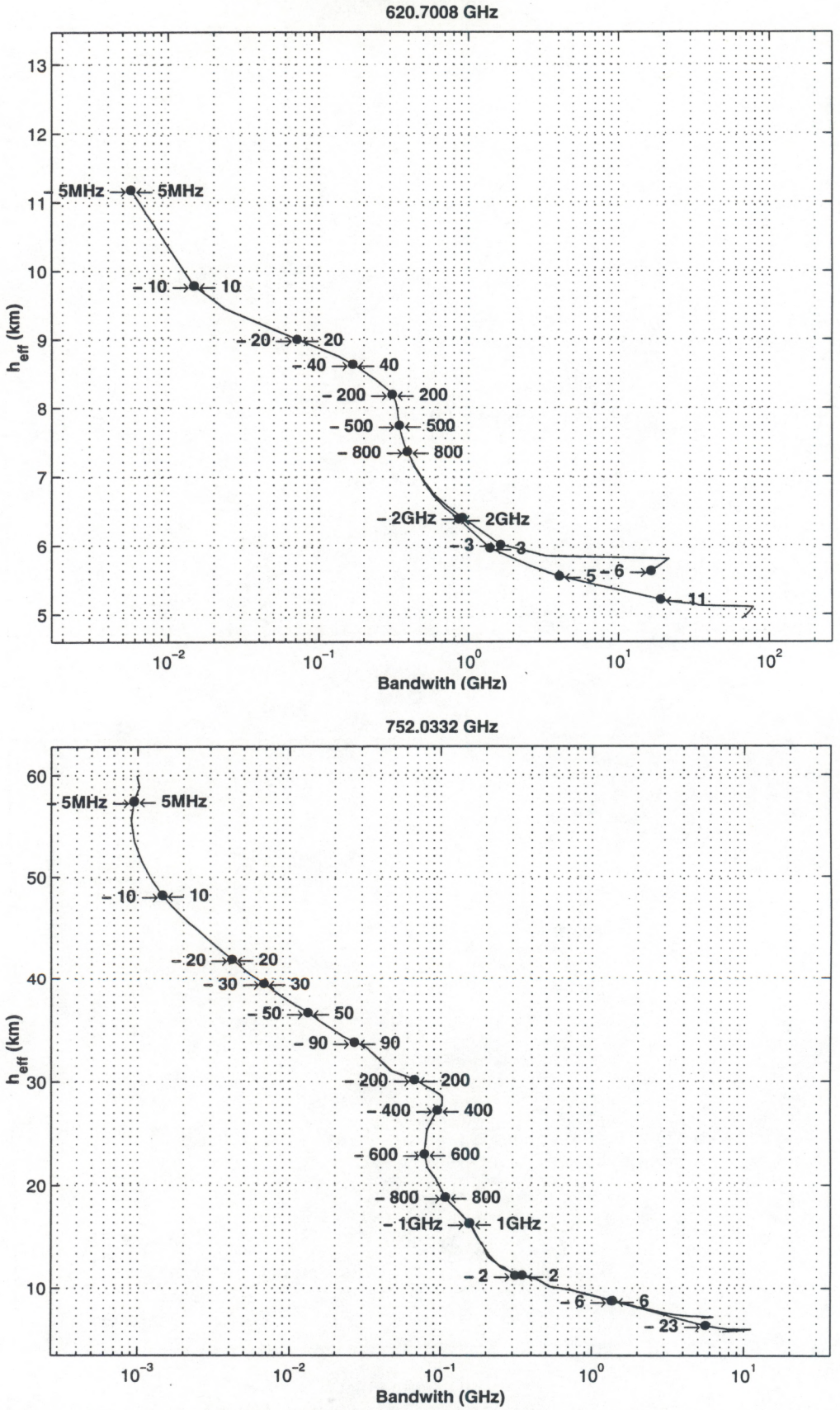

Figure 17d: Natural available bandwidth for water vapor sounding for 620.7008 and 752.0332 GHz water vapor lines for winter and high latitude conditions, satellite nadir view over ocean background. The arrows and numbers indicate frequency offsets from the respective absorption line center.

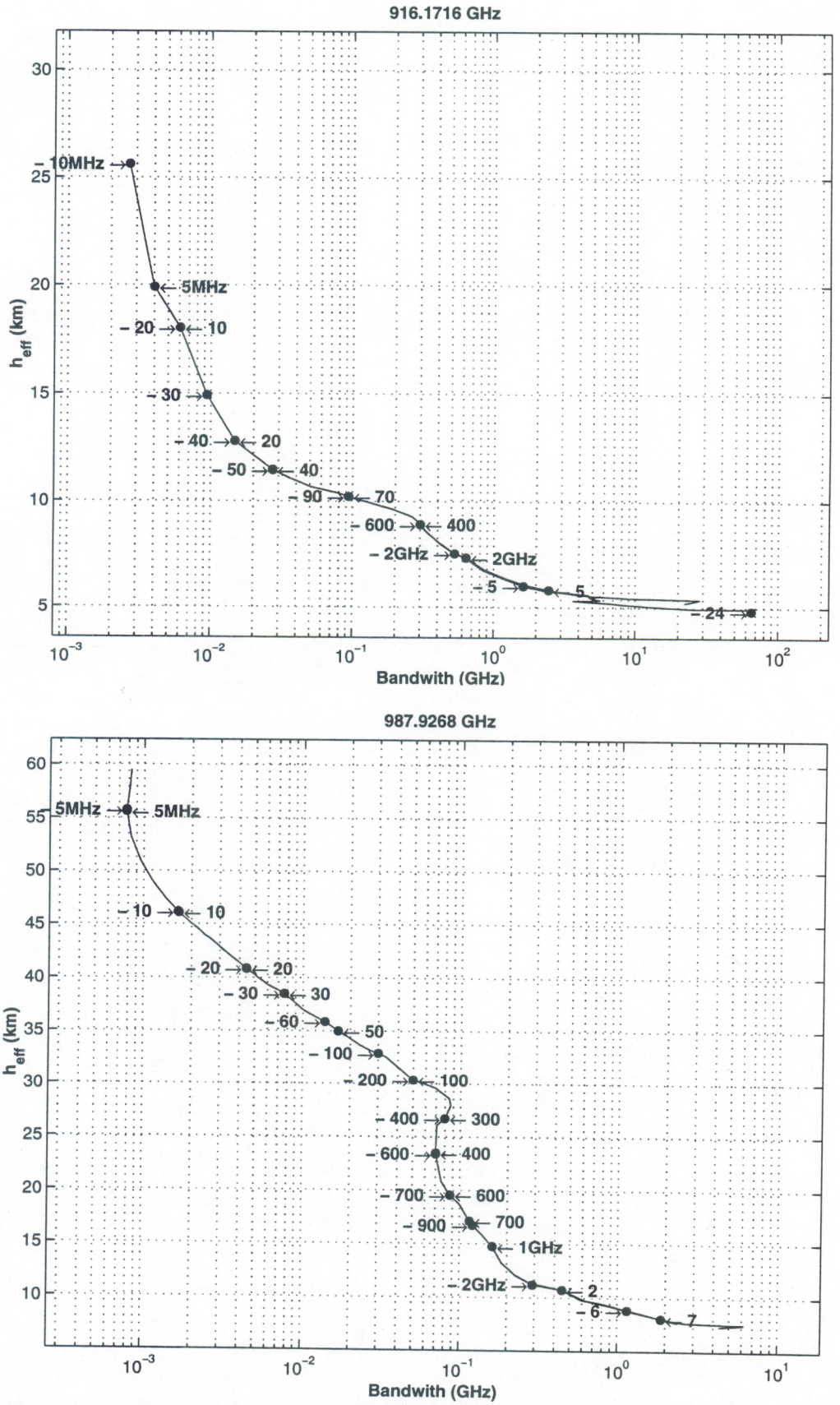

Figure 17e: Natural available bandwidth for water vapor sounding for 916.1716 and 987.9268 GHz water vapor lines for winter and high latitude conditions, satellite nadir view over ocean background. The arrows and numbers indicate frequency offsets from the respective absorption line center.

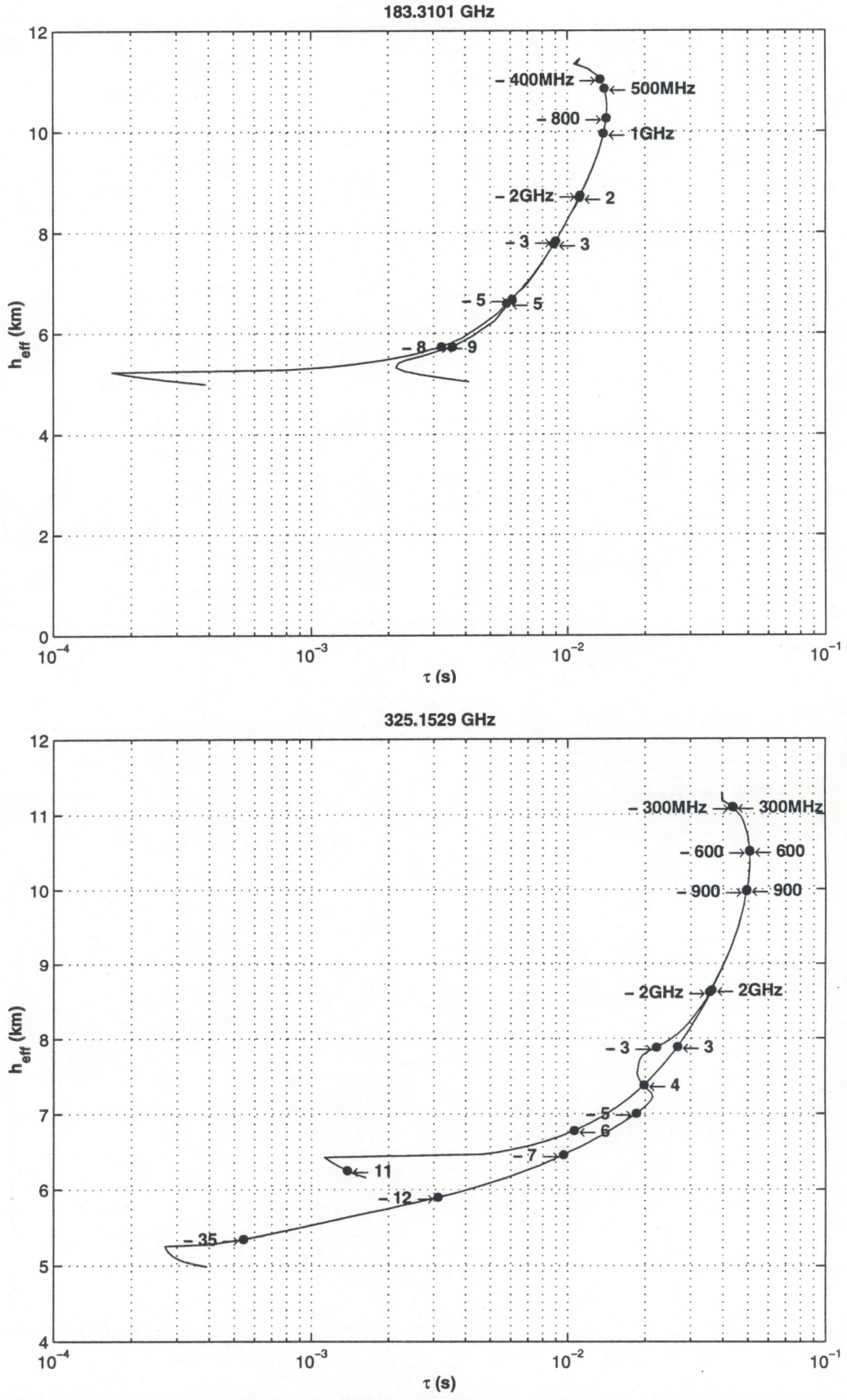

Figure 18a: Integration time for water vapor sounding for 183.3101 and 325.1529 GHz water vapor lines for summer and low latitude conditions, satellite nadir view over ocean background. The arrows and numbers indicate frequency offsets from the respective absorption line center.

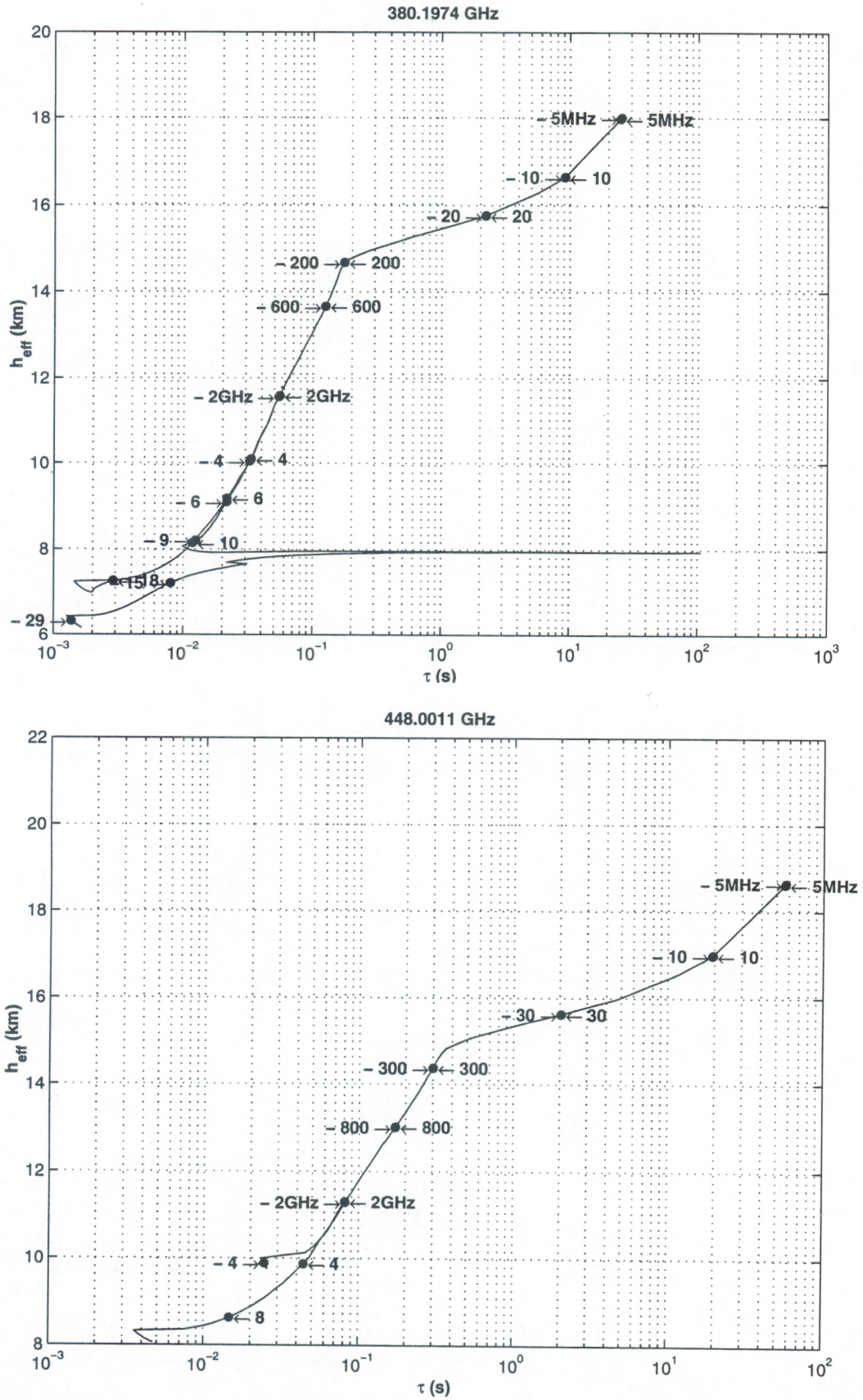

Figure 18b: Integration time for water vapor sounding for 380.1974 and 448.0011 GHz water vapor lines for summer and low latitude conditions, satellite nadir view over ocean background. The arrows and numbers indicate frequency offsets from the respective absorption line center.

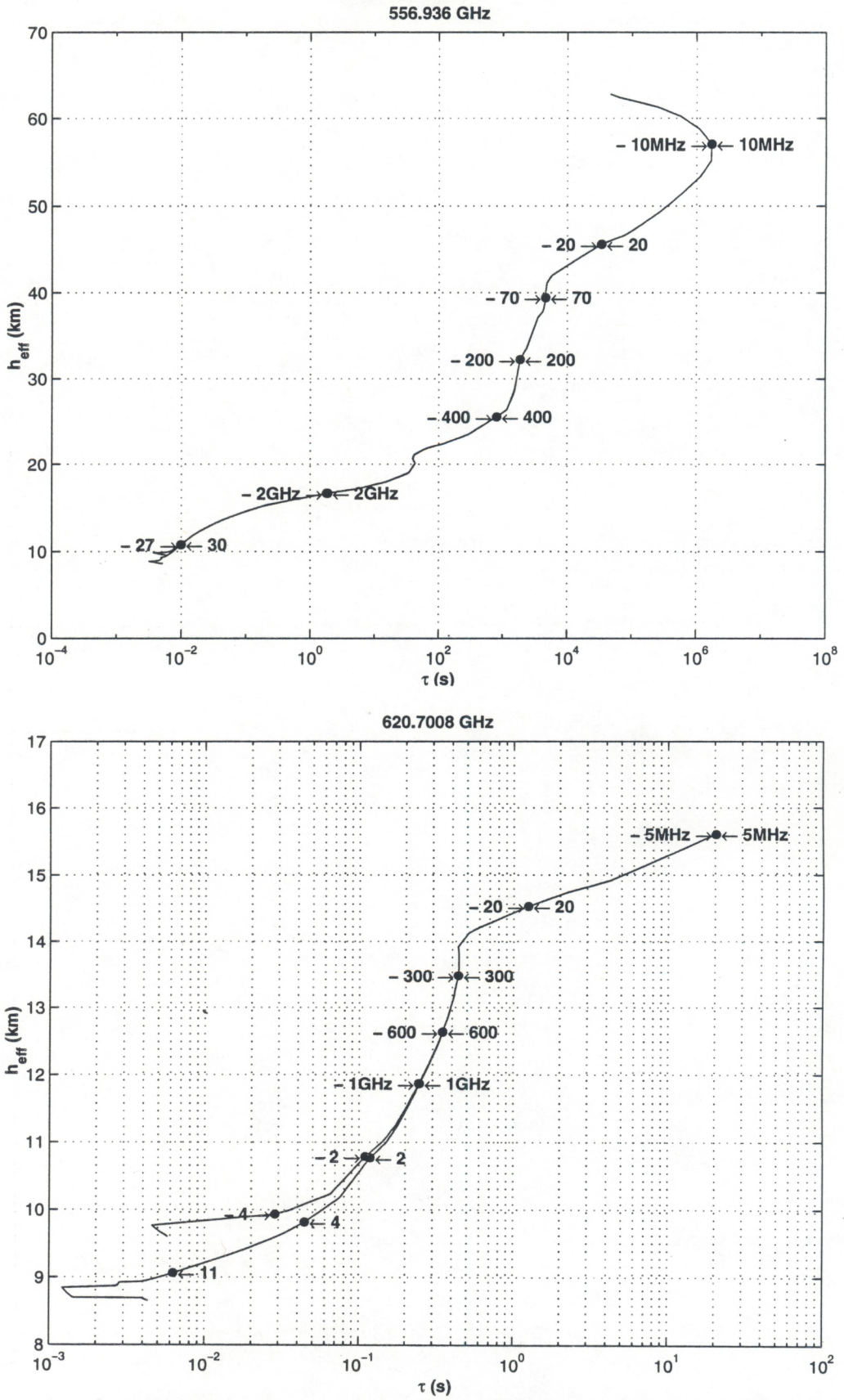

Figure 18c: Integration time for water vapor sounding for 556.9360 and 620.7008 GHz water vapor lines for summer and low latitude conditions, satellite nadir view over ocean background. The arrows and numbers indicate frequency offsets from the respective absorption line center.

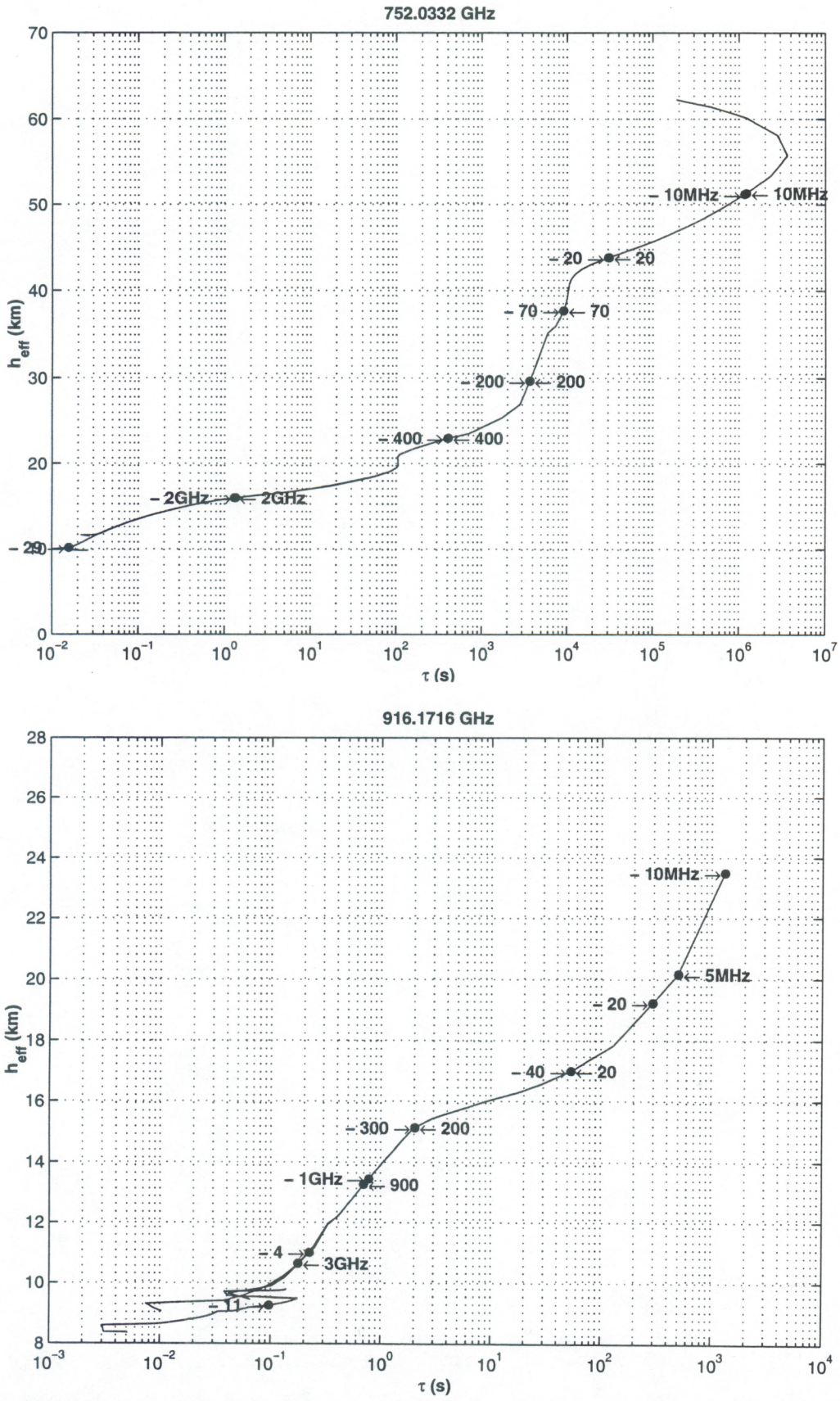

Figure 18d: Integration time for water vapor sounding for 752.0332 and 916.1716 GHz water vapor lines for summer and low latitude conditions, satellite nadir view over ocean background. The arrows and numbers indicate frequency offsets from the respective absorption line center.

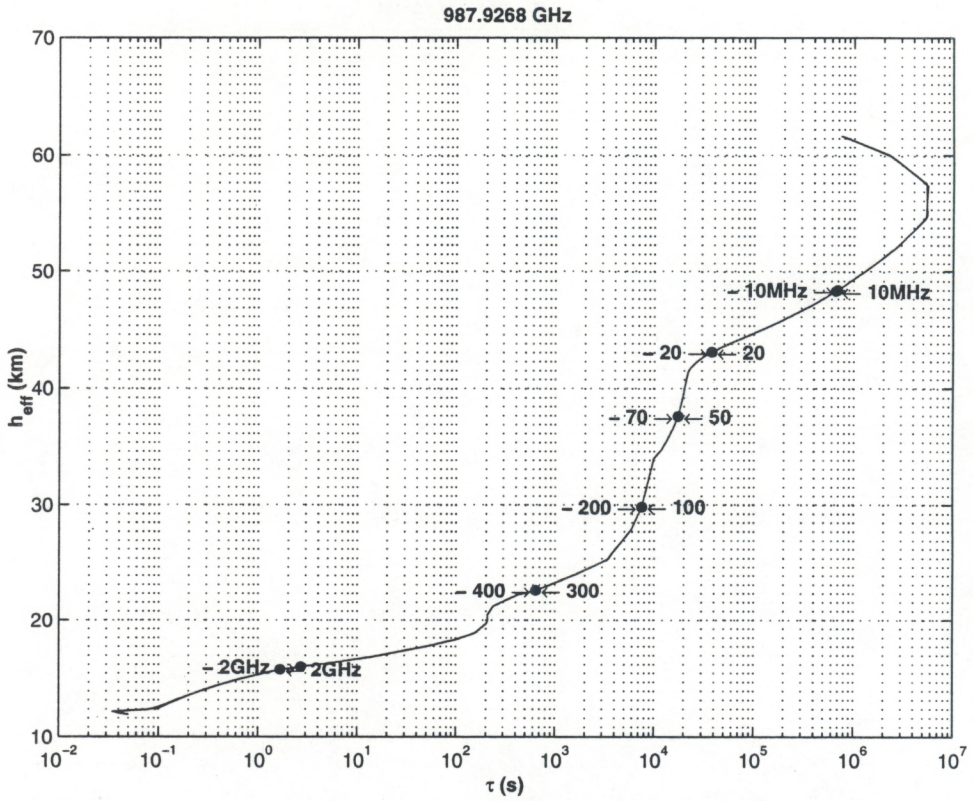

Figure 18e: Integration time for water vapor sounding for 987.9268 GHz water vapor line for summer and low latitude conditions, satellite nadir view over ocean background. The arrows and numbers indicat

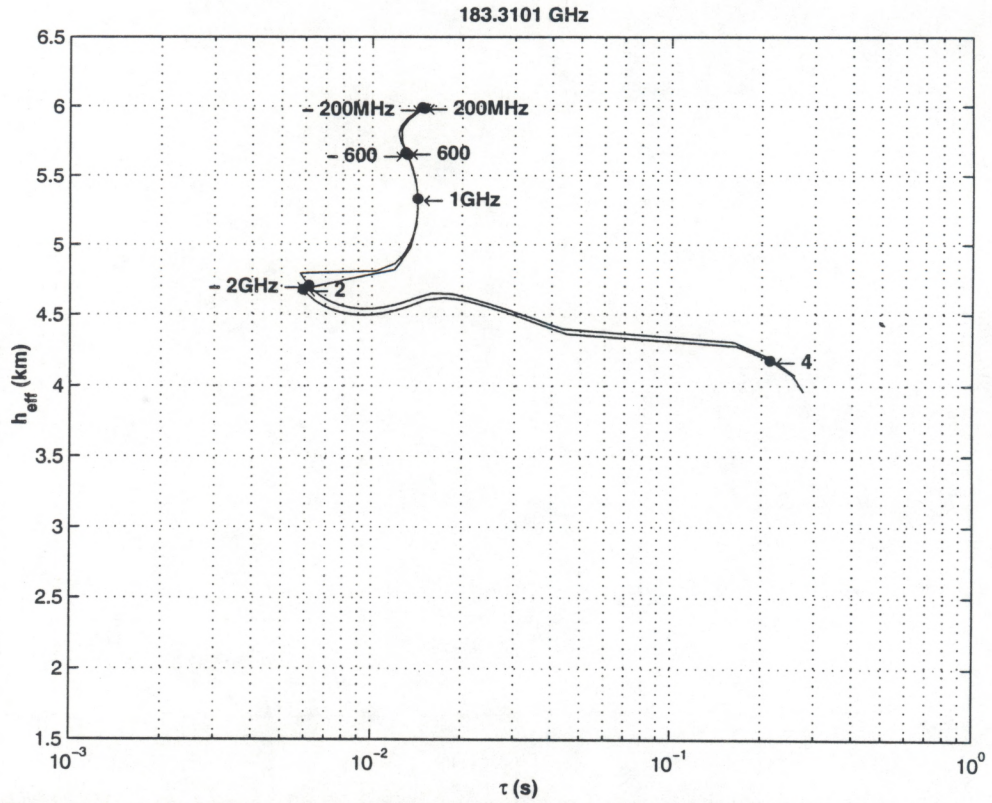

Figure 19a: Integration time for water vapor sounding for 183.3101 GHz water vapor line for winter and high latitude conditions, satellite nadir view over ocean background. The arrows and numbers indicate frequency offsets from the respective absorption line center.

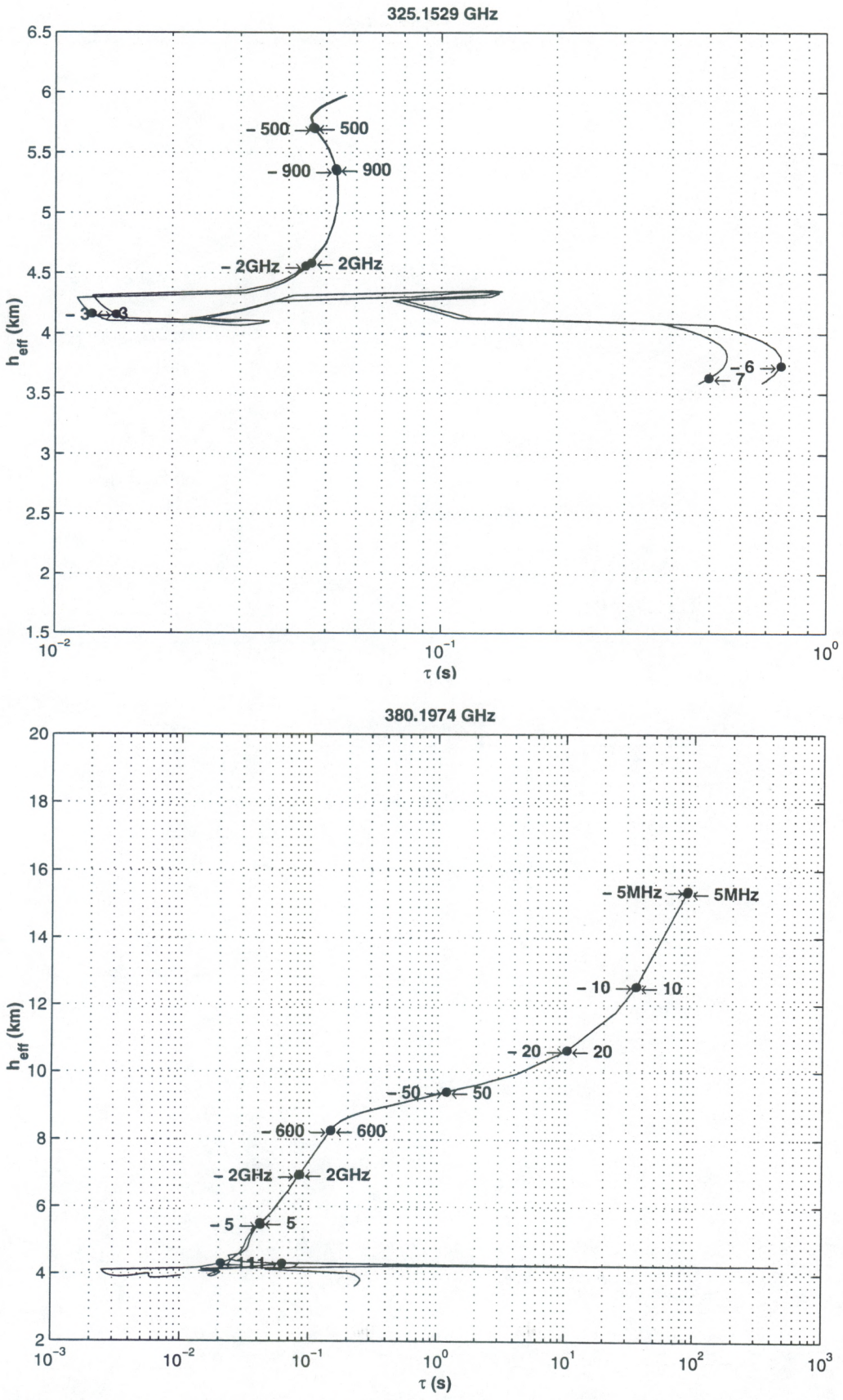

Figure 19b: Integration time for water vapor sounding for 325.1529 and 380.1974 GHz water vapor line for winter and high latitude conditions, satellite nadir view over ocean background. The arrows and numbers indicate frequency offsets from the respective absorption line center.

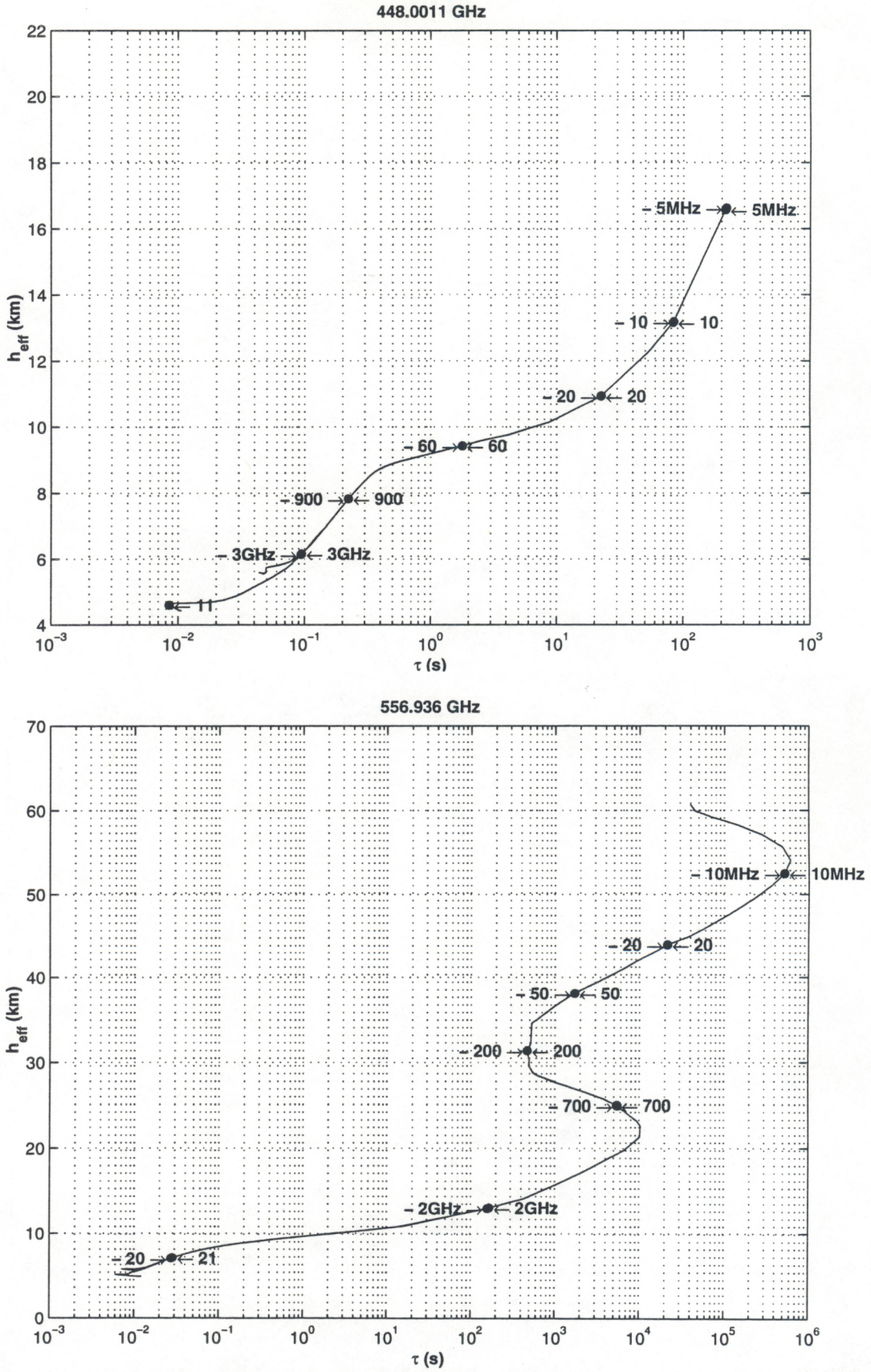

Figure 19c: Integration time for water vapor sounding for 448.0011 and 556.9360 GHz water vapor line for winter and high latitude conditions, satellite nadir view over ocean background. The arrows and numbers indicate frequency offsets from the respective absorption line center.

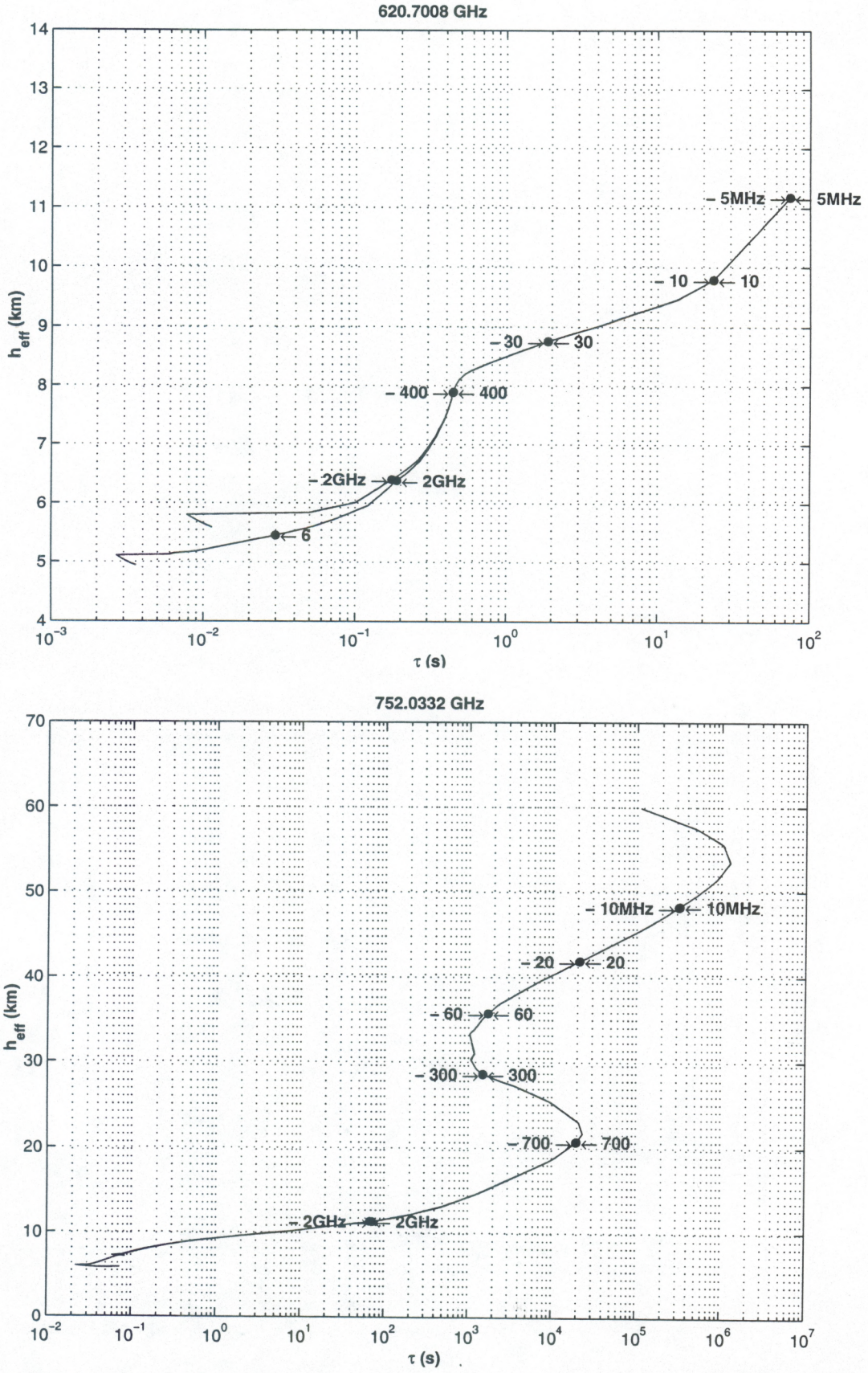

Figure 19d: Integration time for water vapor sounding for 620.7008 and 752.0332 GHz water vapor line for winter and high latitude conditions, satellite nadir view over ocean background. The arrows and numbers indicate frequency offsets from the respective absorption line center.

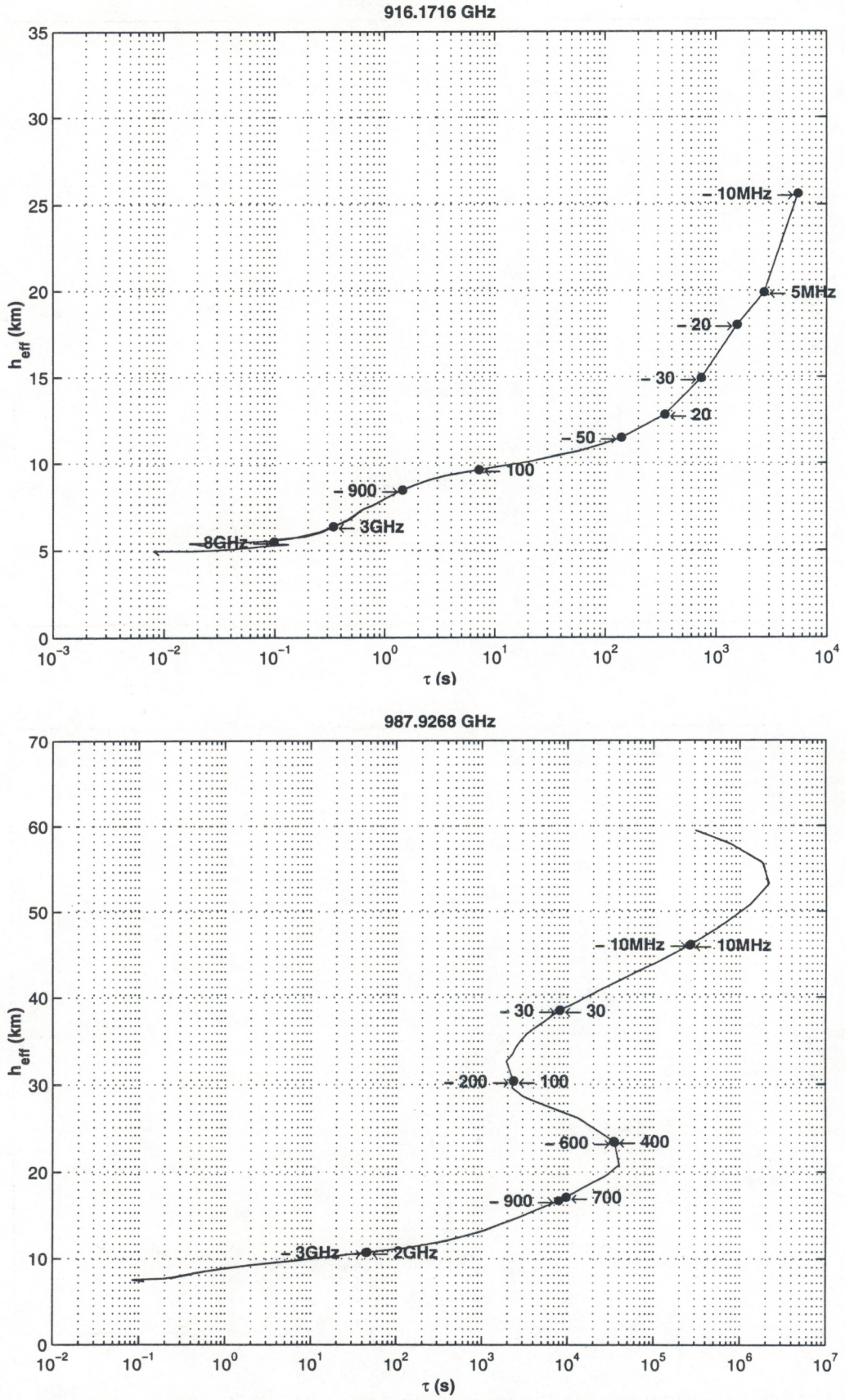

Figure 19e: Integration time for water vapor sounding for 916.1716 and 987.9268 GHz water vapor line for winter and high latitude conditions, satellite nadir view over ocean background. The arrows and numbers indicate frequency offsets from the respective absorption line center.

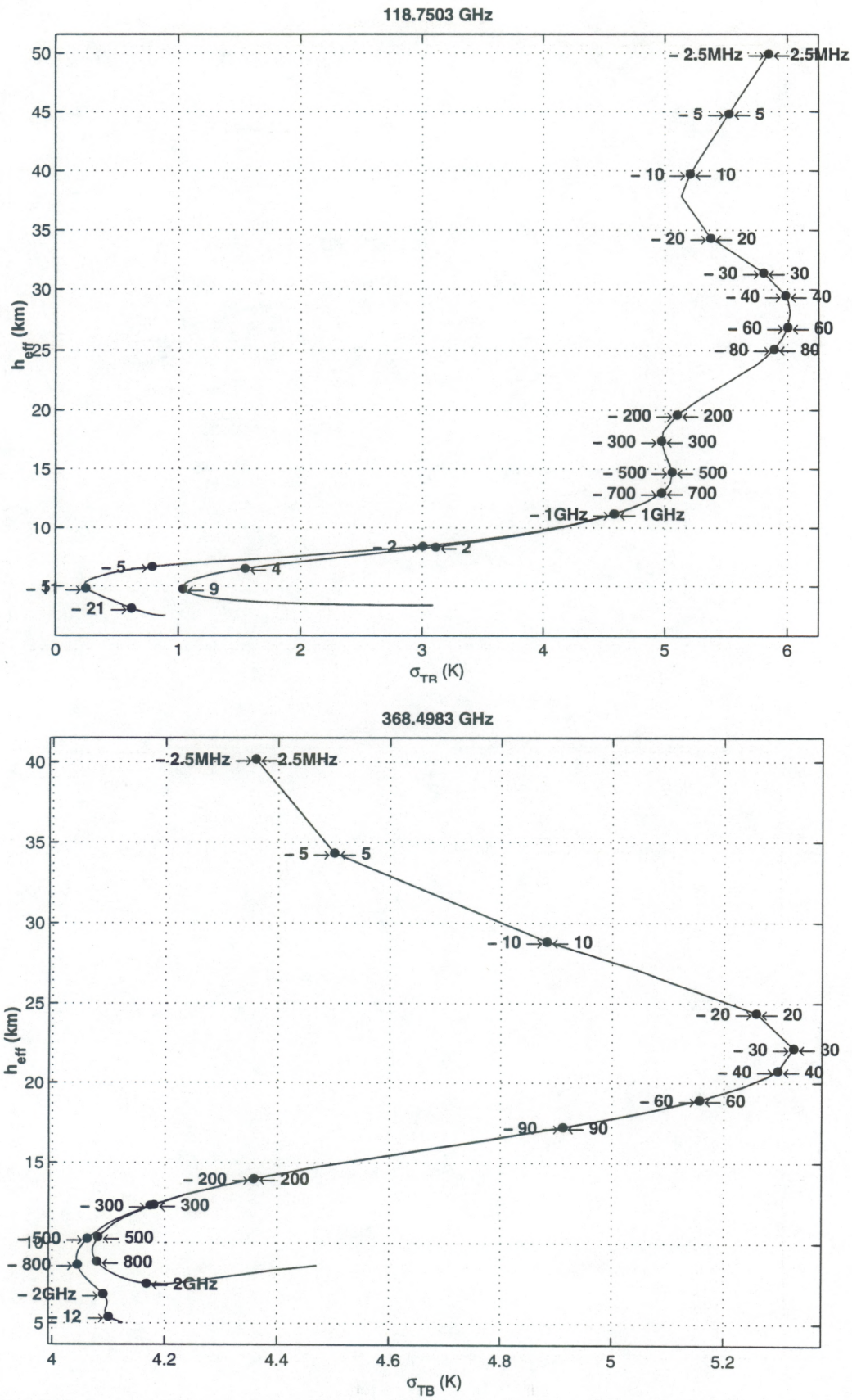

Figure 20a: RMS signal versus sounding height for 118.7503 and 368.4983 GHz oxygen absorption lines for summer and low latitude conditions, satellite nadir view over ocean background. The arrows and numbers indicate frequency offsets from the respective absorption line center.

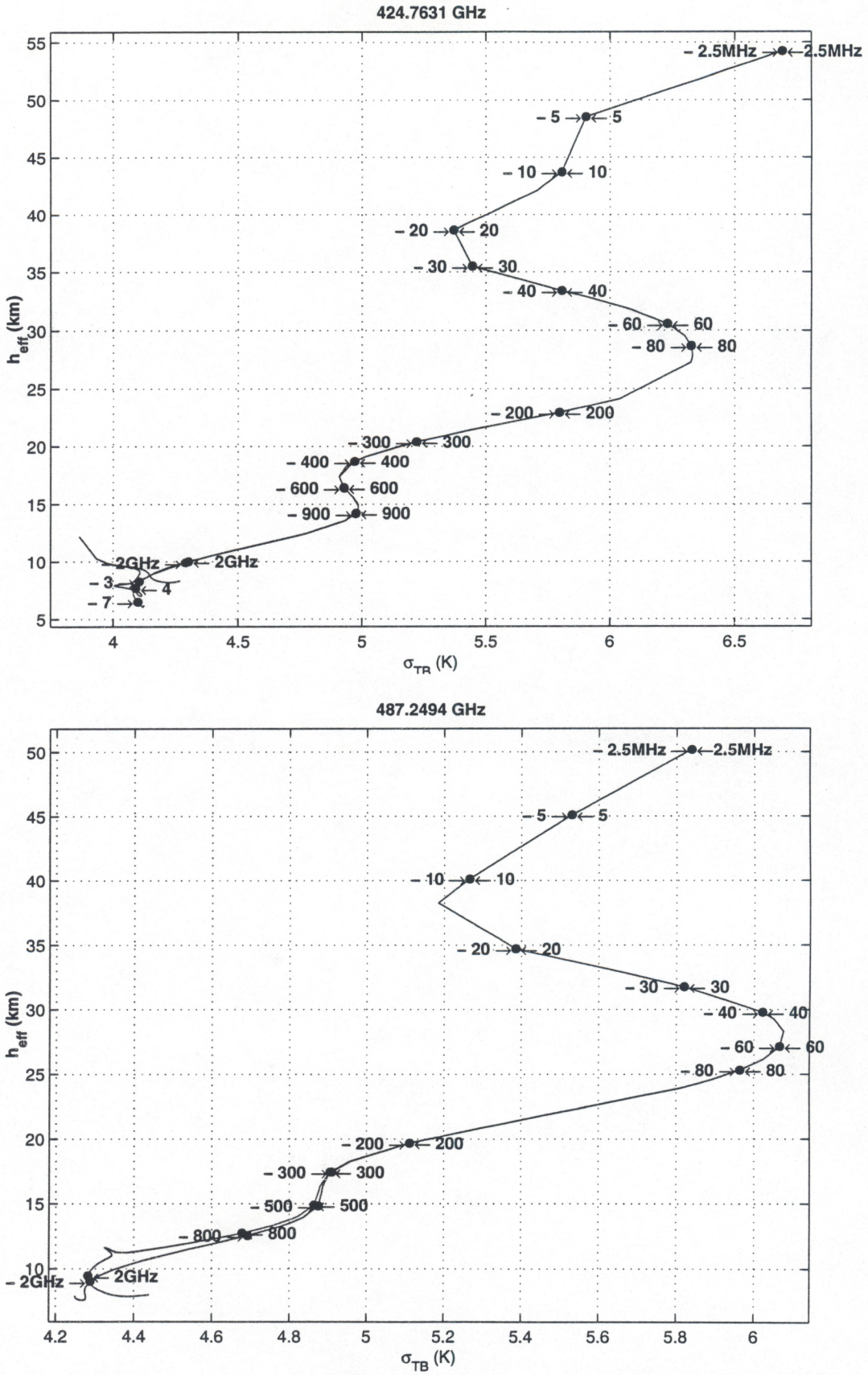

Figure 20b: RMS signal versus sounding height for 424.7631 and 487.2494 GHz oxygen absorption lines for summer and low latitude conditions, satellite nadir view over ocean background. The arrows and numbers indicate frequency offsets from the respective absorption line center.

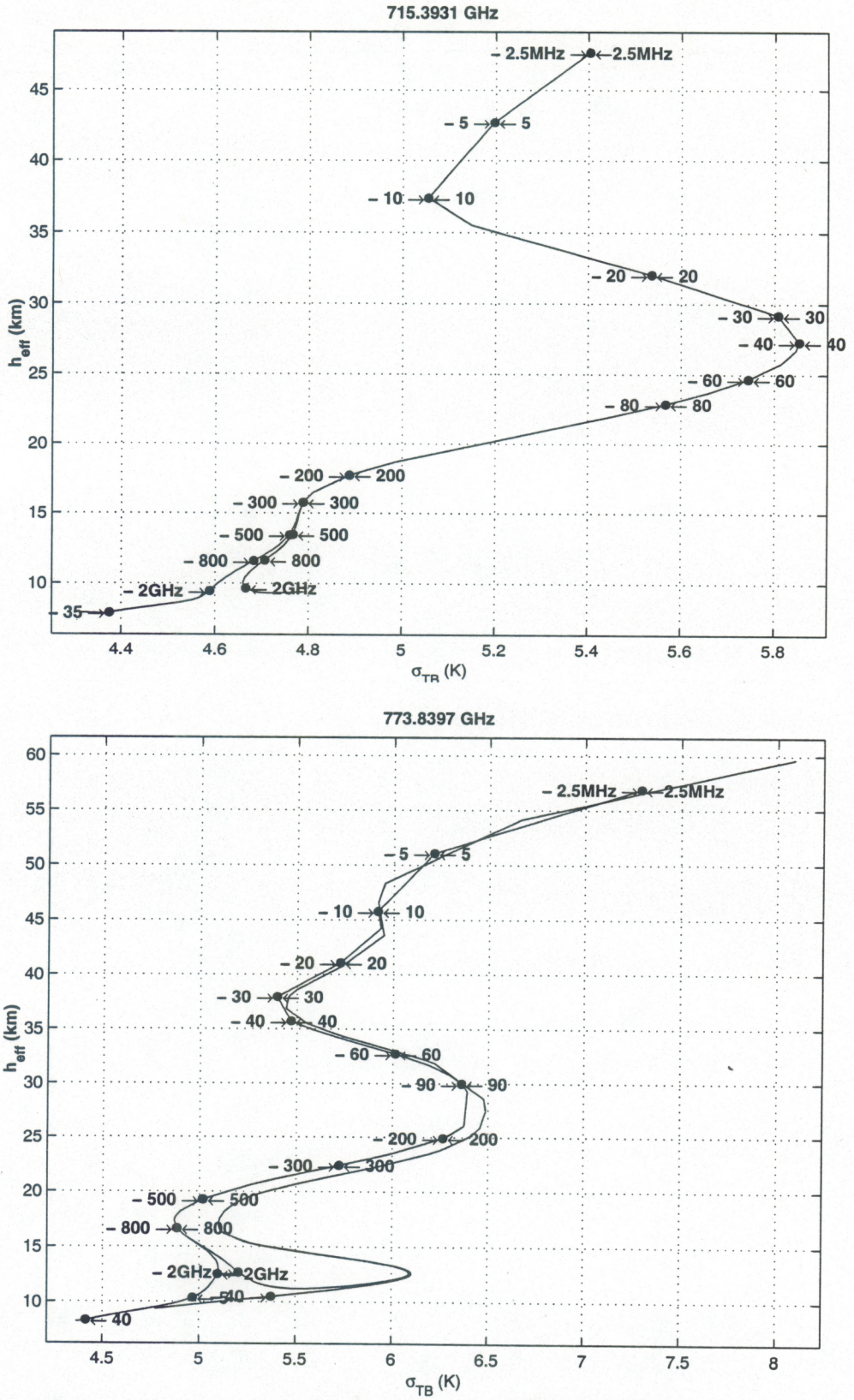

Figure 20c: RMS signal versus sounding height for 715.3931 and 773.8397 GHz oxygen absorption lines for summer and low latitude conditions, satellite nadir view over ocean background. The arrows and numbers indicate frequency offsets from the respective absorption line center. The double-backed nature of the curves for 773.8397 GHz oxygen line is a result of the close proximity of the 752.0332 GHz water vapor line.

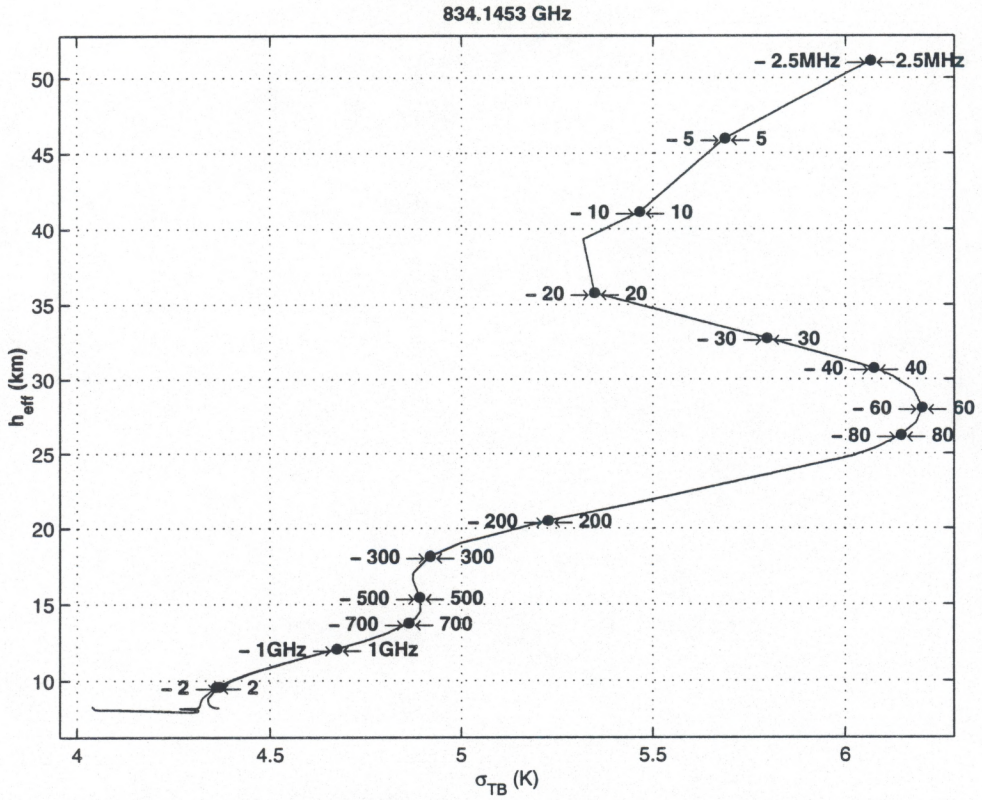

Figure 20d: RMS signal versus sounding height for 837.4453 GHz oxygen absorption line for summer and low latitude conditions, satellite nadir view over ocean background. The arrows and numbers indicat

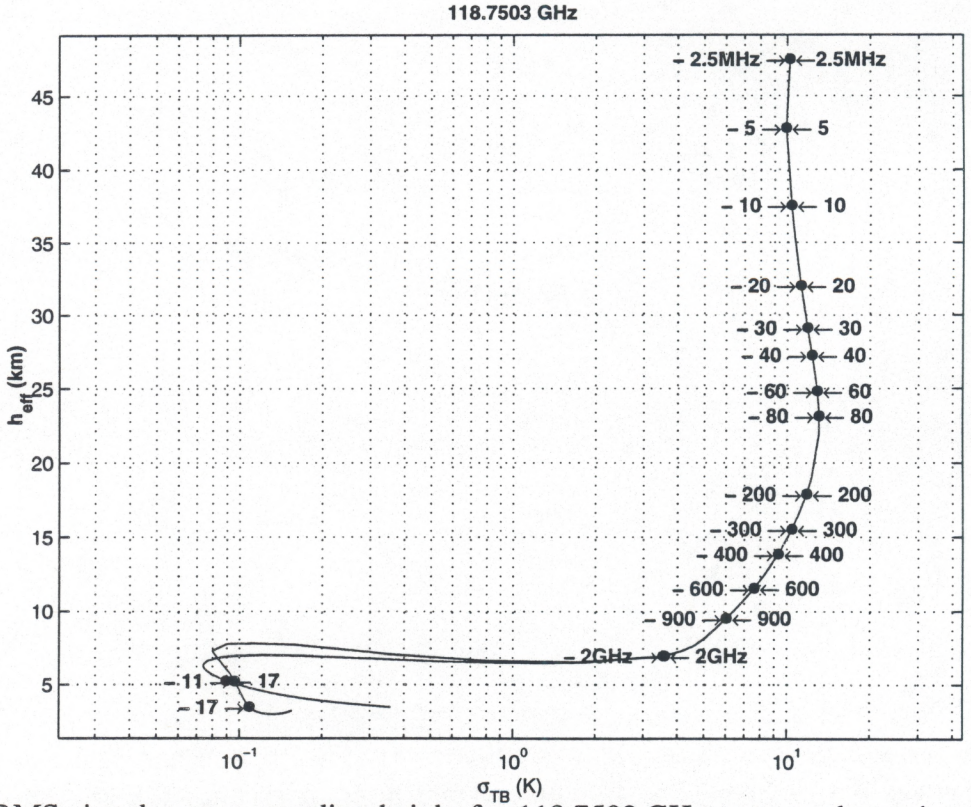

Figure 21a: RMS signal versus sounding height for 118.7503 GHz oxygen absorption line for winter and high latitude conditions, satellite nadir view over ocean background. The arrows and numbers indicate frequency offsets from the respective absorption line center.

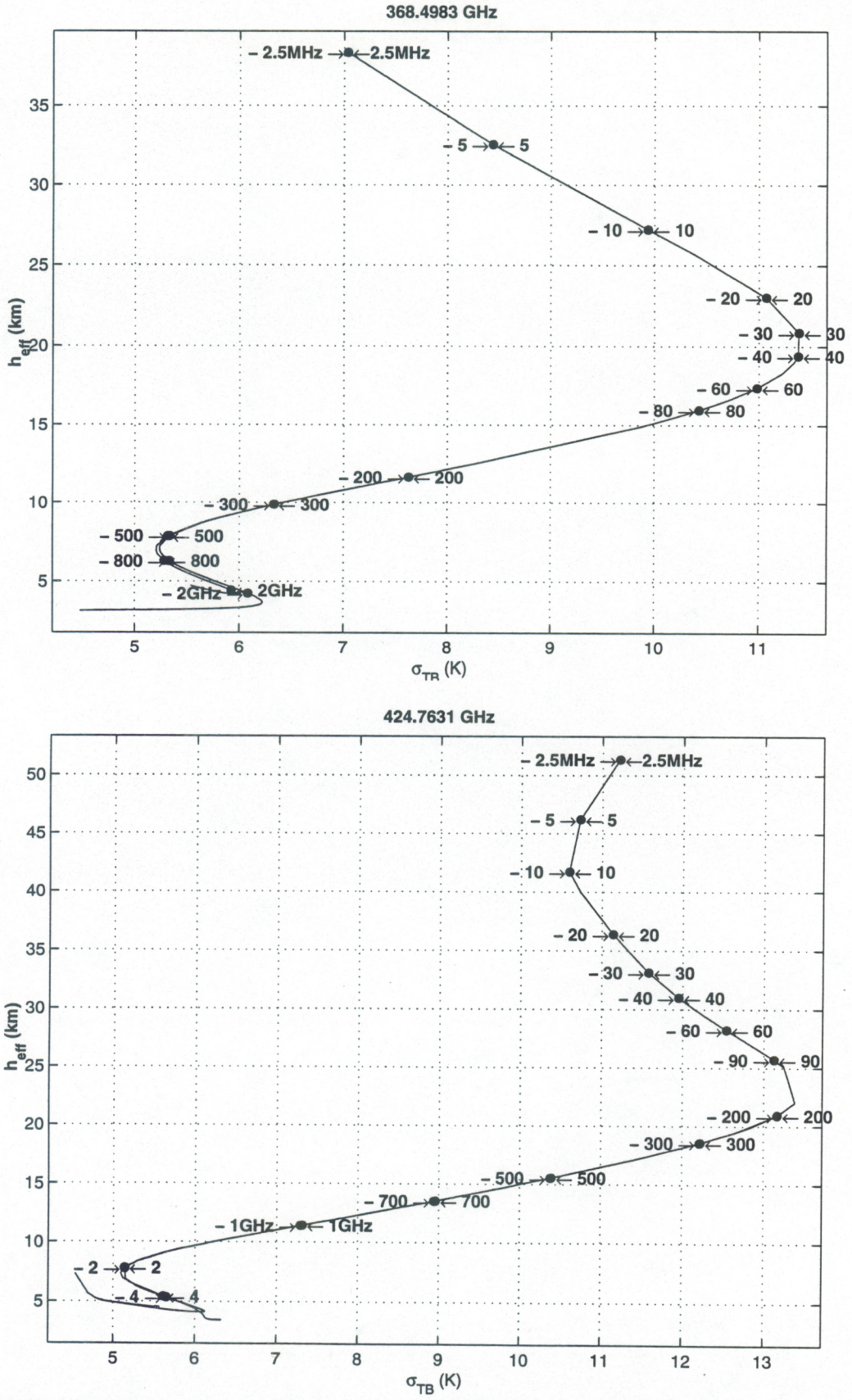

Figure 21b: RMS signal versus sounding height for 368.4983 and 424.7631 GHz oxygen absorption lines for winter and high latitude conditions, satellite nadir view over ocean background. The arrows and numbers indicate frequency offsets from the respective absorption line center.

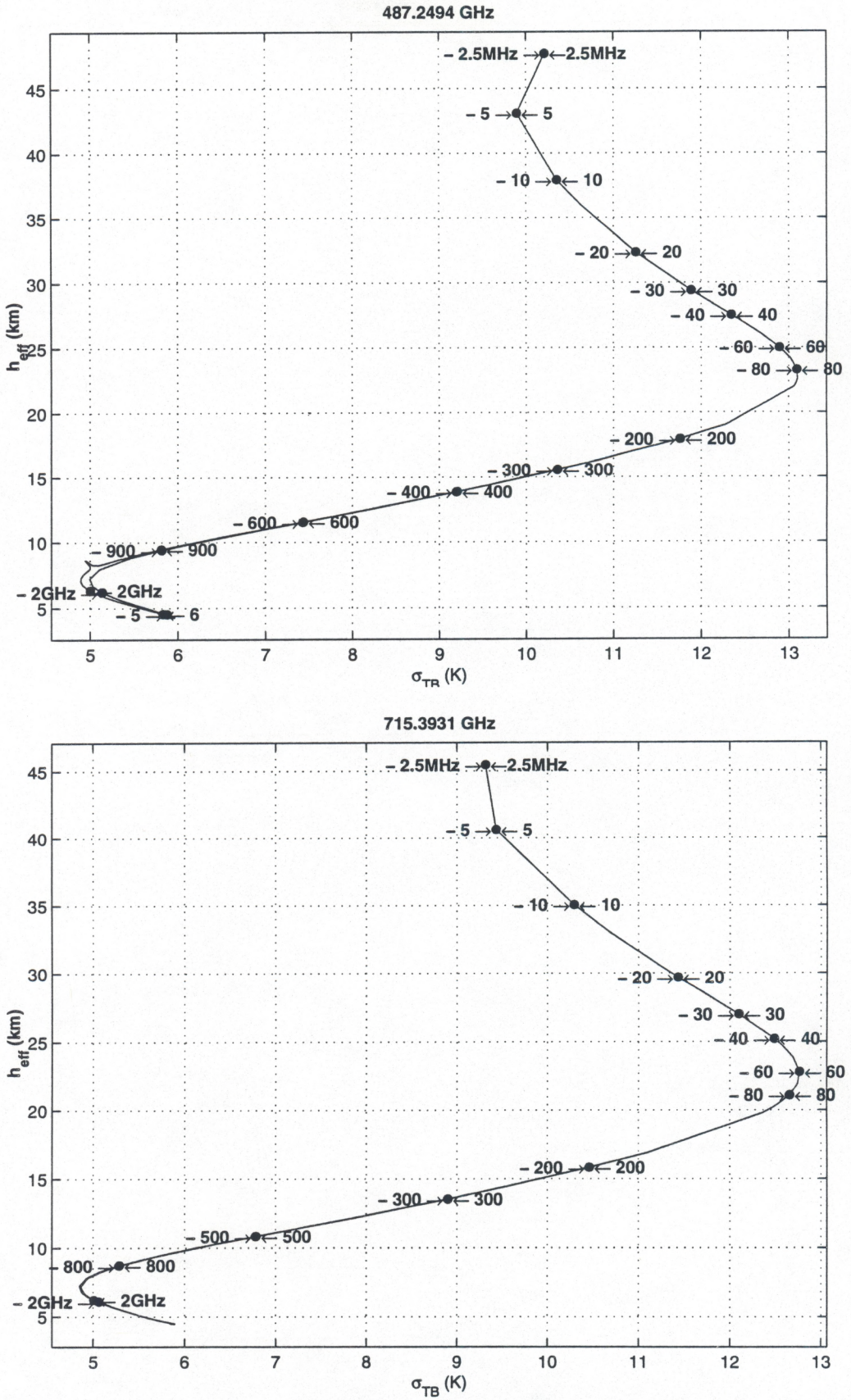

Figure 21c: RMS signal versus sounding height for 487.2494 and 715.3931 GHz oxygen absorption lines for winter and high latitude conditions, satellite nadir view over ocean background. The arrows and numbers indicate frequency offsets from the respective absorption line center.

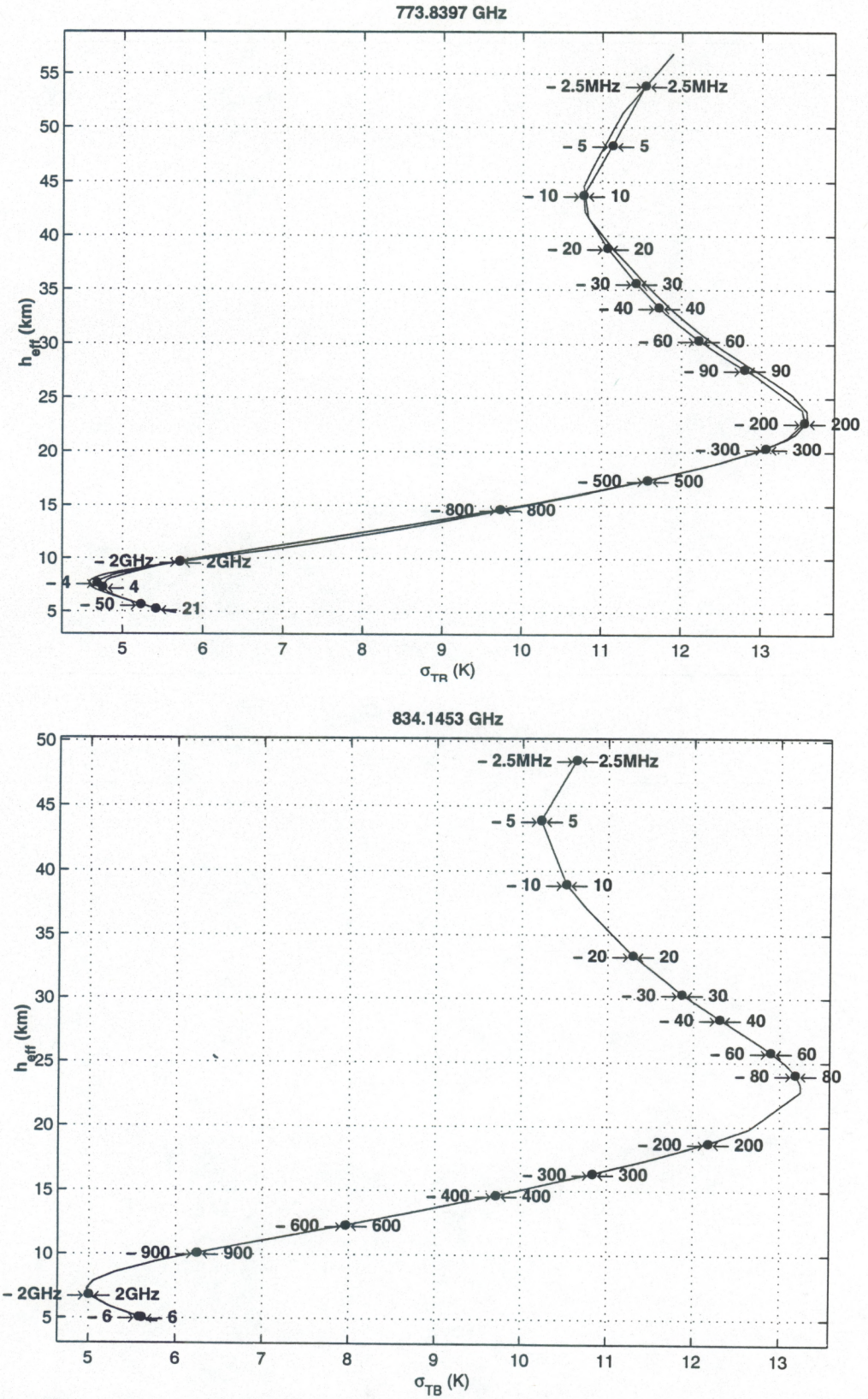

Figure 21d: RMS signal versus sounding height for 773.8397 and 834.1453 GHz oxygen absorption lines for winter and high latitude conditions, satellite nadir view over ocean background. The arrows and numbers indicate frequency offsets from the respective absorption line center. The double-backed nature of the curves for 773.8397 GHz oxygen line is a result of the close proximity of the 752.0332 GHz water vapor line.

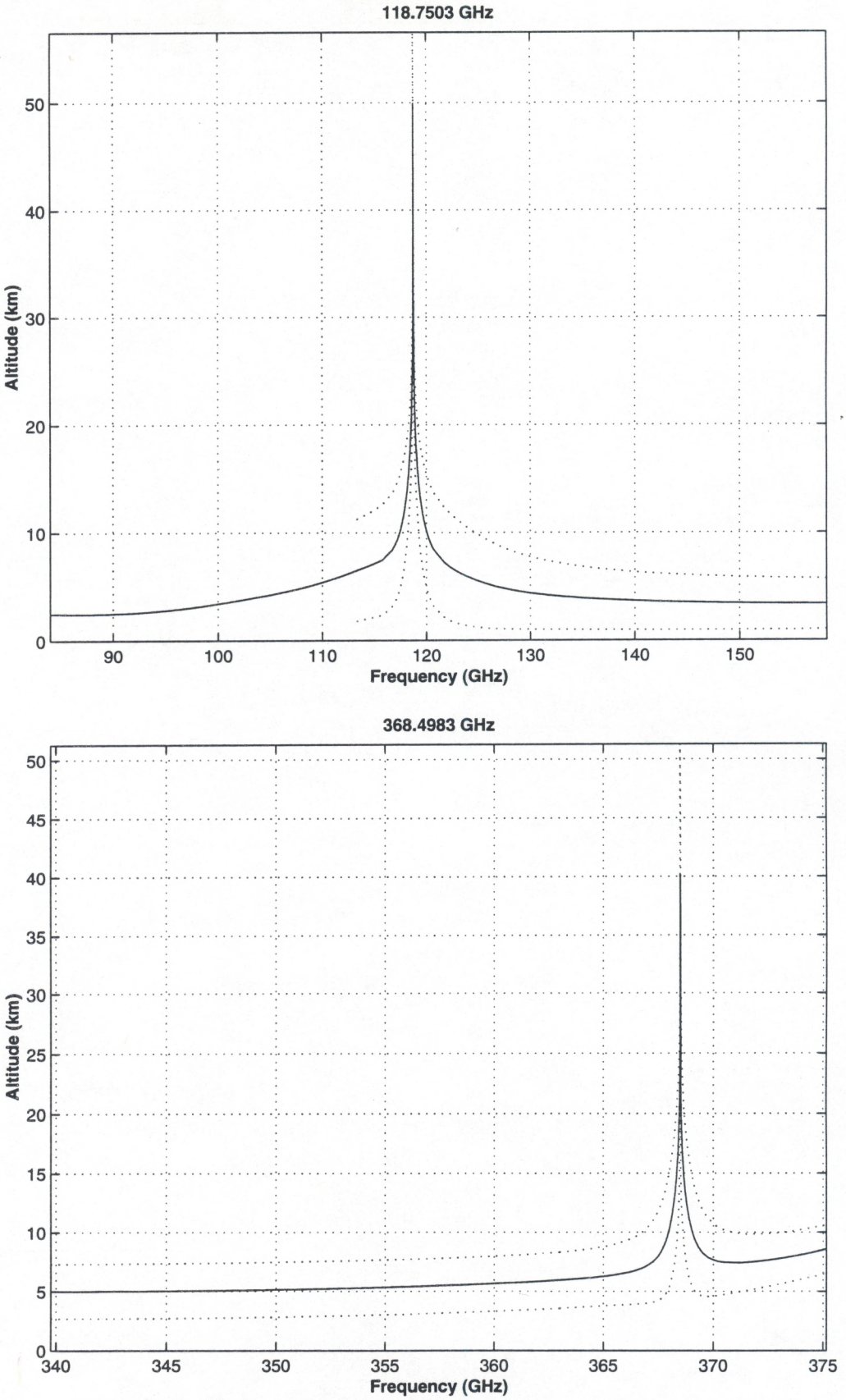

Figure 22a: Effective temperature sounding height h_{eff} along with $h_{eff} \pm \sigma_h$ for 118.7503 and 368.4983 GHz oxygen lines for summer and low latitude conditions, satellite nadir view over ocean background.

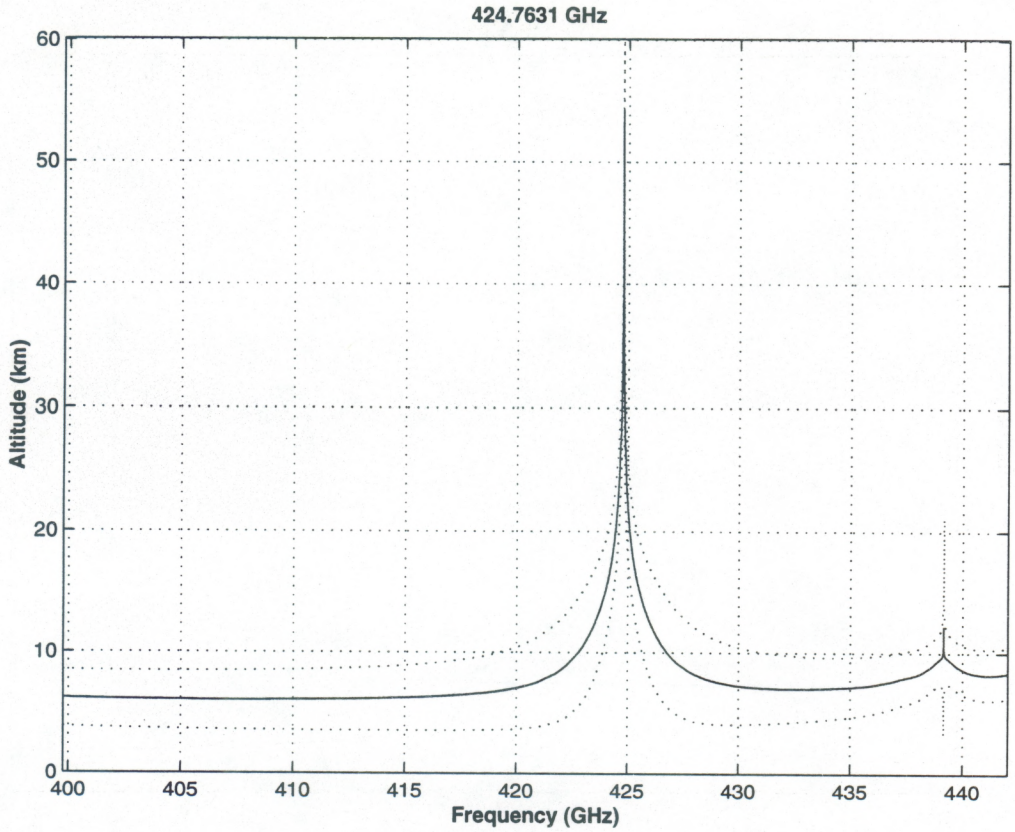

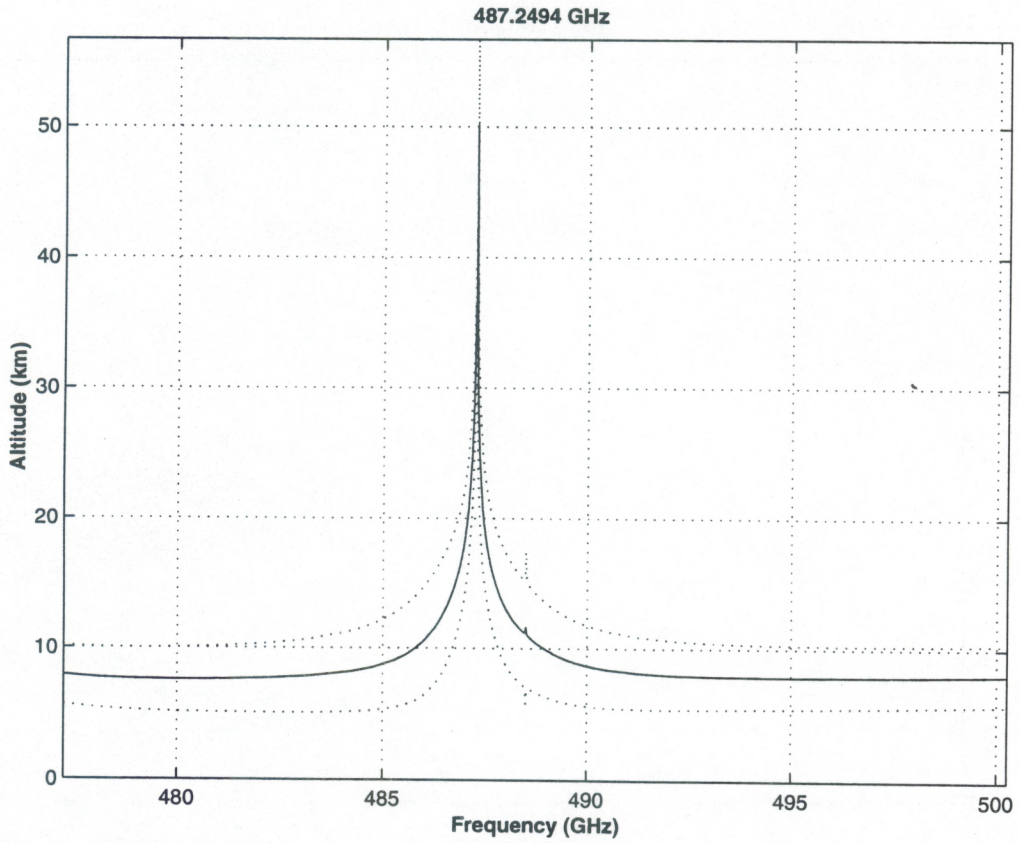

Figure 22b: Effective temperature sounding height h_{eff} along with $h_{eff} \pm \sigma_h$ for 424.7631 and 487.2494 GHz oxygen lines for summer and low latitude conditions, satellite nadir view over ocean background.

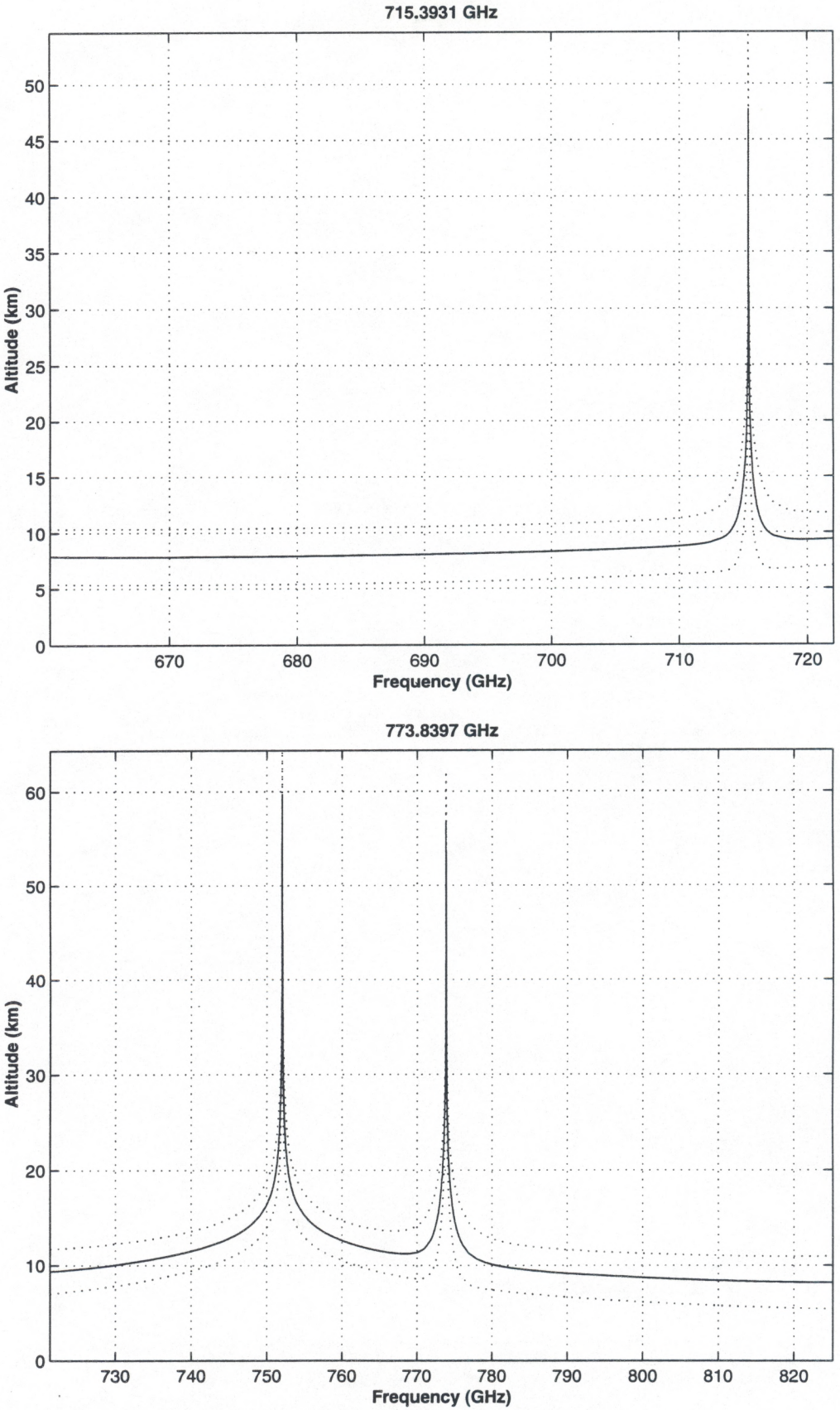

Figure 22c: Effective temperature sounding height h_{eff} along with $h_{eff} \pm \sigma_h$ for 715.3931 and 773.8397 GHz oxygen lines for summer and low latitude conditions, satellite nadir view over ocean background.

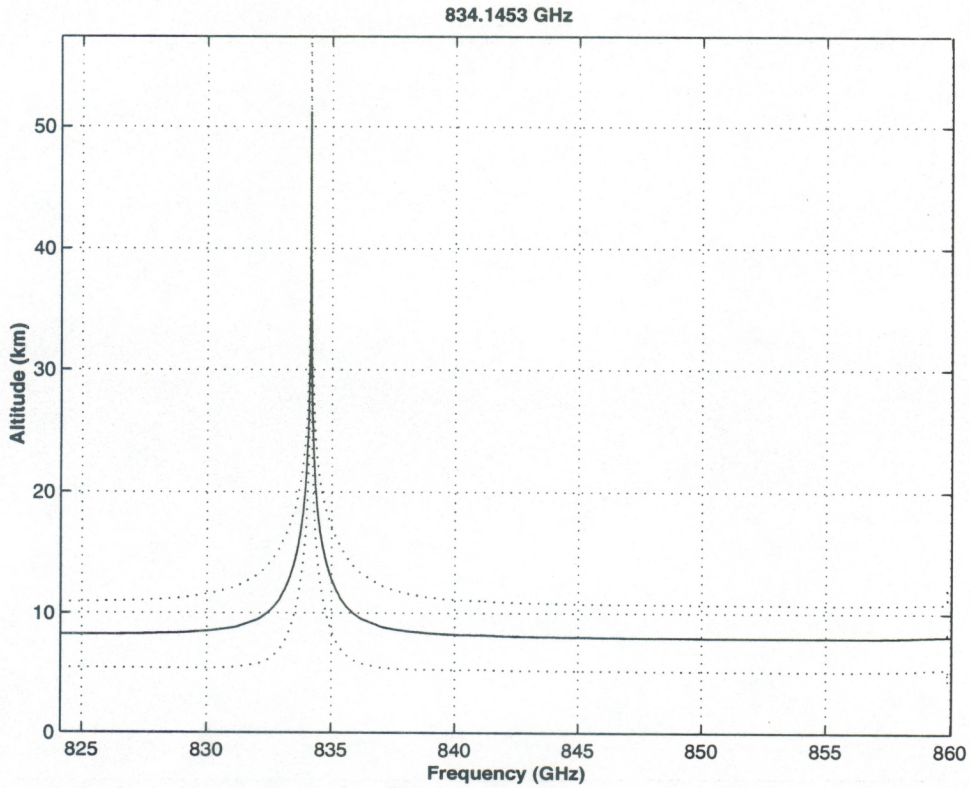

Figure 22d: Effective temperature sounding height h_{eff} along with $h_{eff} \pm \sigma_h$ for 834.1453 GHz oxygen line for

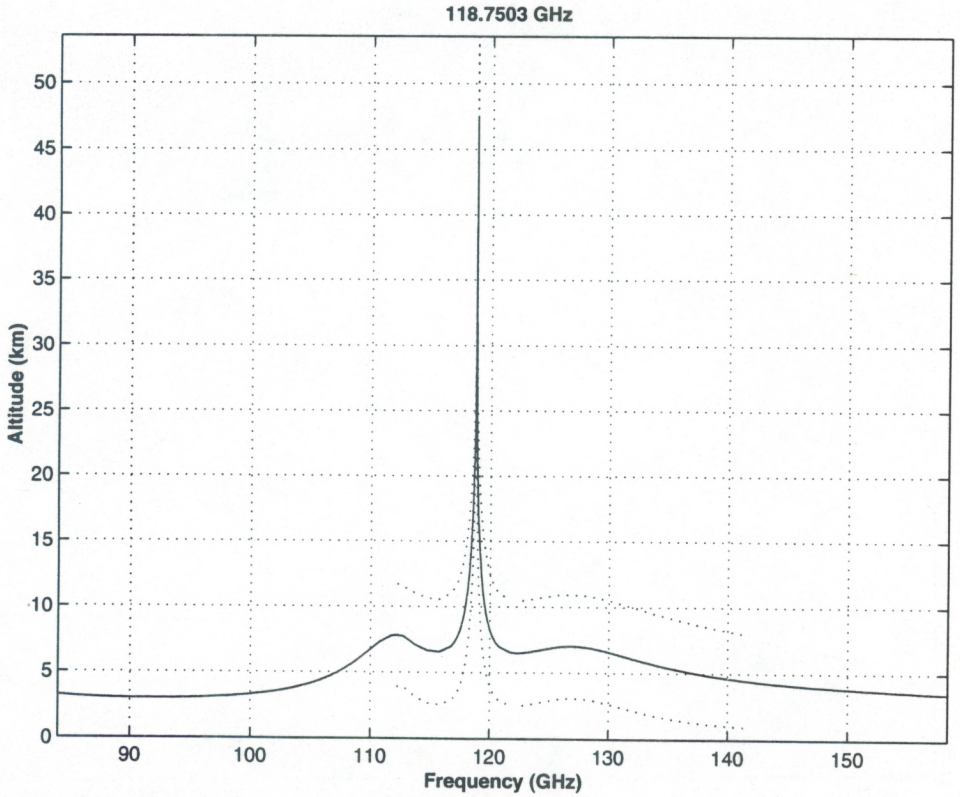

Figure 23a: Effective temperature sounding height h_{eff} along with $h_{eff} \pm \sigma_h$ for 118.7503 GHz oxygen line for winter and high latitude conditions, satellite nadir view over ocean background.

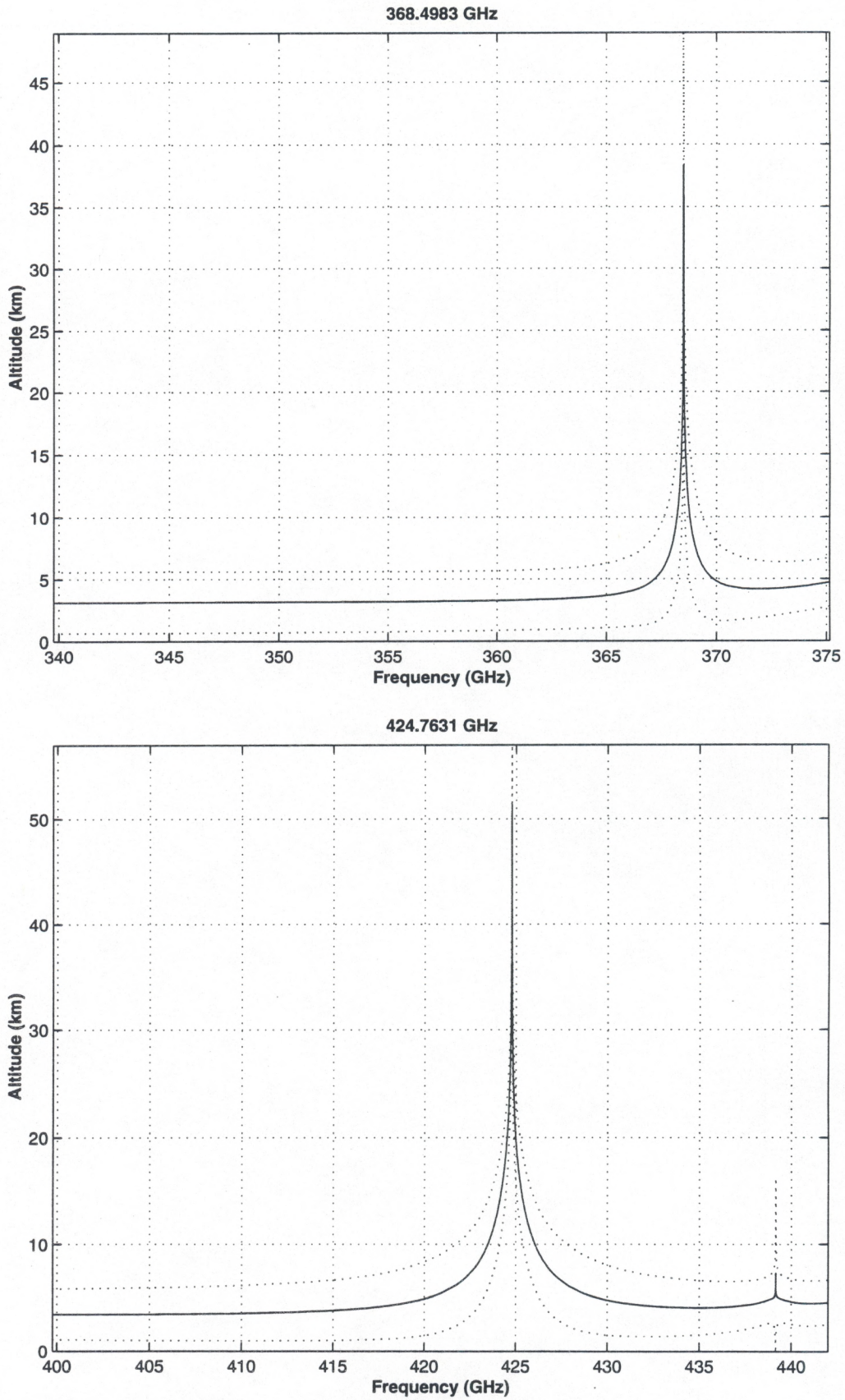

Figure 23b: Effective temperature sounding height h_{eff} along with $h_{eff} \pm \sigma_h$ for 368.4983 and 424.7631 GHz oxygen lines for winter and high latitude conditions, satellite nadir view over ocean background.

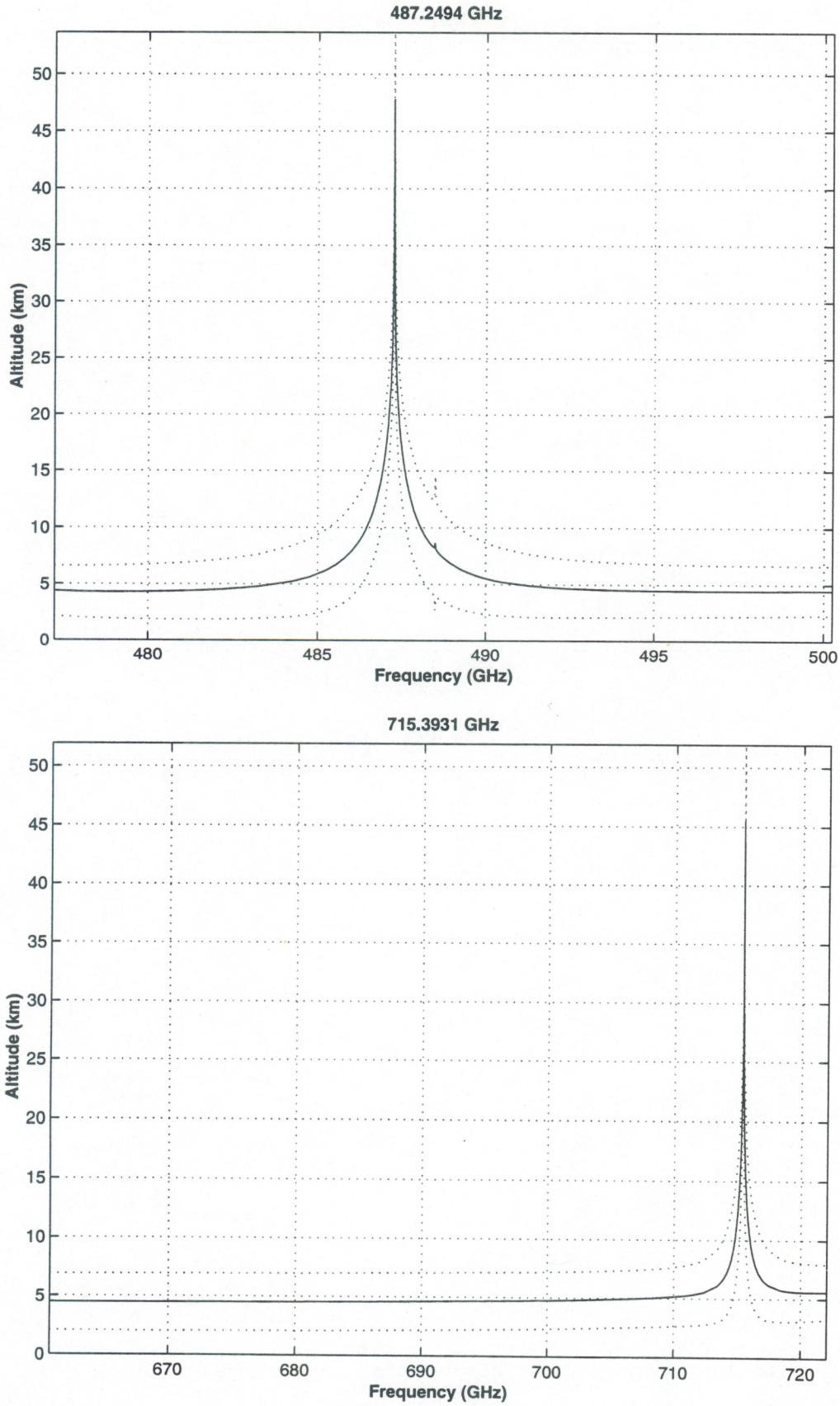

Figure 23c: Effective temperature sounding height h_{eff} along with $h_{eff} \pm \sigma_h$ for 487.2494 and 715.3931 GHz oxygen lines for winter and high latitude conditions, satellite nadir view over ocean background.

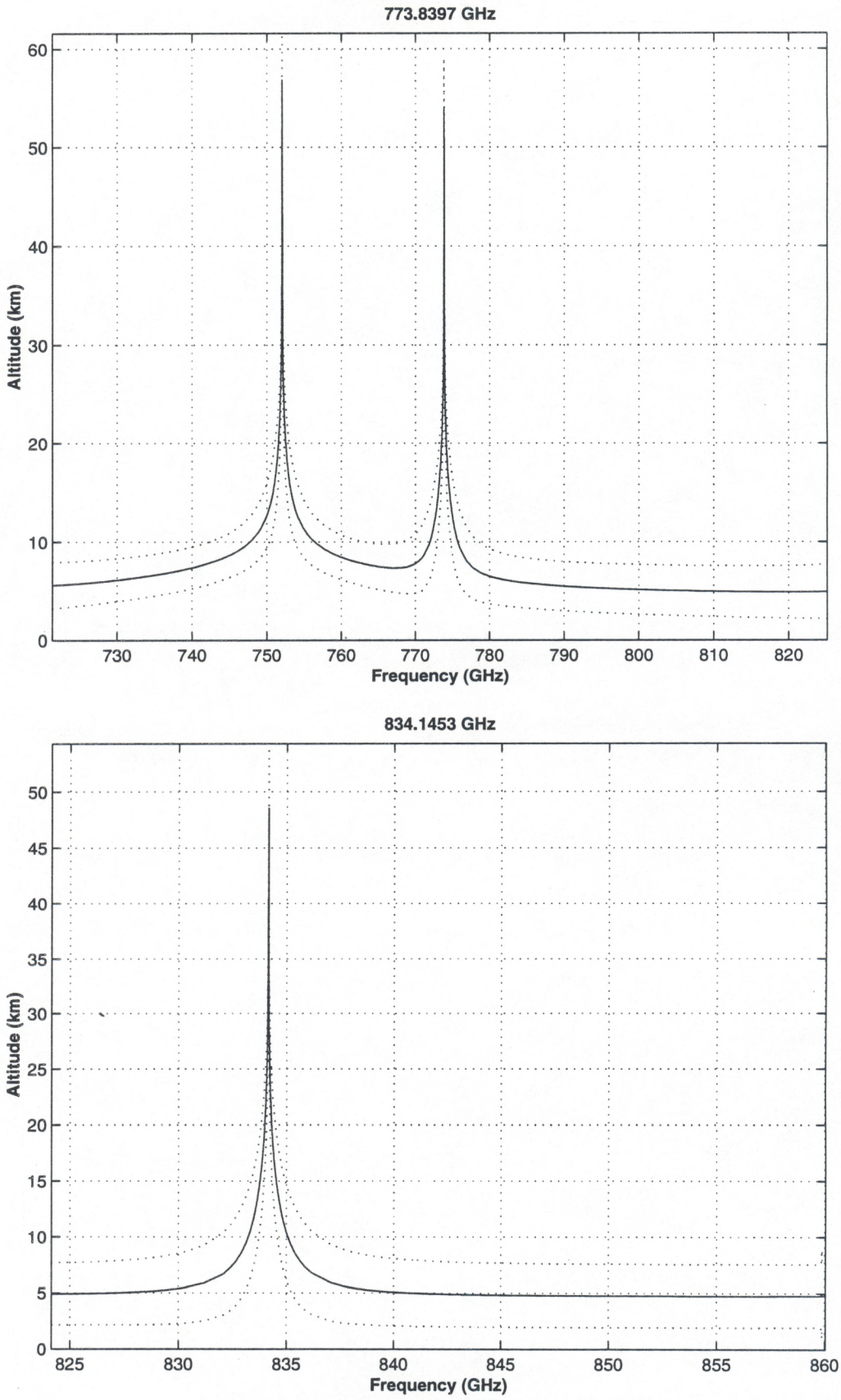

Figure 23d: Effective temperature sounding height h_{eff} along with $h_{eff} \pm \sigma_h$ for 773.8397 and 834.1453 GHz oxygen lines for winter and high latitude conditions, satellite nadir view over ocean background.

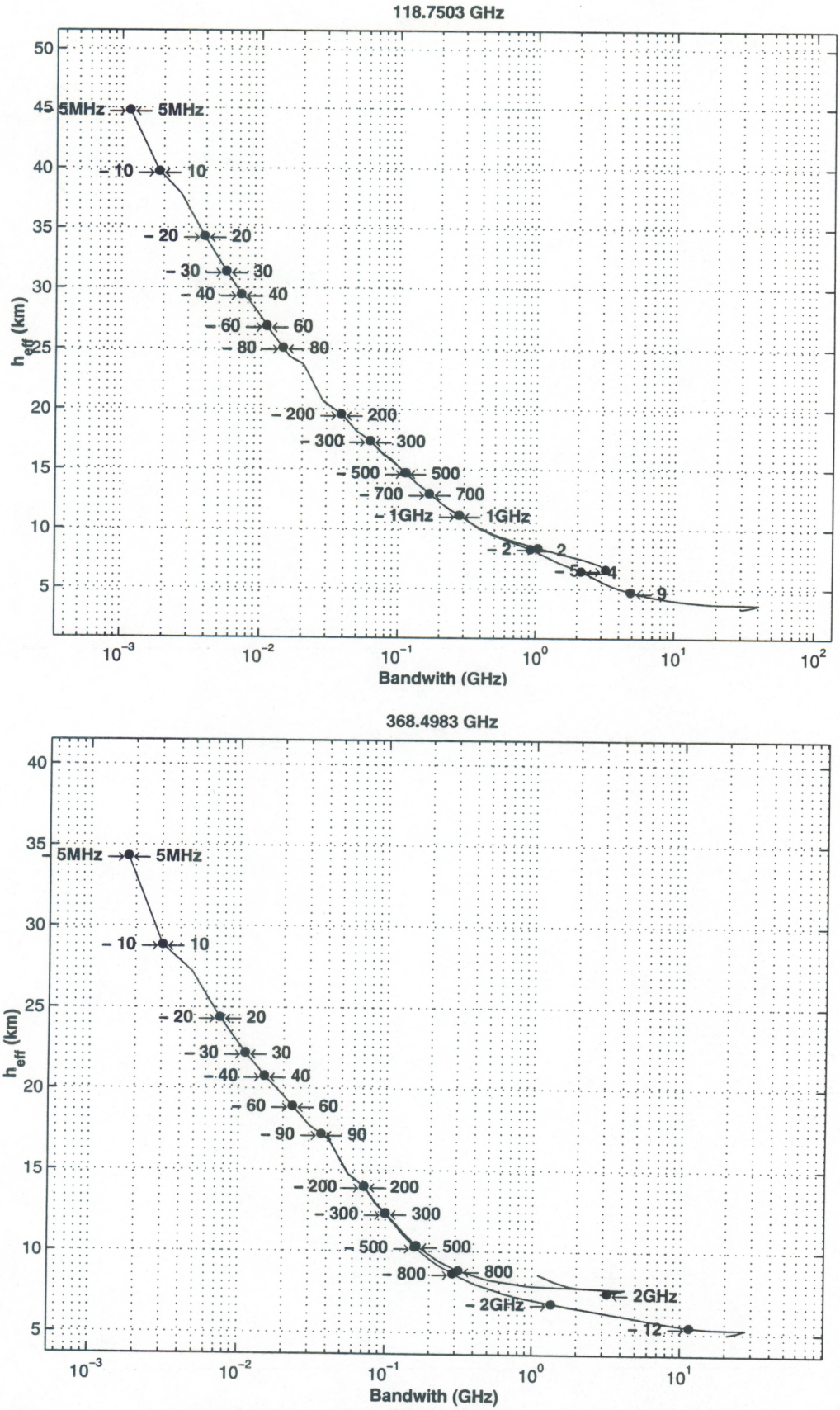

Figure 24a: Natural available bandwidth for temperature sounding for 118.7503 and 368.4983 GHz oxygen lines for summer and low latitude conditions, satellite nadir view over ocean background. The arrows and numbers indicate frequency offsets from the respective absorption line center.

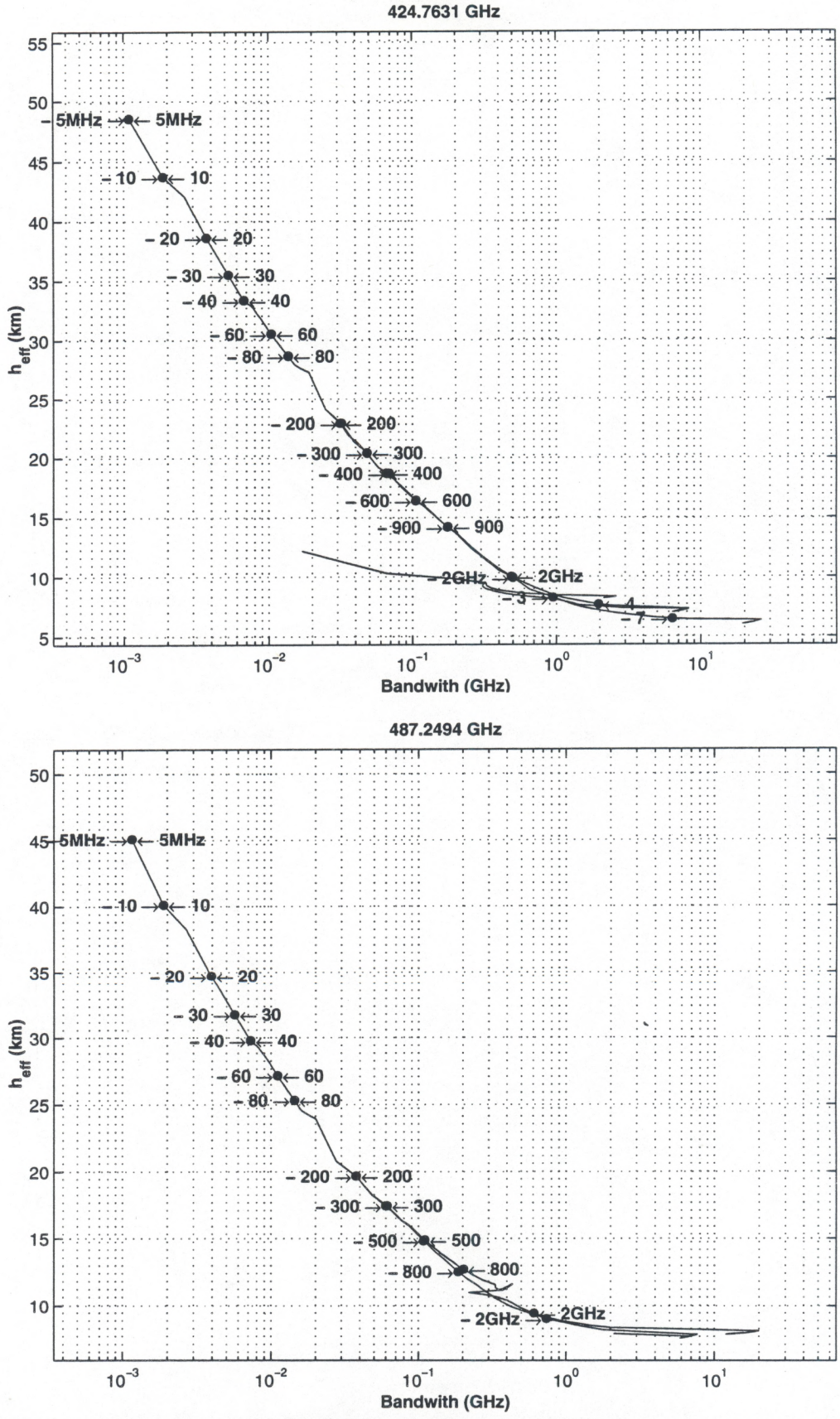

Figure 24b: Natural available bandwidth for temperature sounding for 424.7631 and 487.2494 GHz oxygen lines for summer and low latitude conditions, satellite nadir view over ocean background. The arrows and numbers indicate frequency offsets from the respective absorption line center.

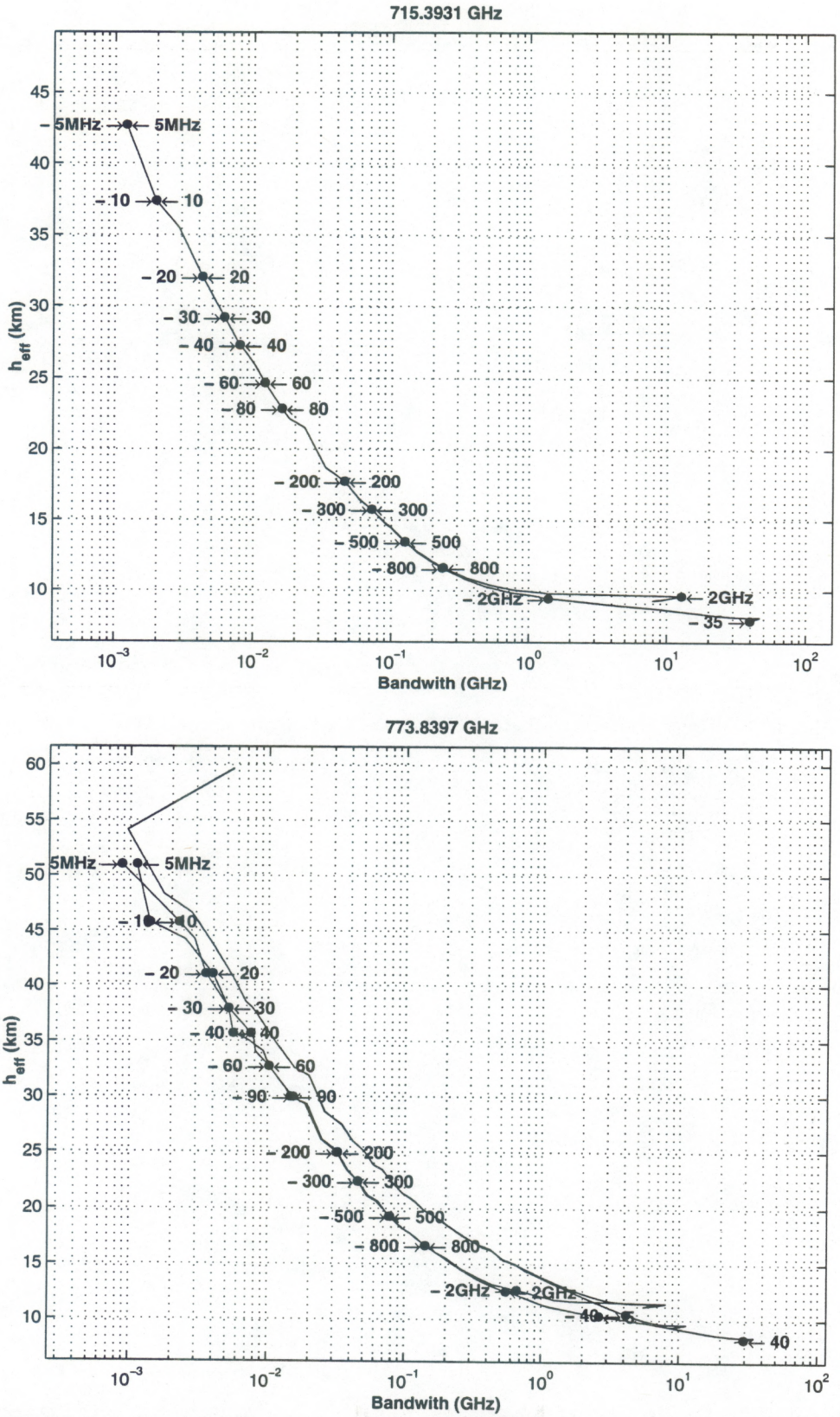

Figure 24c: Natural available bandwidth for temperature sounding for 715.3931 and 773.8397 GHz oxygen lines for summer and low latitude conditions, satellite nadir view over ocean background. The arrows and numbers indicate frequency offsets from the respective absorption line center. The double-backed nature of the curves for 773.8397 GHz oxygen line is a result of the close proximity of the 752.0332 GHz water vapor line.

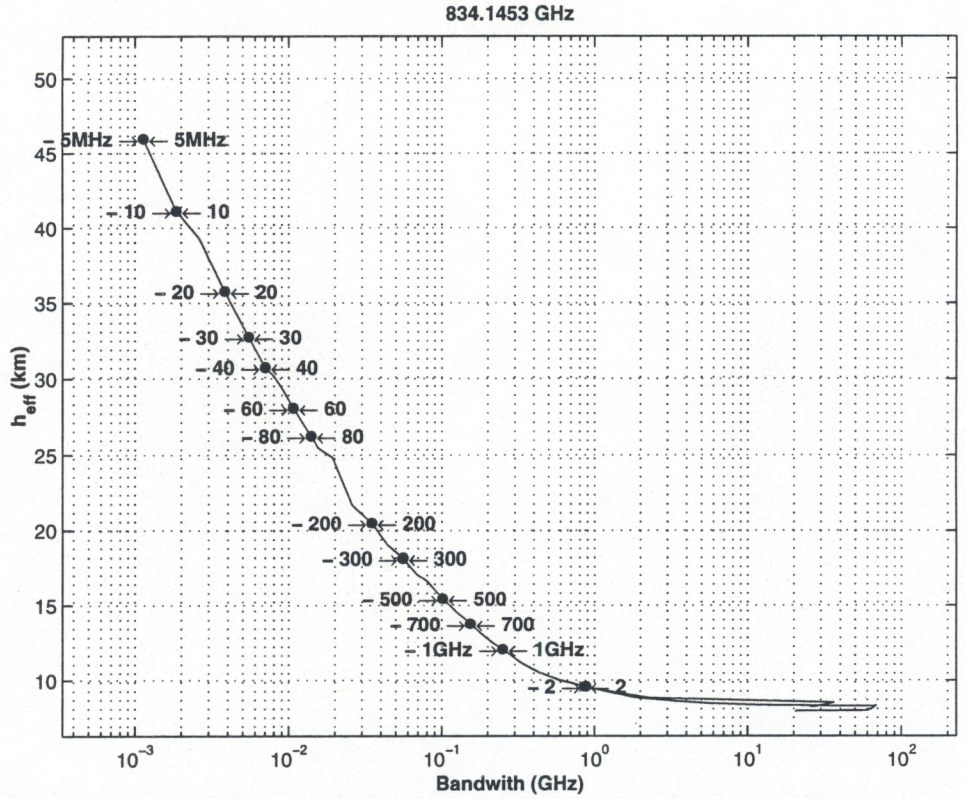

Figure 24d: Natural available bandwidth for temperature sounding for 834.1453 GHz oxygen line for summer and low latitude conditions, satellite nadir view over ocean background. The arrows and numbe

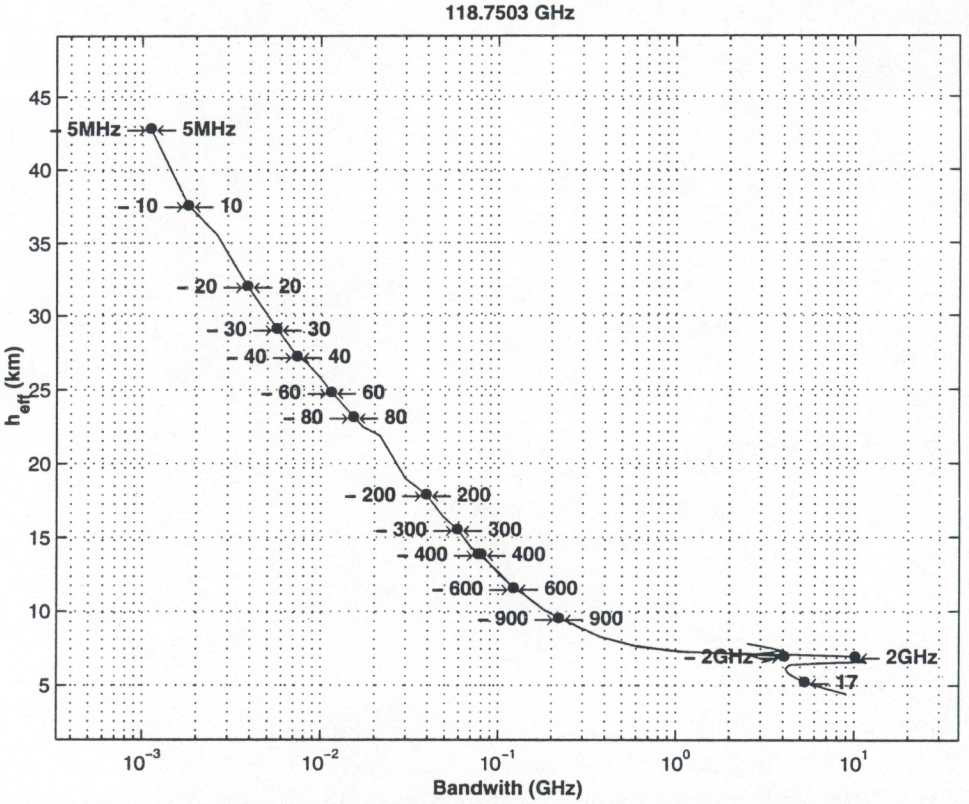

Figure 25a: Natural available bandwidth for temperature sounding for 118.7503 GHz oxygen line for winter and high latitude conditions, satellite nadir view over ocean background. The arrows and numbers indicate frequency offsets from the respective absorption line center.

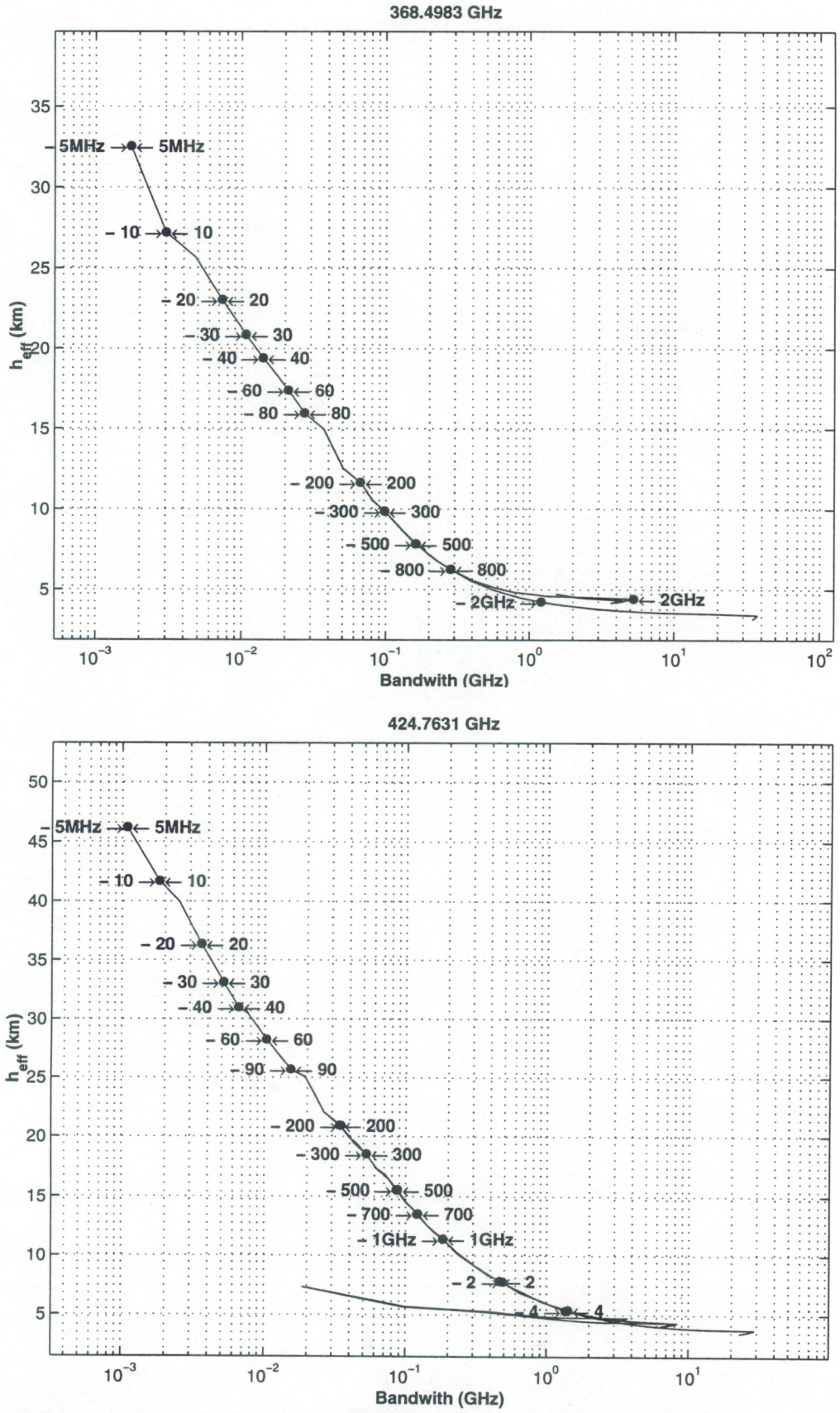

Figure 25b: Natural available bandwidth for temperature sounding for 368.4983 and 424.7631 GHz oxygen lines for winter and high latitude conditions, satellite nadir view over ocean background. The arrows and numbers indicate frequency offsets from the respective absorption line center.

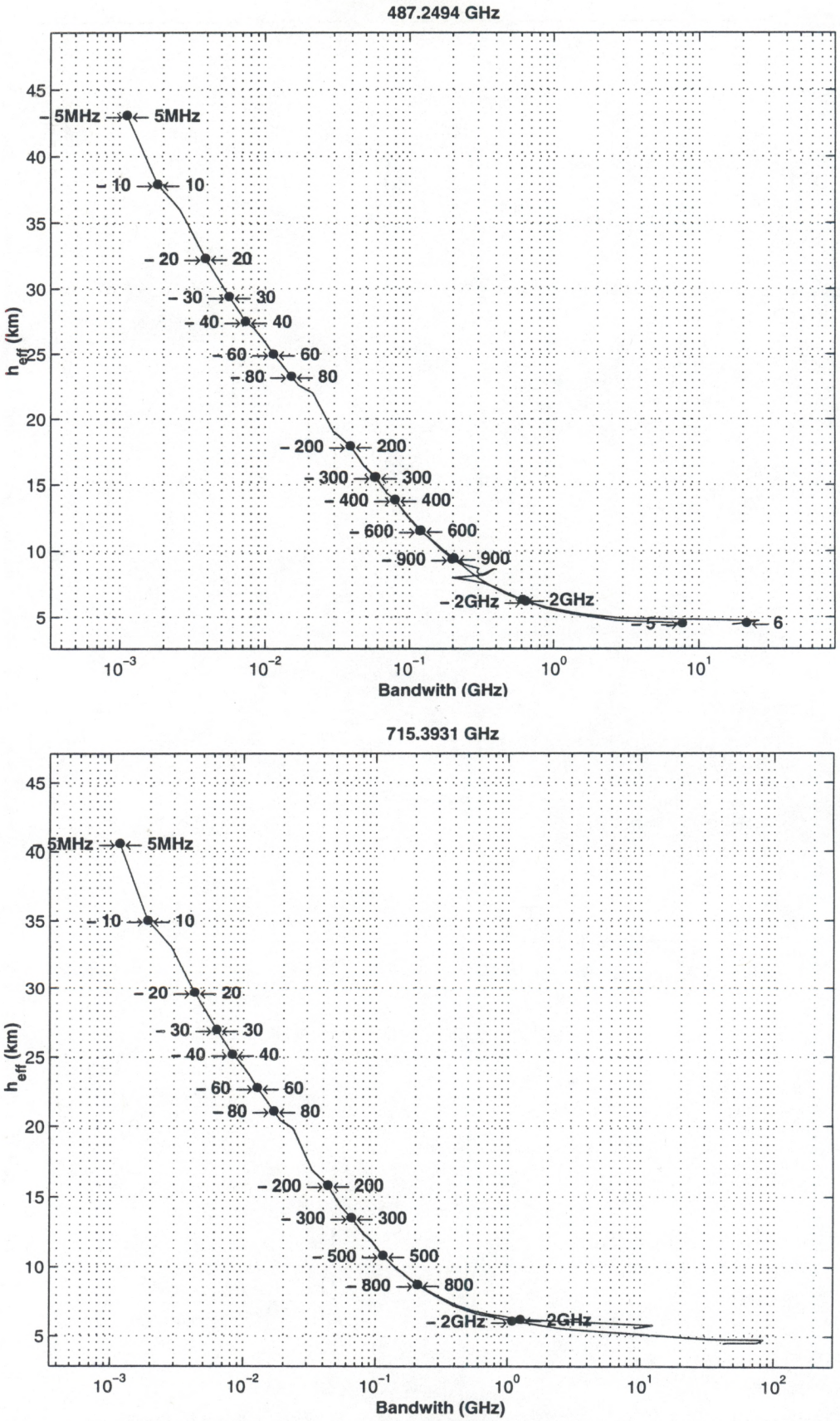

Figure 25c: Natural available bandwidth for temperature sounding for 487.2494 and 715.3931 GHz oxygen lines for winter and high latitude conditions, satellite nadir view over ocean background. The arrows and numbers indicate frequency offsets from the respective absorption line center.

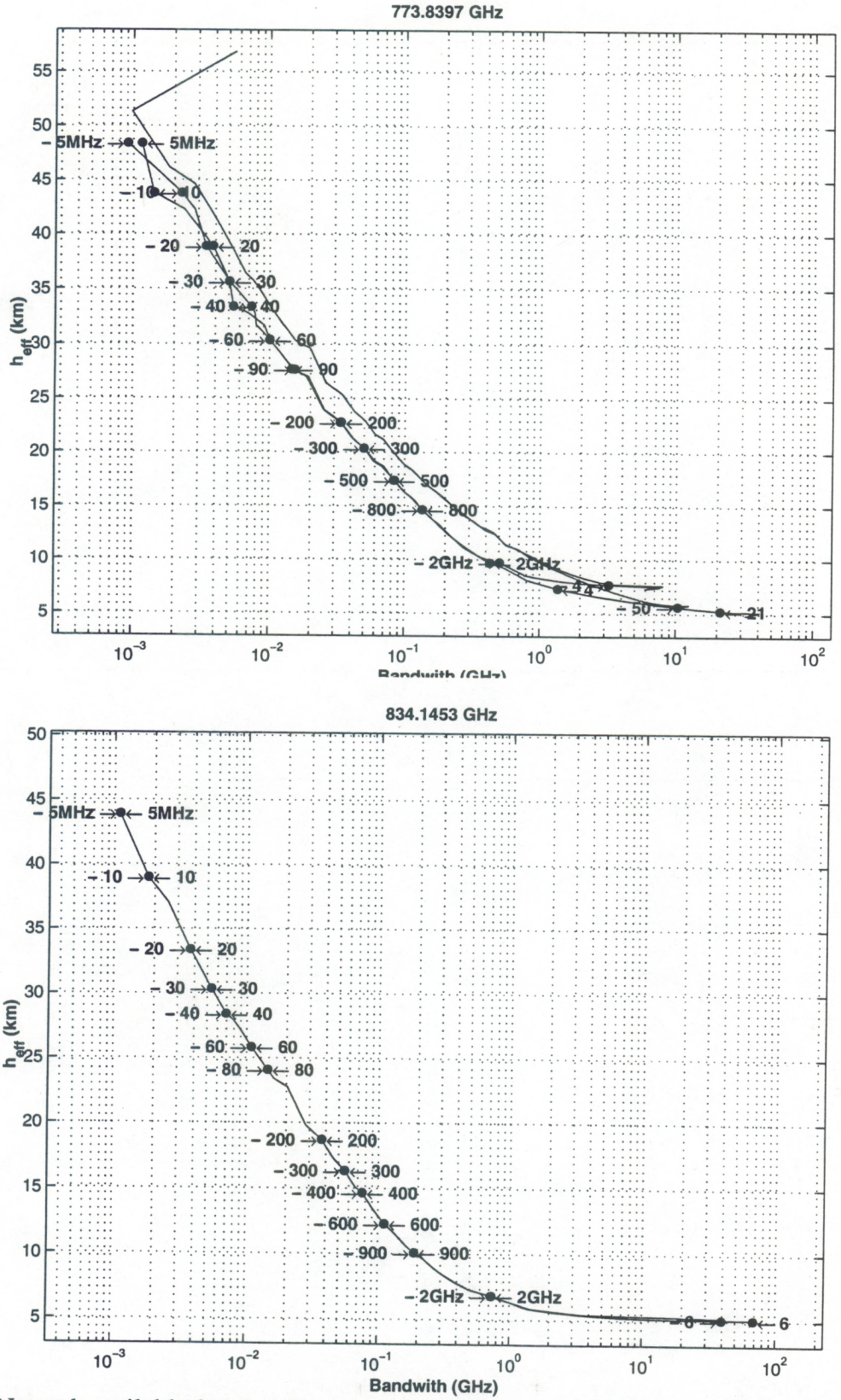

Figure 25d: Natural available bandwidth for temperature sounding for 773.8397 and 834.1453 GHz oxygen lines for winter and high latitude conditions, satellite nadir view over ocean background. The arrows and numbers indicate frequency offsets from the respective absorption line center. The double-backed nature of the curves for 773.8397 GHz oxygen line is a result of the close proximity of the 752.0332 GHz water vapor line.

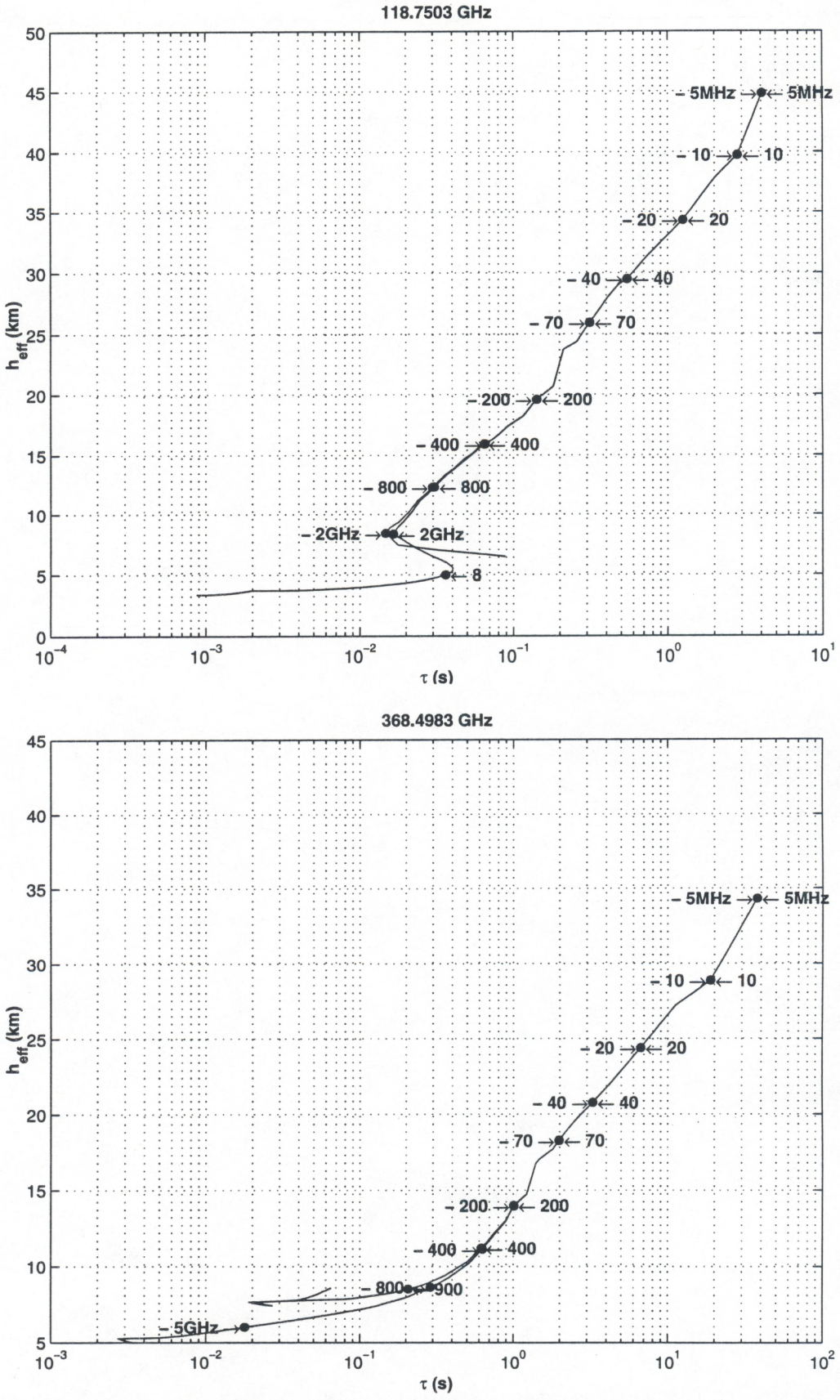

Figure 26a: Integration time for temperature sounding for 118.7503 and 368.4983 GHz oxygen lines for summer and low latitude conditions, satellite nadir view over ocean background. The arrows and numbers indicate frequency offsets from the respective absorption line center.

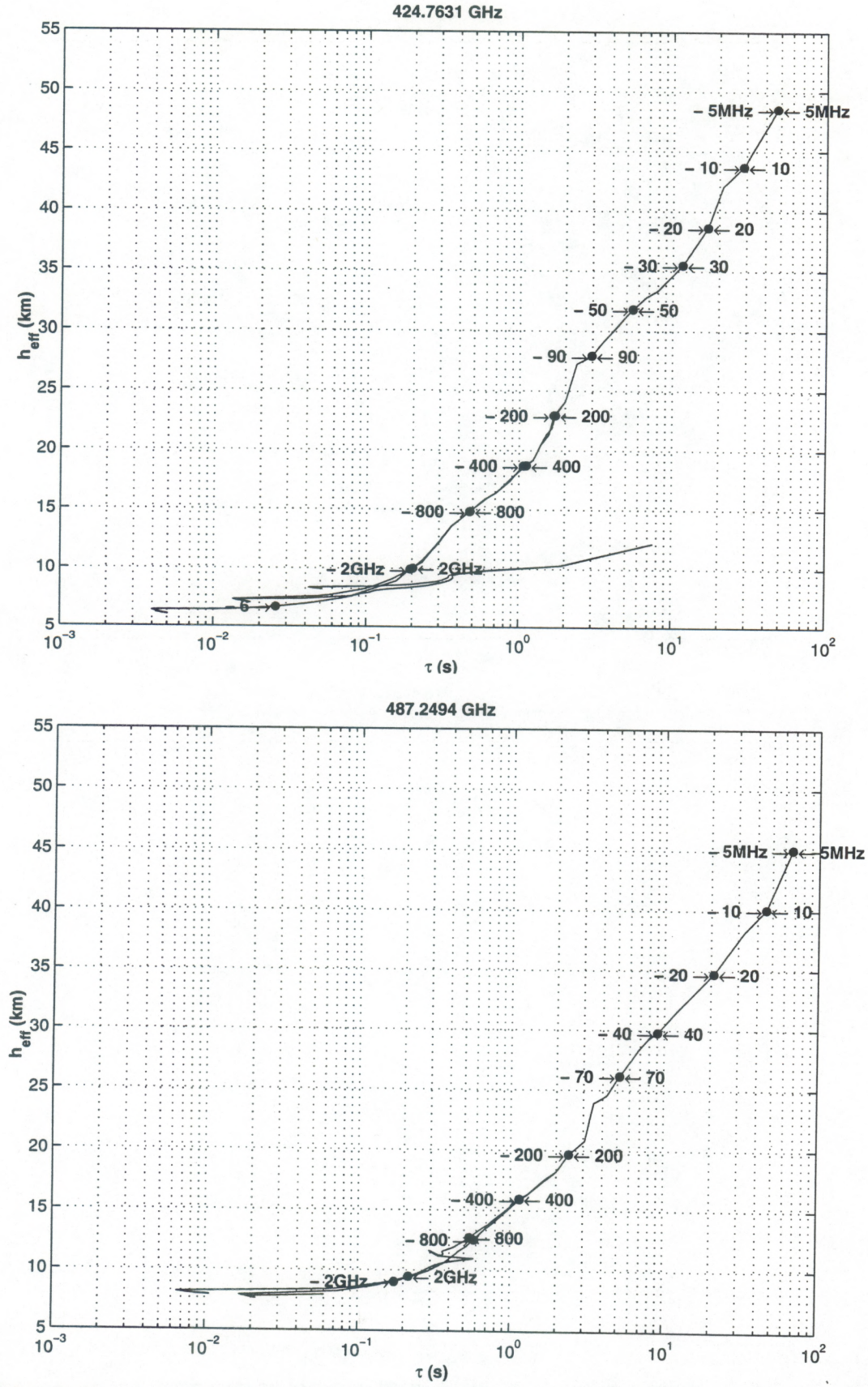

Figure 26b: Integration time for temperature sounding for 424.7631 and 487.2494 GHz oxygen lines for summer and low latitude conditions, satellite nadir view over ocean background. The arrows and numbers indicate frequency offsets from the respective absorption line center.

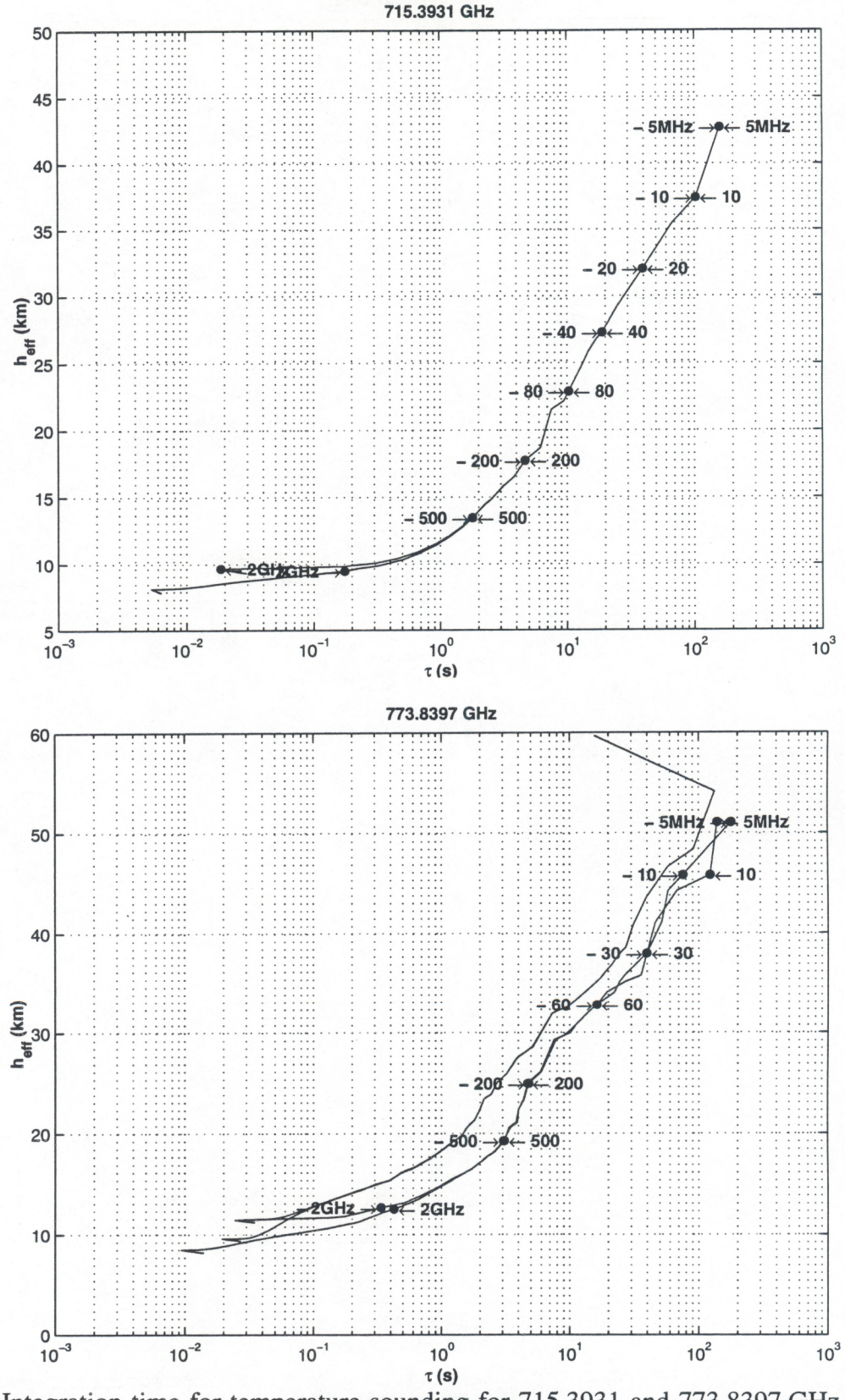

Figure 26c: Integration time for temperature sounding for 715.3931 and 773.8397 GHz oxygen lines for summer and low latitude conditions, satellite nadir view over ocean background. The arrows and numbers indicate frequency offsets from the respective absorption line center. The double-backed nature of the curves for 773.8397 GHz oxygen line is a result of the close proximity of the 752.0332 GHz water vapor line.

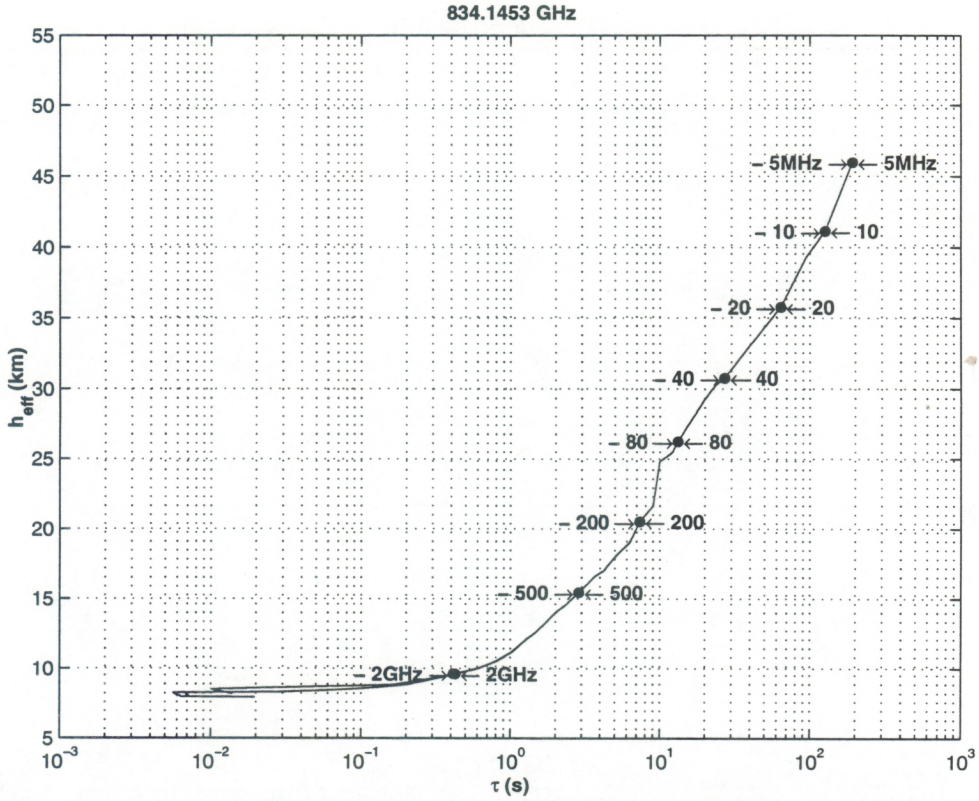

Figure 26d: Integration time for temperature sounding for 834.1453 GHz oxygen line for summer and low latitude conditions, satellite nadir view over ocean background. The arrows and numbers indicate freque

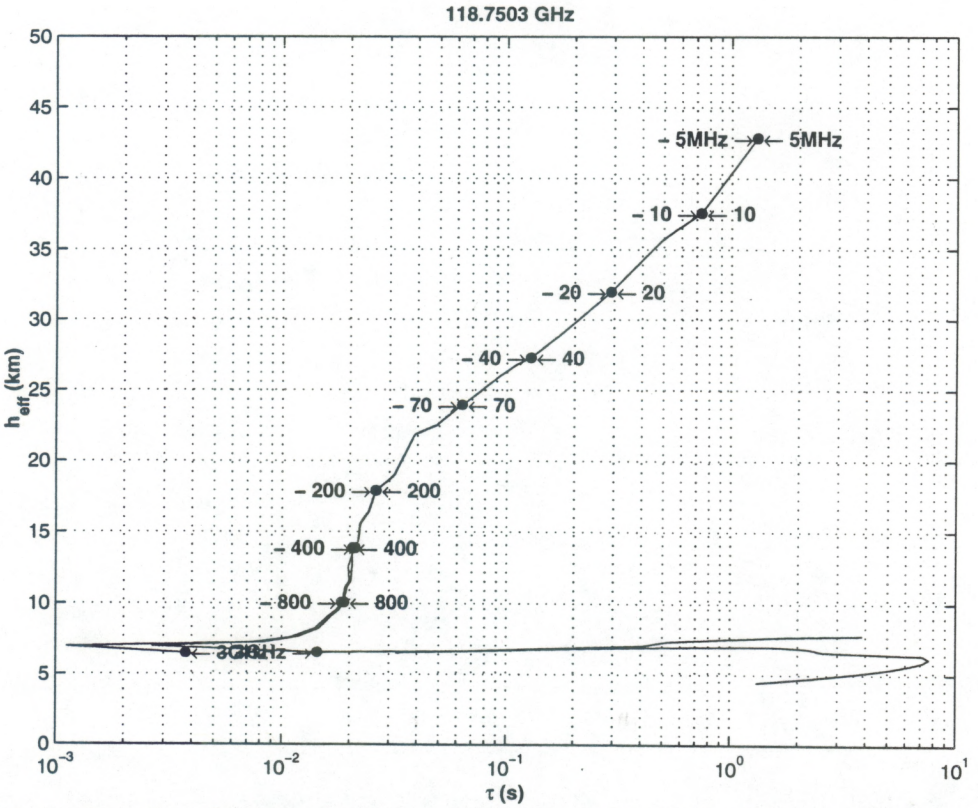

Figure 27a: Integration time for temperature sounding for 118.7503 GHz oxygen line for winter and high latitude conditions, satellite nadir view over ocean background. The arrows and numbers indicate frequency offsets from the respective absorption line center.

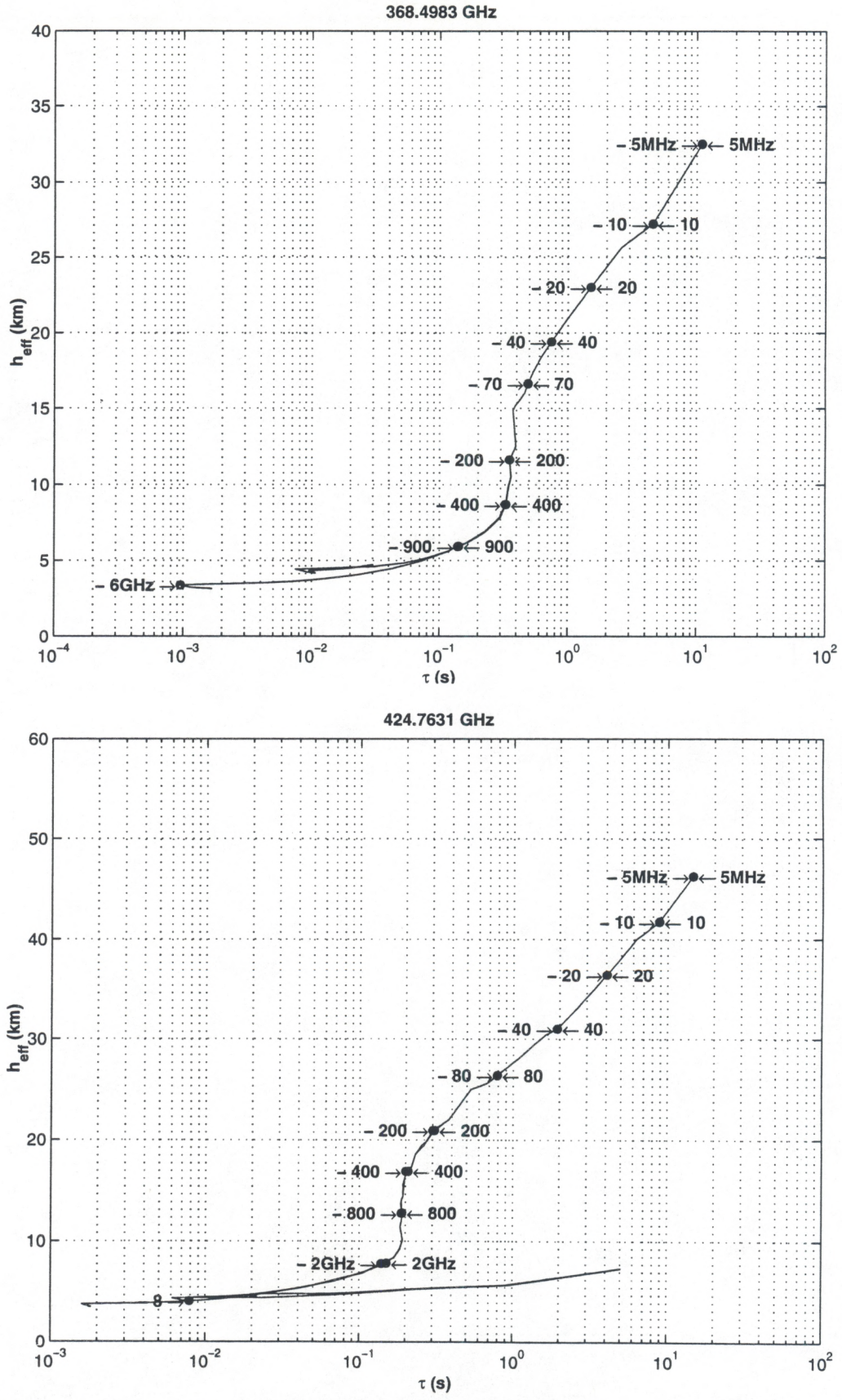

Figure 27b: Integration time for temperature sounding for 368.4983 and 424.7631 GHz oxygen lines for winter and high latitude conditions, satellite nadir view over ocean background. The arrows and numbers indicate frequency offsets from the respective absorption line center.

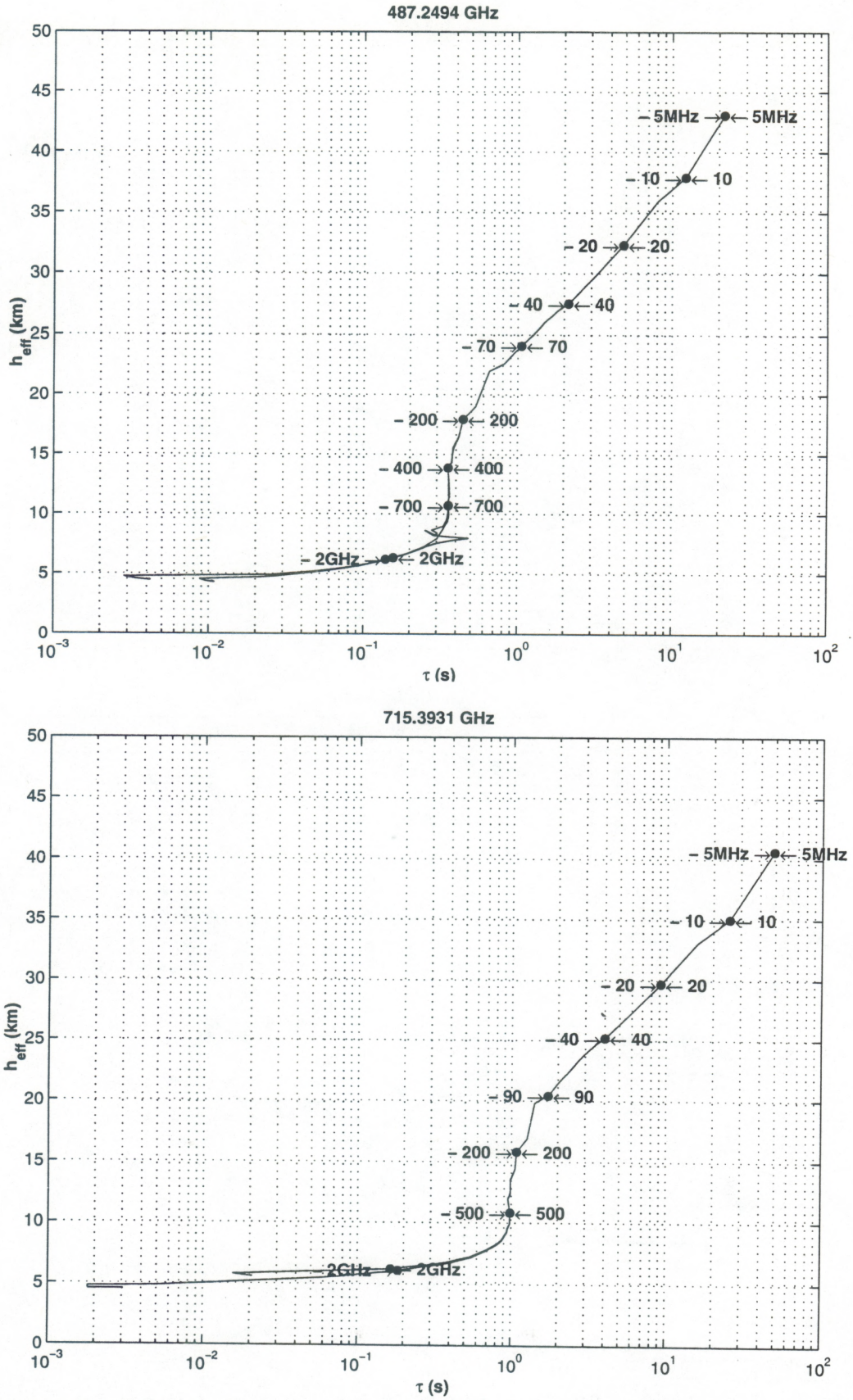

Figure 27c: Integration time for temperature sounding for 487.2494 and 715.3931 GHz oxygen lines for winter and high latitude conditions, satellite nadir view over ocean background. The arrows and numbers indicate frequency offsets from the respective absorption line center.

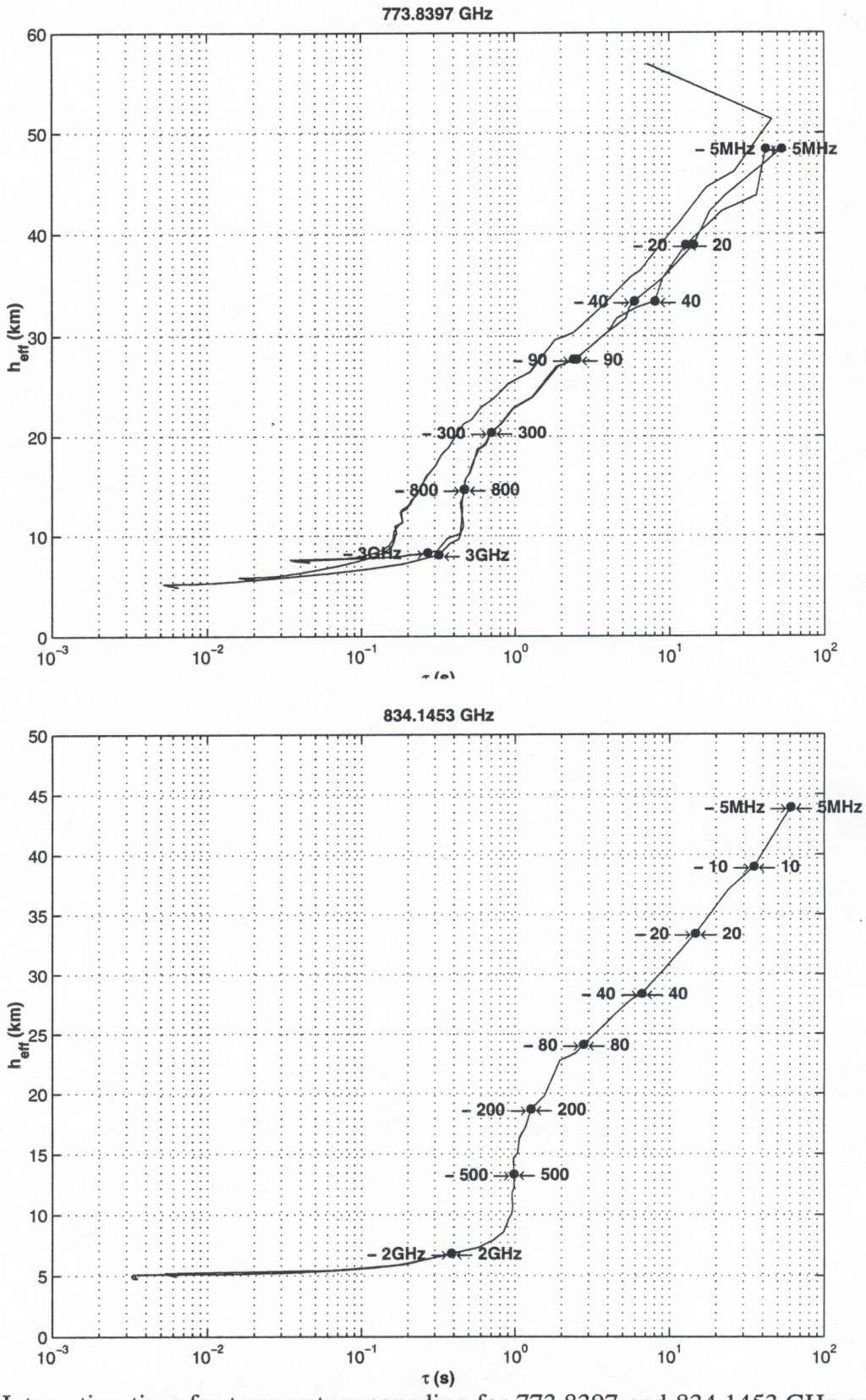

Figure 27d: Integration time for temperature sounding for 773.8397 and 834.1453 GHz oxygen lines for winter and high latitude conditions, satellite nadir view over ocean background. The arrows and numbers indicate frequency offsets from the respective absorption line center. The double-backed nature of the curves for 773.8397 GHz oxygen line is a result of the close proximity of the 752.0332 GHz water vapor line.

*U.S. GOVERNMENT PRINTING OFFICE 1998-0-773-022/40120